

Springer Theses

Recognizing Outstanding Ph.D. Research

Takuya Shimajiri

The Nature of Ultralong C—C Bonds



Springer

Springer Theses

Recognizing Outstanding Ph.D. Research

Aims and Scope

The series “Springer Theses” brings together a selection of the very best Ph.D. theses from around the world and across the physical sciences. Nominated and endorsed by two recognized specialists, each published volume has been selected for its scientific excellence and the high impact of its contents for the pertinent field of research. For greater accessibility to non-specialists, the published versions include an extended introduction, as well as a foreword by the student’s supervisor explaining the special relevance of the work for the field. As a whole, the series will provide a valuable resource both for newcomers to the research fields described, and for other scientists seeking detailed background information on special questions. Finally, it provides an accredited documentation of the valuable contributions made by today’s younger generation of scientists.

Theses may be nominated for publication in this series by heads of department at internationally leading universities or institutes and should fulfill all of the following criteria

- They must be written in good English.
- The topic should fall within the confines of Chemistry, Physics, Earth Sciences, Engineering and related interdisciplinary fields such as Materials, Nanoscience, Chemical Engineering, Complex Systems and Biophysics.
- The work reported in the thesis must represent a significant scientific advance.
- If the thesis includes previously published material, permission to reproduce this must be gained from the respective copyright holder (a maximum 30% of the thesis should be a verbatim reproduction from the author’s previous publications).
- They must have been examined and passed during the 12 months prior to nomination.
- Each thesis should include a foreword by the supervisor outlining the significance of its content.
- The theses should have a clearly defined structure including an introduction accessible to new PhD students and scientists not expert in the relevant field.

Indexed by zbMATH.

Takuya Shimajiri

The Nature of Ultralong C–C Bonds

Doctoral Thesis accepted by
Hokkaido University, Sapporo, Japan

 Springer

Author
Takuya Shimajiri
Department of Chemistry
Hokkaido University
Sapporo, Japan

Supervisor
Takanori Suzuki
Hokkaido University
Sapporo, Japan

ISSN 2190-5053

ISSN 2190-5061 (electronic)

Springer Theses

ISBN 978-981-99-0669-7

ISBN 978-981-99-0670-3 (eBook)

<https://doi.org/10.1007/978-981-99-0670-3>

© The Editor(s) (if applicable) and The Author(s), under exclusive license to Springer Nature Singapore Pte Ltd. 2023

This work is subject to copyright. All rights are solely and exclusively licensed by the Publisher, whether the whole or part of the material is concerned, specifically the rights of translation, reprinting, reuse of illustrations, recitation, broadcasting, reproduction on microfilms or in any other physical way, and transmission or information storage and retrieval, electronic adaptation, computer software, or by similar or dissimilar methodology now known or hereafter developed.

The use of general descriptive names, registered names, trademarks, service marks, etc. in this publication does not imply, even in the absence of a specific statement, that such names are exempt from the relevant protective laws and regulations and therefore free for general use.

The publisher, the authors, and the editors are safe to assume that the advice and information in this book are believed to be true and accurate at the date of publication. Neither the publisher nor the authors or the editors give a warranty, expressed or implied, with respect to the material contained herein or for any errors or omissions that may have been made. The publisher remains neutral with regard to jurisdictional claims in published maps and institutional affiliations.

This Springer imprint is published by the registered company Springer Nature Singapore Pte Ltd. The registered company address is: 152 Beach Road, #21-01/04 Gateway East, Singapore 189721, Singapore

Supervisor's Foreword

The C–C covalent bonding is the most basic concept of organic chemistry. When two hybridized Csp^3 atoms are closing to each other, they form a strong covalent bond through an overlap in a head-on manner along the axis of the atoms, for which the standard bond length is 1.54 Å, as in ethane (CC). This value does not often change in all organic molecules, because deviation from the standard causes a large loss of bonding energy. The bond elongation is caused only when the molecule suffers from severe steric hindrance and/or geometrical strain. Such molecules with an expanded bond would exhibit special properties which the ordinary molecules do not have.

The Ph.D. thesis of Dr. Takuya Shimajiri focuses on the extremely long Csp^3 – Csp^3 bond with exploitation of the new facets of covalent bonding. Based on the previously assumed linear correlation between the bond length and bond energy, the limit of bond length was predicted to be 1.748 Å for Csp^3 . This value seemingly matches the shortest non-bonded contact of 1.80 Å. However, Takuya's curiosity and creativity made him to design a series of hexaphenylethane (HPE) derivatives with dispiro (dibenzocycloheptatriene) units. Actually, he has demonstrated that one of these compounds has the bond length which is greater than the shortest non-bonded contact. Despite the presence of such a weakened bond with a small bond energy, these HPEs were found to be surprisingly stable against heat and air, which differs from the previous general view that the long bond is easily cleaved. In addition, Takuya's hard work led to discover the flexibility of the covalent bond, which is a newly proposed facet. He succeeded to show experimentally that such an elongated Csp^3 – Csp^3 bond can shrink and expand easily and reversibly in response to the external stimuli. These groundbreaking results in the thesis are deserving of a place in the Springer Theses series.

Sapporo, Japan
October 2022

Takanori Suzuki

Parts of this thesis have been published in the following journal articles

Longest C–C Single Bond among Neutral Hydrocarbons with a Bond Length beyond 1.8 Å. Y. Ishigaki, **T. Shimajiri**, T. Takeda, R. Katoono, T. Suzuki, *Chem* **2018**, *4*, 795–806.

Flexible C–C Bonds: Reversible Expansion, Contraction, Formation, and Scission of Extremely Elongated Single Bonds. **T. Shimajiri**, T. Suzuki, Y. Ishigaki, *Angew. Chem. Int. Ed.* **2020**, *59*, 22252–22257.

Acknowledgements

This work has been carried out under the direction of Associate Professor Dr. Yusuke Ishigaki (Department of Chemistry, Faculty of Science, Hokkaido University). The author pays his heartfelt respects and gratitude to Associate Professor Ishigaki for his consistent guidance, suggestion, valuable discussions, encouragement, and so much help throughout the course of this work.

The author would like to express the deepest appreciation to Prof. Dr. Takanori Suzuki (Department of Chemistry, Faculty of Science, Hokkaido University) for his kind guidance, valuable discussions and so much help throughout the course of this work. He taught the author the basics of the way to study.

The author deeply grateful to Assistant Professor Dr. Ryo Katoono (Department of Chemistry, Faculty of Science, Hokkaido University) for his kind guidance, valuable discussion and so much help throughout the course of this work.

The author would like to thank Prof. Dr. Tetsuya Taketsugu, Prof. Dr. Keiji Tanino and Prof. Dr. Takeshi Ohkuma (Department of Chemistry, Faculty of Science, Hokkaido University) for their valuable suggestions and discussions.

The author expresses sincere thanks to Dr. Yasuto Uchimura and Dr. Yuto Sakano for their guidance and valuable discussions throughout the course of this work.

The author expresses sincere thanks to Dr. Yu Ozawa, Dr. Rina Takahashi and Dr. Kanami Sugiyama for their valuable discussions throughout the course of this work.

The author is really thankful to Dr. Eri Fukushi and Mr. Yusuke Takada (GC-MS & NMR Laboratory, Graduate School of Agriculture, Hokkaido University) for the measurement of mass.

The author wish to express special thanks to Prof. Dr. G. Dan (Department of Chemistry, University of Bath) and all the members of his laboratory for their hospitable support, heartfelt guidance and valuable suggestions during my stay in Bath, UK.

The author gives a special thanks to Mr. Yuki Saito, Mr. Satoshi Okamoto, Dr. Wataru Nojo, Dr. Yuse Kuriyama, Mr. Keisuke Sugimoto, Mr. Kazuki Sakamoto and other members in Suzuki Laboratory from the bottom of his heart for their valuable discussions and giving his invaluable time.

The author is in acknowledgement of Research Fellowship of the Japan Society for the Promotion of Science (JSPS) for Young Scientists for Financial Support.

Finally, the author would like to express his deep, sincere and endless gratitude to his family, Yoshifumi Shimajiri, Michiyo Shimajiri and Kentaro Shimajiri for their continuous help and encouragement.

Sapporo, Japan
2022

Takuya Shimajiri

Contents

| | | |
|----------|--|----|
| 1 | General Introduction | 1 |
| 1.1 | C–C Covalent Bond | 1 |
| 1.2 | Unusual Bonding Interaction..... | 3 |
| 1.3 | Short and Long C–C Single Bond..... | 4 |
| | References | 7 |
| 2 | Creation and Demonstration of the Longest C–C Single Bond with a Bond Length Beyond 1.8 Å | 9 |
| 2.1 | Introduction | 9 |
| 2.2 | Results and Discussions..... | 10 |
| 2.2.1 | Design Concept..... | 10 |
| 2.2.2 | Theoretical Examination for Molecular Design..... | 12 |
| 2.2.3 | Preparation of Hydrocarbon 1a–1c..... | 15 |
| 2.2.4 | Raman Spectroscopy | 16 |
| 2.2.5 | Experimentally Determined Bond Length by X-ray Analyses | 18 |
| 2.2.6 | Stability of the Hydrocarbon 1c with a Very Weak C–C Bond | 20 |
| 2.2.7 | Theoretical Analysis for the Nature of Ultralong C–C Single Bond..... | 23 |
| 2.3 | Conclusion | 26 |
| 2.4 | Experimental Section | 28 |
| | References | 39 |
| 3 | Discovery of Flexible Bonds Based on an Extremely Elongated C–C Single Bond | 41 |
| 3.1 | Introduction | 41 |
| 3.2 | Results and Discussions..... | 43 |
| 3.2.1 | Intramolecular Photocyclization..... | 43 |
| 3.2.2 | Theoretical Study | 46 |
| 3.2.3 | Single-Crystal-to-Single-Crystal Transformation | 49 |
| 3.2.4 | Redox Behavior | 50 |

| | |
|--------------------------------|-----------|
| 3.3 Conclusion | 57 |
| 3.4 Experimental Section | 58 |
| References | 77 |
| Curriculum Vitae..... | 79 |

Chapter 1

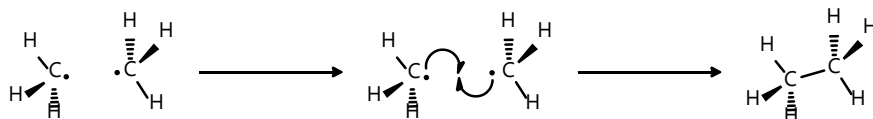
General Introduction



1.1 C–C Covalent Bond

Organic chemists study organic compounds, which are basically defined as molecules that contain one or more carbon (C) atom(s), excluding carbon oxides (CO and CO₂), inorganic cyanides (XCN), and carbonates (X_nCO₃). Such organic compounds are mainly constructed by covalent bonds between atoms. A covalent bond, in which two atoms are connected by sharing two electrons, is a class of chemical bonding, as proposed by Lewis (Scheme 1.1). Pauling systematized the chemical bond theory, including the covalent bond [3]. Currently, a covalent bond is defined by IUPAC as “a region of relatively high electron density between nuclei which arises at least partly from sharing of electrons and gives rise to an attractive force and characteristic internuclear distance” [4].

In this context, the C–C covalent bond is the most basic concept of organic compounds. In general, a carbon atom has an electronic configuration of $[1s]^2[2s]^2[2p]^2$, and the four valence electrons in the $2s$ and $2p$ orbitals of a carbon atom are involved in chemical bonds and reactions. By promotion of an electron from the $2s$ orbital to a $2p$ orbital, the valence state is formed, and then $2s$ and $2p$ orbitals hybridize to make new orbitals (hybridized orbital). By the formation of hybridized orbitals, there are three types of C–C covalent bonds: C–C single bonds, C=C double bonds, and C≡C triple bonds (Fig. 1.1). Depending on the manner of bonding, these electron states of carbon atoms are described as sp^3 hybridization for a C–C single bond, sp^2 hybridization for a C=C double bond, and sp hybridization for a C≡C triple bond, corresponding to the ratio between s - and p -orbitals (e.g., sp^3 ; s -orbital character: p -orbital character = 1: 3). When two hybridized C atoms are close to each other, they form a strong bond in which they overlap in a head-on manner along the axis of the atoms, called a σ -bond. In the case of sp^2 - or sp hybridization, unhybridized p -orbitals still remain, and they can interact with each other by overlapping sideways to form a second or third bond (π -bond). The electrons in a σ -bond occupy the central region between nuclei, while the electrons in a π -bond occupy the regions



Scheme 1.1 C–C covalent bond

on either side of a line between nuclei. Due to the large overlap integral of the σ -bond, the σ -bond has a greater bonding energy than the π -bond.

With regard to the structural parameters, the standard bond length is 1.54 Å for a C–C single bond with sp^3 hybridization, 1.33 Å for a C=C double bond with sp^2 hybridization, and 1.33 Å for a C≡C triple bond with sp hybridization. The C=C double bond and C≡C triple bond often show expansion or contraction since the π -bond is sensitive to the electronic environment around the bond. However, the C–C single bond does not change because deviation from the standard causes a large loss of bonding energy.

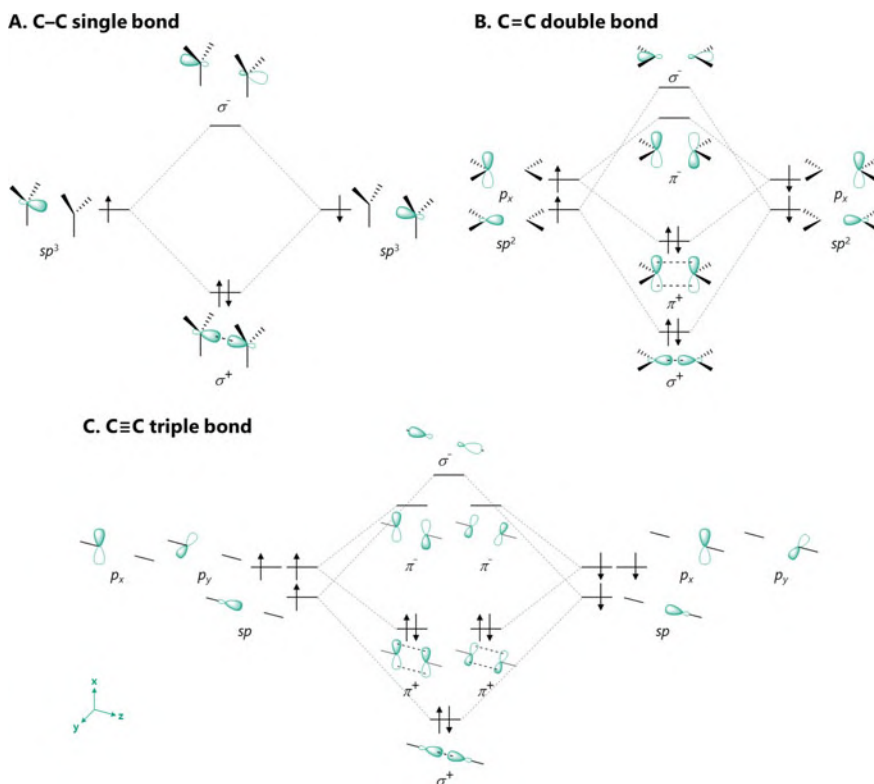


Fig. 1.1 Energy diagram of C–C covalent bond

1.2 Unusual Bonding Interaction

As mentioned above, the structural parameters such as bond length, bond angle, and torsion angle among carbon atoms are nearly constant as a result of their hybrid orbitals (Fig. 1.2). On the other hand, unusual geometrical parameters have been reported for highly strained molecules, such as sterically congested and/or curved polycyclic aromatic hydrocarbons [5–12] as well as cyclic π -conjugated molecules, including cycloparaphenylenes [13–21], which are endowed with special properties that are not seen with ordinary hydrocarbons.

In terms of the C–C bond, several attempts have been made to obtain molecules with an unusual chemical bonding. For example, some molecules such as cyclic 1,3-diyl diradical were reported to have π -single bonding without a σ -bond, although the C–C single bond is basically constructed by a σ -bond (Fig. 1.3) [22–24].

From another point of view, atoms such as carbon obey the octet rule and can make four covalent bonds with two electrons in each bond. However, some atoms can form more than four bonds, which are known as hypervalent bonds. These bonds have been well-studied in compounds containing heavier main-group elements, but very rarely in carbon-based compounds. Akiba and Yamamoto et al. reported that anthracene derivatives have pentacoordinate and hexacoordinate carbocations (Fig. 1.4) [25–27]. These results are supported by X-ray analyses and theoretical studies.



Fig. 1.2 Standard bond length and bond angles of C–C bonds

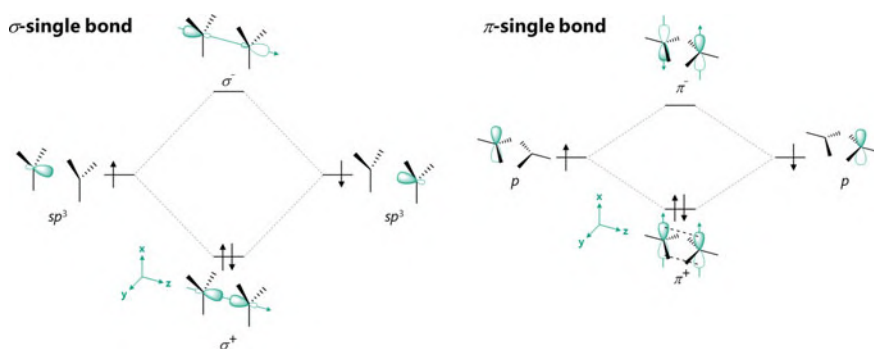
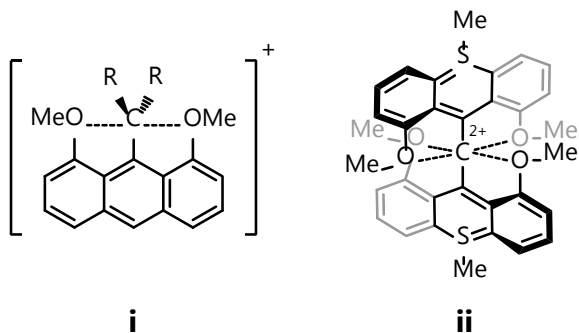


Fig. 1.3 Energy diagram of σ - and π -single bonding

Fig. 1.4 Compounds with hypervalent pentacoordinate or hexacoordinate carbon atom



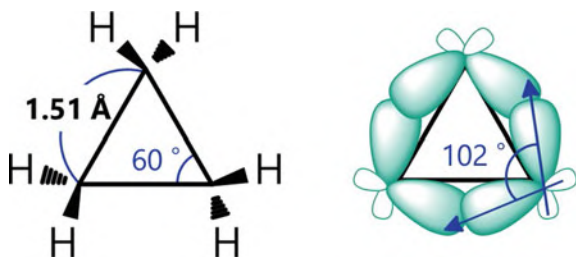
1.3 Short and Long C–C Single Bond

The Csp^3-Csp^3 single bond length is generally 1.54 Å, as in the case of ethane. This standard bond length is observed in almost all compounds [28]. On the other hand, strained compounds may exhibit unusual bonding states. For example, cyclopropane, an equilateral triangular-shaped cyclic hydrocarbon, has a bond angle of 60°, which is far different from the ideal bond angle around a Csp^3 atom (109.5°), and the distance between the carbon atoms is 1.51 Å (Fig. 1.5) [29]. This is because the orbital of the C–C bonds is distributed out of the three-membered ring, resulting in a bent shape of the bond, which is referred to as a bent bond or banana bond. As a result, the s -character (25%) of the C–C bond of cyclopropane is reduced to 18%, which corresponds to “ $sp^{4.5}$ ” hybridization. On the other hand, the hybridization of the C–H bond outside the ring is expressed as “ sp^2 ”, which results in a shorter C–H bond.

By using this strategy of shortening the bond outside of the ring structure, an unusually short C1–C2 bond has been reported in the dimer of tetrahedranes **iii** which is regarded as a cluster of cyclopropanes with a caged structure (Fig. 1.6) [30]. In addition, a contracted bond has also been achieved by steric compression of the C–C bond in a caged molecule **iv**. [31] Despite the approximately 0.1 Å contraction of the C–C single bond, both the C1 and C2 atoms still form four covalent bonds.

In contrast, a longer C1–C2 bond was predicted for hexaphenylethane (HPE) **v** as a result of large steric repulsion among its six phenyl groups. [32] However, the

Fig. 1.5 Bond length, bond angle and bond orbitals of cyclopropane



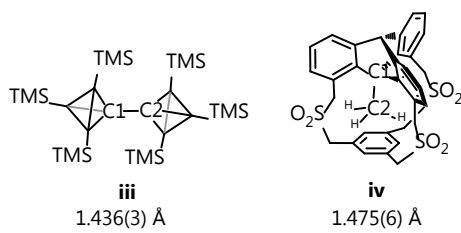
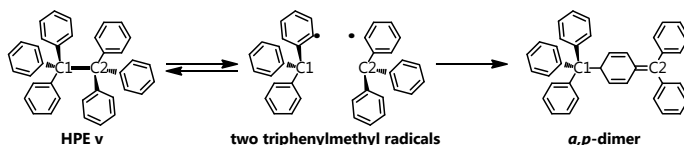


Fig. 1.6 Examples of the molecule with short C–C bond



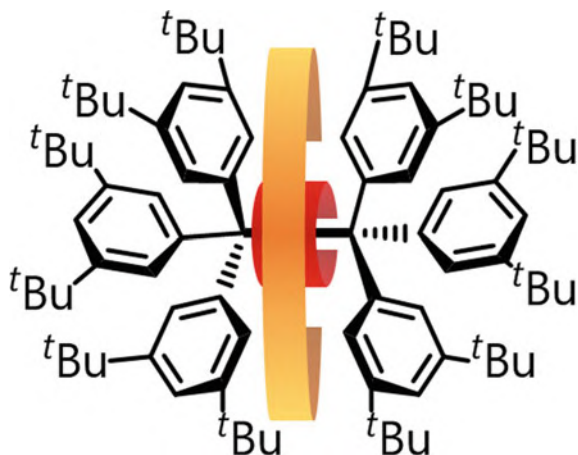
Scheme 1.2 The isomerization mechanism of HPE **v**

parent HPE **v** is not stable because of facile fission of the C1–C2 bond to generate two triphenylmethyl radicals, which finally produces the α,p -dimer, the more stable isomer of HPE (Scheme 1.2) [33].

By preventing α,p -dimer formation, Mislow et al. obtained HPE derivative **vi** with bulky *tert*-butyl groups, which is in equilibrium with the bond-dissociated triarylmethyl radical in solution. The length of the C1–C2 bond (d_I) was determined to be 1.67(3) Å by an X-ray crystal structural analysis [34]. Schreiner et al. indicated that bulky *tert*-butyl groups not only suppress the isomerization from partially generated bond cleavage species by Pauli repulsion, but they also increase thermodynamic stabilization of bonded species by van der Waals dispersion interaction (Fig. 1.7) [35, 36].

Although methano[10]annulene (bisorcaradiene) [37] and anthracene-based [2,2]paracyclophane [38] have been reported to have much longer C–C bonds, those values were later proven to be artifacts because of the coexistence of a bond-dissociated valence isomer. Herges et al. [39] and Toda et al. [40] synthesized **vii** and **viii**, which can be regarded as stabilized HPE derivatives that do not undergo valence isomerization (Fig. 1.8). They are stable compounds because C1–C2 bond fission is suppressed due to sharing of two benzene rings of the HPE framework despite much greater d_I values [1.713(2) and 1.734(5) Å, respectively] than in HPE **vi**. Our group has reported that fused HPEs **ix–xi** have an elongated C–C single bond. Especially, dispiro(acridan)-substituted pyracene (**DSAP**) exhibits the greatest bond length [1.791(3) Å] at 413 K in a single crystal. As well as the HPE-type hydrocarbon **vii**, caged-alkane dimers can also possess an expanded bond, as demonstrated by Schreiner et al. [41]. A d_I value of 1.704(4) Å has been reported for the cross-dimer of triamantane with diamantane **xii**. For these caged-alkane dimers, bond dissociation is hampered by attractive dispersion interactions [41, 42], and the dimers are

Fig. 1.7 Pauli repulsion (red) and dispersion effect (orange) around the C1–C2 of HPE vi



stable even at high temperature. Theoretical calculations for these alkane dimers suggested that there is a limit for d_I (1.803 Å) [1], because the bond dissociation energy (BDE) becomes zero when the two carbon nuclei are separated beyond this distance. A data analysis on the relationship between the C–C single-bond length and BDE also predicted the limit of a C–C single bond [1.748 Å] [2]. In contrast, the shortest non-bonded C...C contact [1.80(2) Å] was observed in [1.1.1]propellane analogue xiii [43].

Thus, on the surface, it seems impossible to synthesize a stable hydrocarbon with a bond of d_I beyond 1.8 Å. Very recently, molecules with a bond length beyond 1.9 Å have been reported. For instance, diaminocarborane xiv contains a C–C three-center two-electron (3c–2e) bonding with a bond length of 1.932(2) Å. In hydrocarbon xv, a bonding interaction beyond 2.0 Å consisting of two *p*-orbitals of C1 and C2 was observed by Kubo et al. However, these examples are not considered to be a pure Csp^3 – Csp^3 single bond composed of two electrons, and thus the nature of an extremely elongated Csp^3 – Csp^3 single bond is not yet clear.

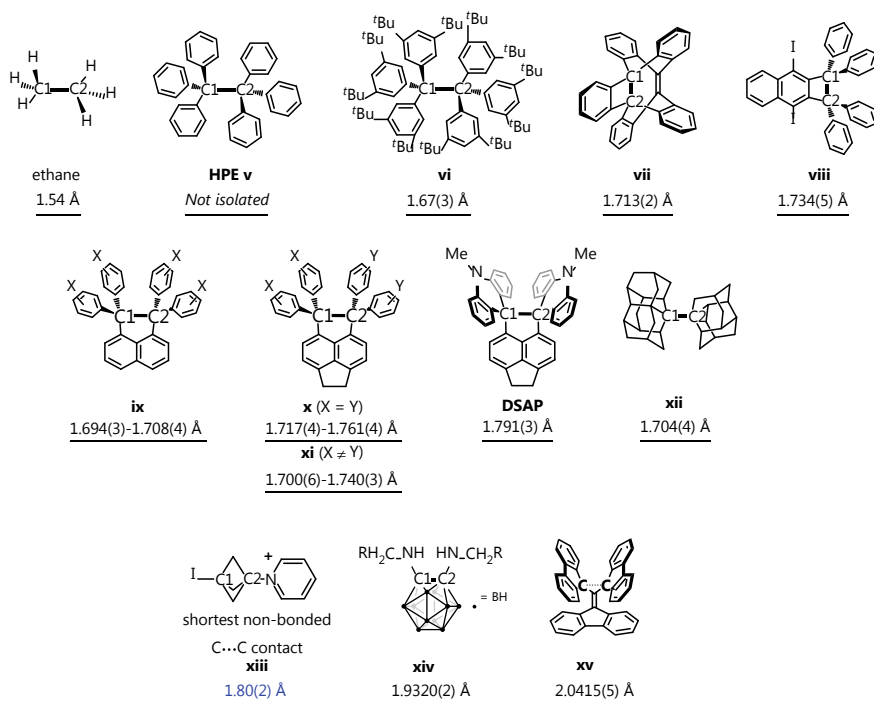


Fig. 1.8 Examples with an unusual distance between C1 and C2 atoms

References

1. D. Cho, Y. Ikabata, T. Yoshikawa, Y.L. Jin, H. Nakai, *Bull. Chem. Soc. Jpn.* **88**, 1636–1641 (2015)
2. A.A. Zavitsas, *J. Phys. Chem. A* **107**, 897–898 (2003)
3. L. Pauling, *The Nature of the Chemical Bond*, 3rd edn. (Cornell University Press, Ithaca, NY, 1960)
4. Compendium of chemical terminology gold book. Int. Union Pure Appl. Chem. (2014)
5. J. Lu, D.M. Ho, N.J. Vogelaar, C.M. Kraml, R.A. Pascal, *J. Am. Chem. Soc.* **126**, 11168–11169 (2004)
6. C.N. Feng, M.Y. Kuo, Y.T. Wu, *Angew. Chem. Int. Ed.* **52**, 7791–7794 (2013)
7. Y. Sakamoto, T. Suzuki, *J. Am. Chem. Soc.* **135**, 14074–14077 (2013)
8. H. Kashiwara, T. Asada, K. Kamikawa, *Chem. A Eur. J.* **21**, 6523–6527 (2015)
9. T. Fujikawa, Y. Segawa, K. Itami, *J. Am. Chem. Soc.* **137**, 7763–7768 (2015)
10. X. Gu, H. Li, B. Shan, Z. Liu, Q. Miao, *Org. Lett.* **19**, 2246–2249 (2017)
11. Y.T. Wu, J.S. Siegel, *Chem. Rev.* **106**, 4843–4867 (2006)
12. A. Sygula, P. W. Rabideau, in *Carbon-Rich Compd.*, eds by M. Haley., R. Tykwinski (Wiley-VCH Verlag GmbH & Co. KGaA, Weinheim, FRG, 2006), pp. 529–565
13. S. Yamago, E. Kayahara, T. Iwamoto, in *Chem. Rec.*, (John Wiley And Sons Inc., 2014), pp. 84–100.
14. T. Iwamoto, E. Kayahara, N. Yasuda, T. Suzuki, S. Yamago, *Angew. Chem. Int. Ed.* **53**, 6430–6434 (2014)
15. E.R. Darzi, R. Jasti, *Chem. Soc. Rev.* **44**, 6401–6410 (2015)

16. P. Li, L.N. Zakharov, R. Jasti, *Angew. Chem. Int. Ed.* **56**, 5237–5241 (2017)
17. H. Isobe, T. Suenaga, Z. Sun, M. Kotani, P. Sarkar, S. Sato, *Proc. Natl. Acad. Sci.* **113**, 8109–8114 (2016)
18. K. Ikemoto, R. Kobayashi, S. Sato, H. Isobe, *Angew. Chem. Int. Ed.* **56**, 6511–6514 (2017)
19. S. Hitosugi, S. Sato, T. Matsuno, T. Koretsune, R. Arita, H. Isobe, *Angew. Chem. Int. Ed.* **56**, 9106–9110 (2017)
20. Y. Segawa, A. Yagi, K. Matsui, K. Itami, *Angew. Chem. Int. Ed.* **55**, 5136–5158 (2016)
21. G. Povie, Y. Segawa, T. Nishihara, Y. Miyauchi, K. Itami, *Science* **356**, 172–175 (2017)
22. S.L. Buchwalter, G.L. Closs, *J. Am. Chem. Soc.* **97**, 3857–3858 (1975)
23. M. Abe, H. Furunaga, D. Ma, L. Gagliardi, G.J. Bodwell, *J. Org. Chem.* **77**, 7612–7619 (2012)
24. Z. Wang, R. Akisaka, S. Yabumoto, T. Nakagawa, S. Hatano, M. Abe, *Chem. Sci.* **12**, 613–625 (2021)
25. M. Yamashita, Y. Yamamoto, K. Akiba, D. Hashizume, F. Iwasaki, N. Takagi, S. Nagase, *J. Am. Chem. Soc.* **127**, 4354–4371 (2005)
26. K. Akiba, M. Yamashita, Y. Yamamoto, S. Nagase, *J. Am. Chem. Soc.* **121**, 10644–10645 (1999)
27. T. Yamaguchi, Y. Yamamoto, D. Kinoshita, K. Akiba, Y. Zhang, C.A. Reed, D. Hashizume, F. Iwasaki, *J. Am. Chem. Soc.* **130**, 6894–6895 (2008)
28. D.G. Watson, L. Brammer, A.G. Orpen, O. Kennard, F.H. Allen, R. Taylor, *J. Chem. Soc. Perkin Trans.* **2**, S1 (2004)
29. A. de Meijere, *Angew. Chem. Int. Ed. Engl.* **18**, 809–826 (1979)
30. M. Tanaka, A. Sekiguchi, *Angew. Chem. Int. Ed.* **44**, 5821–5823 (2005)
31. Q. Song, D.M. Ho, R.A. Pascal, *J. Am. Chem. Soc.* **127**, 11246–11247 (2005)
32. W.D. Hounshell, D.A. Dougherty, J.P. Hummel, K. Mislow, *J. Am. Chem. Soc.* **99**, 1916–1924 (1977)
33. J.M. McBride, *Tetrahedron* **30**, 2009–2022 (1974)
34. B. Kahr, D. Van Engen, K. Mislow, *J. Am. Chem. Soc.* **108**, 8305–8307 (1986)
35. S. Rösel, C. Balestrieri, P.R. Schreiner, *Chem. Sci.* **8**, 405–410 (2016)
36. S. Rösel, J. Becker, W.D. Allen, P.R. Schreiner, *J. Am. Chem. Soc.* **140**, 14421–14432 (2018)
37. R. Bianchi, G. Morosi, A. Mugnoli, M. Simonetta, *Acta Crystallogr. Sect. B Struct. Crystallogr. Cryst. Chem.* **29**, 1196–1208 (1973)
38. M. Ehrenberg, *Acta Crystallogr.* **20**, 182–186 (1966)
39. S. Kammermeier, R. Herges, P.G. Jones, *Angew. Chem. Int. Ed. Engl.* **36**, 1757–1760 (1997)
40. K. Tanaka, N. Takamoto, Y. Tezuka, M. Kato, F. Toda, *Tetrahedron*, 3761–3767 (2001)
41. E.Y. Tikhonchuk, R.M.K. Carlson, J.E.P. Dahl, S. Schlecht, M. Serafin, A.A. Fokin, P.A. Gunchenko, H. Hausmann, L.V. Chernish, P.R. Schreiner, *Nature* **477**, 308–311 (2011)
42. A.A. Fokin, L.V. Chernish, P.A. Gunchenko, E.Y. Tikhonchuk, H. Hausmann, M. Serafin, J.E.P. Dahl, R.M.K. Carlson, P.R. Schreiner, *J. Am. Chem. Soc.* **134**, 13641–13650 (2012)
43. J.L. Adcock, A.A. Gakh, J.L. Pollitte, C. Woods, *J. Am. Chem. Soc.* **114**, 3980–3981 (1992)

Chapter 2

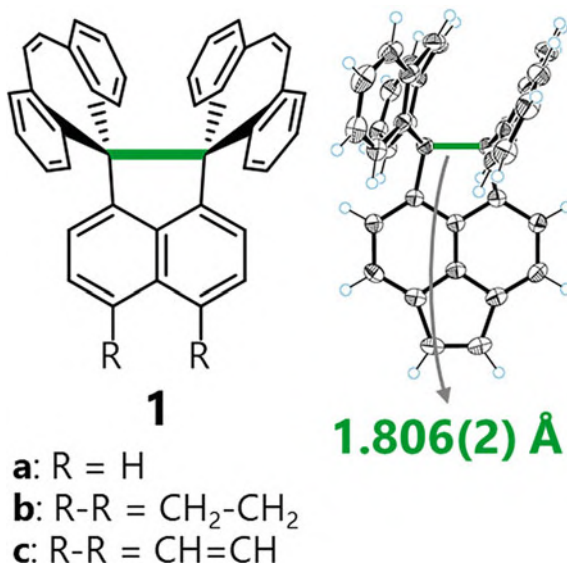
Creation and Demonstration of the Longest C–C Single Bond with a Bond Length Beyond 1.8 Å



2.1 Introduction

On the basis of the “expandability” of the extremely expanded C–C bonds found in other types of hexaphenylethane derivatives (HPEs) **ix** and **x** [1, 2], the author envisaged that much longer C–C bonds could be realized by proper molecular design. The theoretical limit for the C–C bond length d_l was estimated by supposing a linear correlation between bond length and bond dissociation energy (BDE) [3, 4]. However, it has been known for years that through-bond coupling can weaken the bond without changing the bond length [5, 6]. Furthermore, to describe the BDE of an expanded C–C bond, the Lennard–Jones-type potential may be more appropriate rather than a simple linear correlation. Thus, the change in BDE with an increase in the length of pre-strained weak C–C bonds (>1.7 Å) should be smaller than the energy required to lengthen a normal C–C bond (1.54 Å) to the same degree. The author’s group recently found that the expanded bond in some tetraarylpyracenes **xi** (X = OMe, Y = F; X = OMe, Y = H) exhibited quite different values in their pseudo-polymorphs because the bond length can be altered upon the application of a very slight energy change that is compensated by the crystal packing force rather than by the electronic factors of the substituents [7]. The change in the C–C bond length of **DSAP** with a bond length beyond 1.7 Å in a single crystal induced by thermal stimulus was also observed [2]. Therefore, it is highly likely that a C–C bond longer than the theoretically predicted value [3, 4] or the shortest non-bonded C...C contact [1.80(2) Å] in [1.1.1] propellane **xii** [8] can be found when HPE derivatives with greater steric repulsion could be synthesized as stable entities. Herein, to obtain an extremely elongated C–C bond, the author newly proposes the intramolecular “core–shell strategy”: the weak Csp^3 – Csp^3 bond (core) is surrounded and protected by the shape-persistent and chemically inert Csp^2 fused rings (shell) which suppress the dissociation of the expanded bond by π – π interaction between shells. In this chapter, the author designed and synthesized dispiro(dibenzocycloheptatriene)-type HPEs **1a–1c**, where all degradation processes of the weak Csp^3 – Csp^3 bond are hampered to enable their isolation, and thus finally found the longest C–C bond among neutral hydrocarbons (Fig. 2.1).

Fig. 2.1 ORTEP drawing of spiro-DBCHT **1c** at 400 K

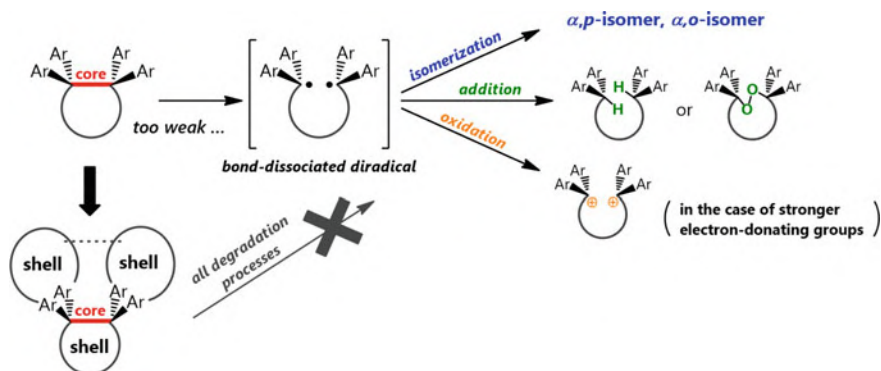


2.2 Results and Discussions

2.2.1 Design Concept

Based on the above-mentioned background, the author sets three key points for the molecular design to create novel hydrocarbons with an unprecedented C–C bond length beyond 1.80 Å, so that the compounds could maintain their chemical stability despite the presence of a very weak C–C bond. To make the compounds stable, all degradation processes, such as isomerization, bond-dissociative addition, bond-dissociative ionization, and diradical formation have to be suppressed. Thus, the author newly proposed an intramolecular core–shell strategy as the first key concept because degradation reactions never occur when the degradation products have higher energy than the compound with an expanded bond. In the intramolecular core–shell strategy, HPE derivatives with a very weak bond (core) could be stabilized by a shape-persistent framework (shell) composed of rigid Csp^2 fused-rings (Scheme 2.1).

The intramolecular core–shell strategy applied on the HPE derivatives also favors bond expansion, because the rigid and bulky “shell” structure is directly connected with the “core”. By increasing the steric repulsion between the shell units, the C–C bond of the core is more expanded. In addition, the author’s group has shown that a “scissor effect” is a reliable structural modification for further expanding the “expandable” weak bond in fused HPE derivatives. Greater bond lengths were observed not only for the C1–C2 bond in **xi** or **xii** compared to that in **x**, but also for the C–O bond in **xvii** or **xviii** compared to that in **xvi** [9] in a single crystal, which can be rationalized by considering the angle strain caused by the ethano or etheno



Scheme 2.1 Intramolecular core–shell strategy could suppress all degradation processes

bridge at the opposite peri position (Fig. 2.2). Thus, the author decided to apply the scissor effect as the second key concept to expand the central C–C bond by attaching the fused ring at the terminal part of the shell.

Restriction of the HPE skeleton to a highly eclipsed conformation ($\sigma \approx 0$) to gain greater “eclipseness” is the third key concept to realize a greater d_1 value, as demonstrated in **ix–xi**: a more eclipsed molecule in the crystal has a greater bond length than a molecule with a less eclipsed geometry [1]. Bridging of the two phenyl rings of the shell structure to form a spiro ring is an effective way for favoring the eclipsed conformation to restrict a rotation of phenyl rings that can lead to the skewed conformation with a less expanded bond by relaxing a steric repulsion. Since **DSAP** in crystal form adopts a nearly eclipsed geometry [2], the precisely determined d_1 value has been considered the longest Csp^3-Csp^3 bond [1.791(3) Å at 413 K] among neutral organic compounds for a while. However, a single crystal of **DSAP** contains another crystallographically independent molecule with a skewed conformation and a smaller d_1 value of 1.719(3) Å. Thus, the more elongated Csp^3-Csp^3 bond should be realized by introducing a larger ring into the shell structures because a large steric

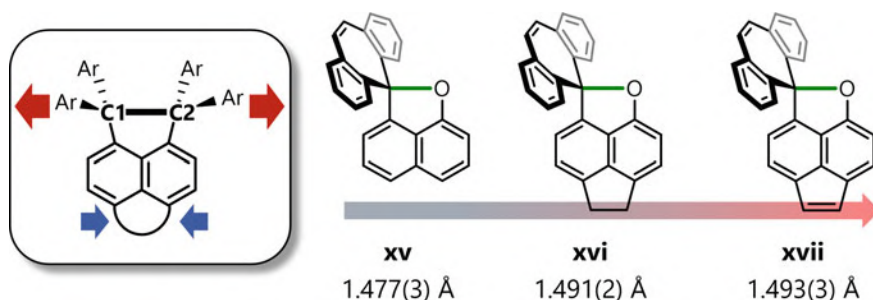


Fig. 2.2 Scissor effect contributes the bond elongation

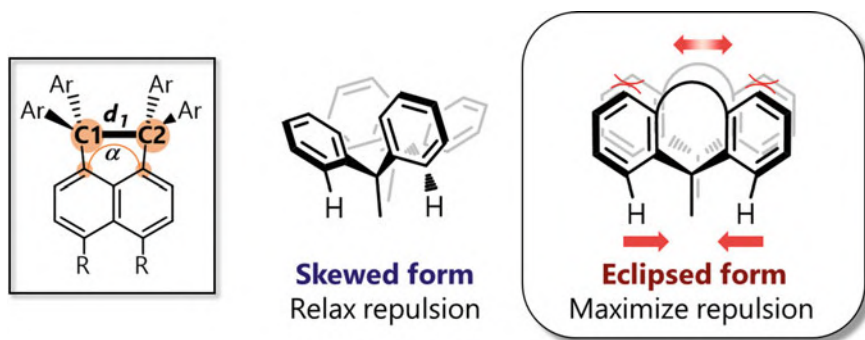


Fig. 2.3 Eclipsed conformation maximizes the steric repulsion to elongate the C–C bond

hindrance between a naphthalene ring and inner protons of the shells could force the molecule to adopt the more eclipsed conformation (Fig. 2.3).

2.2.2 Theoretical Examination for Molecular Design

Initially, the author performed density functional theory (DFT) calculations at the M06-2X/6-31G* level of theory, which includes a dispersion correction. The calculations of **DSAP** revealed that the skewed conformer is the only stable form, and the eclipsed conformer is not found even as a metastable state upon full optimization; thus spiro-cyclization alone is not enough to assure restriction to the eclipsed conformation (Fig. 2.4 and Table 2.1).

After a detailed theoretical examination of a series of compounds, the author found that spiro-fused dibenzocycloheptatriene (DBCHT) is a special shell framework that can favor the eclipsed form of HPEs (Figs. 2.4, 2.5 and Table 2.1). With all the above three concepts, the author designed acenaphthene **1a**, pyracene **1b**, and dihydropyracylene **1c** as novel hydrocarbons. According to DFT calculations at the M06-2X/6-31G* level of theory, they all adopt a completely eclipsed conformation (Fig. 2.5b, d, f) with large d_1 values (Table 2.1) of 1.730, 1.767, and 1.771 Å, respectively. The largest value for **1c** and the larger value for **1b** than for **1a** is due to the scissor effect, because the shorter bridge at the opposite peri position induces greater angle strain on the naphthalene nucleus.

In contrast to the preference for the skewed conformer in **DSAP**, the eclipsed conformer is more stable for **1a–1c** (Fig. 2.4 and Table 2.1), which is due to the DBCHT unit based on the core–shell strategy. A series of calculations, in which the torsion angle of **1c** was fixed, predicted a preference for the eclipsed conformation as well as a greater d_1 value for a more eclipsed conformation. These calculations showed that an unsymmetrical bent geometry for the two spiro rings of the shell structure, which is the outstanding structural feature of spiro-DBCHT **1a–1c**. One spiro ring adopts the well-known folded geometry (containing C1 atom). The concave

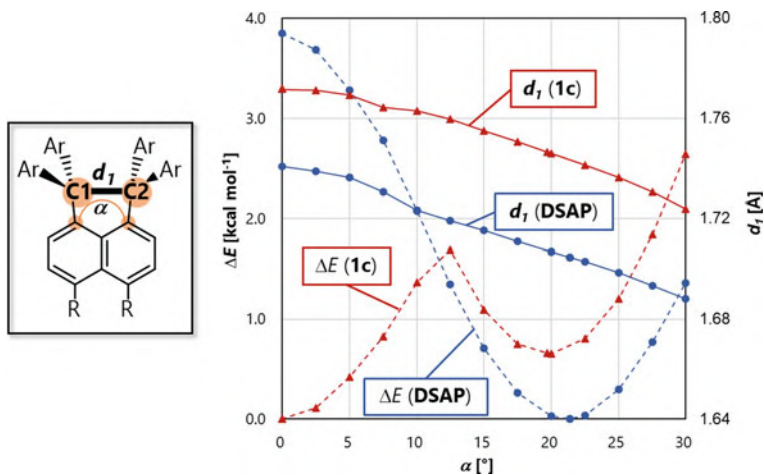


Fig. 2.4 Energy potentials (dotted lines) and d_I values (solid lines) for **1c** (red) and **DSAP** (blue) were calculated by varying the torsion angle α in steps of 2.5° and by considering metastable ($\Delta E = 0.66 \text{ kcal mol}^{-1}$ for **1c**) or the most stable conformations

Table 2.1 Torsion angles α and d_I values of optimized structures for **1a–1c** and **DSAP** predicted by DFT calculations (M06-2X/6-31G*)

| | 1a | 1b | 1c | | DSAP | |
|------------------------|-----------|-----------|-----------|--------|-------------|--------|
| | | | Eclipsed | Skewed | Eclipsed | Skewed |
| α [$^\circ$] | 0 | 0 | 0 | 19.7 | (0) | 21.4 |
| d_I [\AA] | 1.730 | 1.767 | 1.771 | 1.746 | (1.741) | 1.705 |

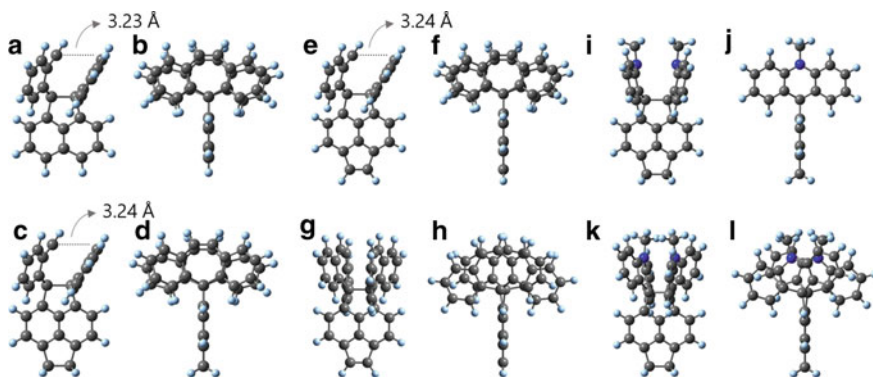


Fig. 2.5 Optimized structures by DFT calculations (M06-2X/6-31G*) for **1a** [(a) front and (b) side views], **1b** [(c) front and (d) side views], **1c** [(e) front and (f) side views], metastable skewed conformer for **1c**; (k) front, (l) side views, eclipsed conformer in DSAP; (g) front, (h) side views, and skewed conformer in DSAP

face of the tub-shaped seven-membered ring faces another spiro unit, which is almost planar geometry (containing C2 atom). In this way, the two spiro units are overlapped in proximity to gain stabilization through π – π interaction (shortest C...C contact between the vinylic carbons of DBCHT units: 3.23 Å for **1a**, 3.24 Å for **1b**, and 3.24 Å for **1c**, Fig. 2.5a, c, e). Because of the folded and compact shape of the shell, any torsional displacement increases the steric repulsion between them and causes some loss of π – π stabilization. This is the reason why spiro-DBCHT **1a–1c** prefer a completely eclipsed geometry.

Such an overlapped geometry of the shells is also the key to maintaining chemical stability. Upon homolytic dissociation of the C1–C2 bond, DBCHT units have to adopt a planar geometry that cannot form a face-to-face stacking arrangement with π – π interaction between the vinylic carbons. The origin of the highly eclipsed conformation was supported by noncovalent interaction (NCI) plots [10] for the optimized structure of **1c** calculated at the M06-2X/6-31G* level of theory, which visualizes the presence of both the attractive and repulsive interactions between neighboring units (Fig. 2.6). The NCI plots exhibit a green surface corresponding to van der Waals (mainly π ... π) interactions between two DBCHT units, and a red surface involving steric hindrance between a naphthalene ring and inner protons of the shells, which indicated that two DBCHT units are interacting with each other in both attractive and repulsive manners to stabilize and elongate the central C–C bond.

Thus, upon conversion of single-bonded **1a–1c** to the corresponding diradicals, not only the BDE but also the stabilization energy through π – π interaction would be lost, making “diradical formation” less favorable. UM06-2X calculations suggest that the bond-dissociated triplet diradical corresponding to **1c** has a higher energy by 20.43 kcal mol⁻¹ without π – π interaction between the vinylic carbons (Fig. 2.7a). Moreover, the diradical of the singlet state has no energy minimum for **1c**, because the DFT calculations started from a bond-dissociated species (C...C distance >3.0 Å) as the initial structure converged to a single-bonded closed-shell species (Fig. 2.7b).

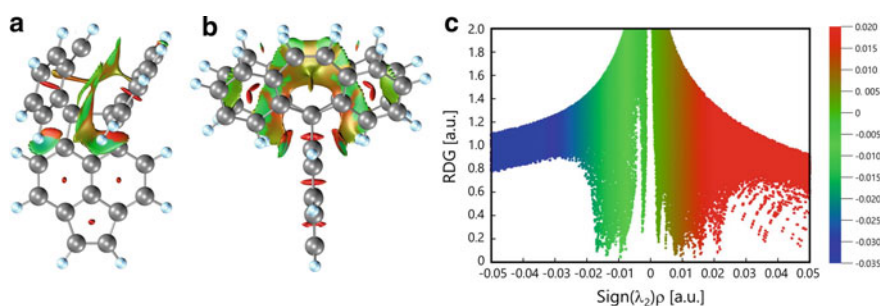


Fig. 2.6 Top (a) and side (b) views of NCI plots (isovalue = 0.5 a.u.) and reduced density gradient (RDG) scattering map (c) for **1c** optimized at M06-2X/6-31G* level of theory. Color online: blue represents strong attractive interactions, green indicates van der Waals interactions, and red indicates repulsive/steric interactions

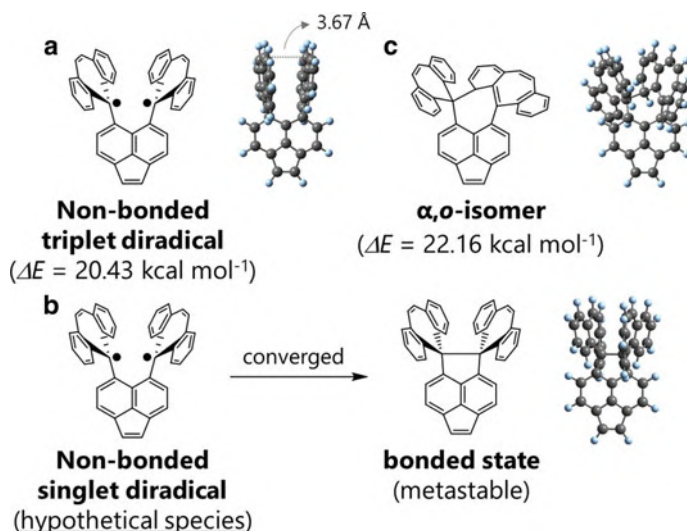
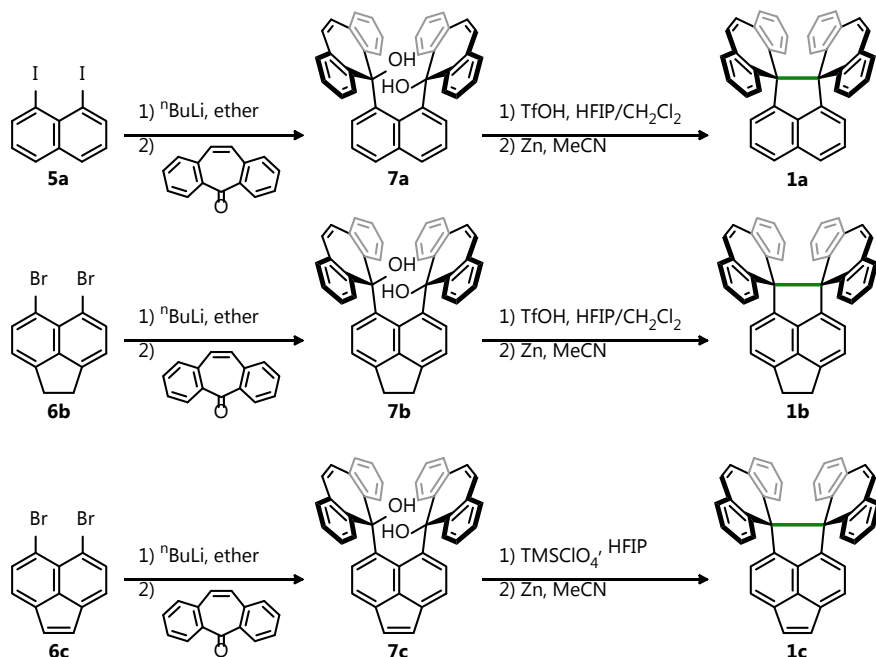


Fig. 2.7 The optimized structures and relative energies of degradation products related to **1c** predicted by DFT calculations (UM06-2X/6-31G*)

Furthermore, for bridged triphenylmethyl radicals, the formation of peroxide or hydrogen abstraction is a representative degradation process (“bond-dissociative addition”) [11, 12]. However, the shell structure of spiro-DBCHT **1a–1c** does not have enough space to accommodate two oxygen bridge or two C–H groups at the peri position between the two DBCHT units. According to DFT calculations, the spiro skeleton induces greater steric repulsion in the corresponding σ , o -type isomer ($\Delta E = 22.16 \text{ kcal mol}^{-1}$; Fig. 2.7c) for **1c**, and thus the “isomerization” of **1c** would not occur because of the shape persistency of the shell. Unlike **DSAP**, which readily undergoes air oxidation to the corresponding bond-dissociated dication [13], the shell structure without any heteroatoms in **1a–1c** is chemically inert and exhibits only limited electron-donating ability, and thus “bond-dissociative oxidation” is less probable.

2.2.3 Preparation of Hydrocarbon **1a–1c**

Based on the above molecular design process assisted by DFT calculations, synthetic studies on spiro-DBCHT **1a–1c** have started. As shown in Scheme 2.2, diols **7a–7c** were obtained in 43–73% yield by lithiation of the corresponding dihalo derivatives **5a–6c** followed by the addition of dibenzosuberone. Diols **7a–7c** were then exposed to acidic conditions [14] in the presence of 1,1,1,3,3,3-hexafluoro-2-propanol (HFIP), and resulting precursor dications **3a²⁺–3c²⁺** were reduced with



Scheme 2.2 Preparation of spiro-DBCHT **1a–1c**

Zn powder to give desired hydrocarbons **1a–1c** in 50–91% yield as colorless crystals for **1a** and **1b** and as an orange crystal for **1c**. The formation of spiro-DBCHT **1a–1c** was confirmed by ^1H NMR and ^{13}C NMR spectra, which show sharp signals assigned to singlet closed-shell species, and high-resolution mass spectra. They all are thermally stable compounds that can be kept under air at ambient temperature; thus, the validity of the intramolecular core–shell strategy the author designed was confirmed regarding the chemical stability.

2.2.4 Raman Spectroscopy

The author first investigated the stretching vibration of the expanded C1–C2 bond by Raman spectroscopy with single crystals of spiro-DBCHT **1a–1c** at 298 K, which gives direct information regarding the force constant of the bond. The experimentally obtained and simulated Raman spectra for these hydrocarbons are shown in Fig. 2.8a–c. The calculated spectra by DFT method very nicely reproduce the experimental results, especially when the B3LYP calculated spectra are scaled with a factor [15] of 0.9613 to consider anharmonicity (Fig. 2.8g–i). The simulated absorption of symmetric C1–C2 stretching vibration in **1c** predicted to have the longest C–C bond among newly prepared hydrocarbons **1a–1c** appeared at 658 cm^{-1} in Fig. 2.8i

(M06-2X/6-31G*), which corresponds to the normal mode with the greatest amplitude along the trajectory of the stretching vibration. The observed Raman shift for the central C–C bond in **1c** is 587 cm^{-1} , which represents a large shift compared with that (993 cm^{-1}) in ethane [16], because the extremely elongated C–C single bond has a much smaller force constant than the ordinary C–C bond (Fig. 2.8c); the estimated force constants (108.3 N m^{-1} for **1c** and 441.0 N m^{-1} for ethane) were obtained as second derivatives of the energy to the bond length by DFT calculations (M06-2X/6-31G*) (Fig. 2.9) [17].

As in the case of **1c**, observed Raman shifts for **1a** and **1b** (650 and 582 cm^{-1} , respectively) are in good agreement with the frequencies for the stretching vibration of the C1–C2 bond determined by M06-2X/6-31G* calculations (724 cm^{-1} for **1a** and 655 cm^{-1} for **1b**) (Fig. 2.8a, j, b, k). The Raman experiments demonstrated that all spiro-DBCHT **1a–1c** have a very weak C1–C2 bond, as predicted by DFT calculations.

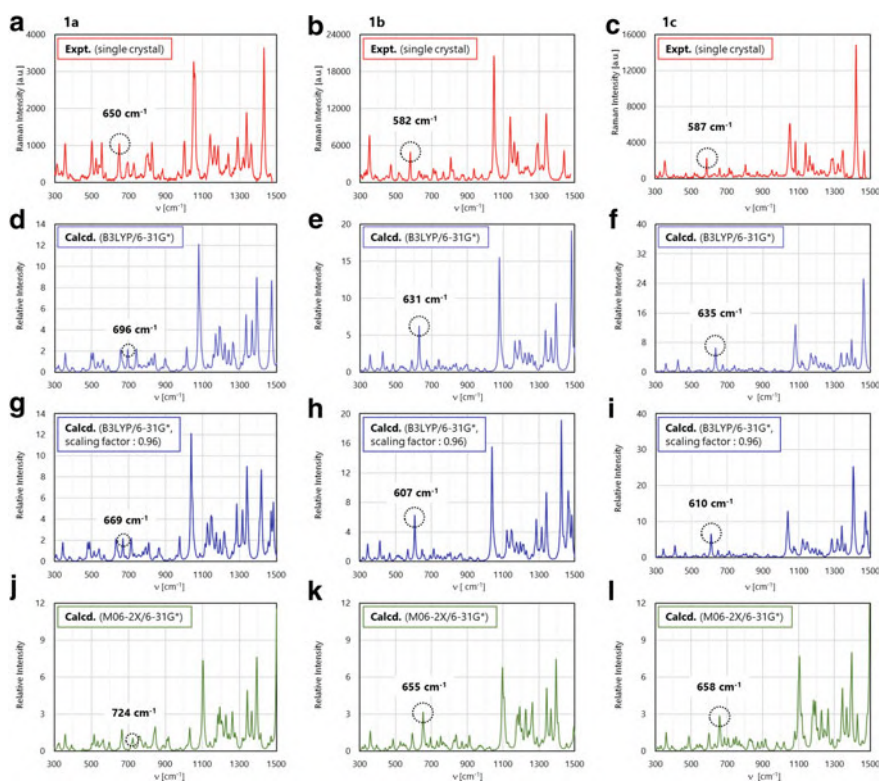


Fig. 2.8 Raman spectra (red) measured by using a single crystal for (a) **1a**, (b) **1b**, and (c) **1c** at 298 K. Simulated spectra predicted by DFT calculations at B3LYP/6-31G* level without scaling (light blue) for (d) **1a**, (e) **1b** and (f) **1c**, at B3LYP/6-31G* level under scaling (blue) for (g) **1a**, (h) **1b** and (i) **1c**, and at M06-2X/6-31G* level without scaling (green) for (j) **1a**, (k) **1b** and (l) **1c**

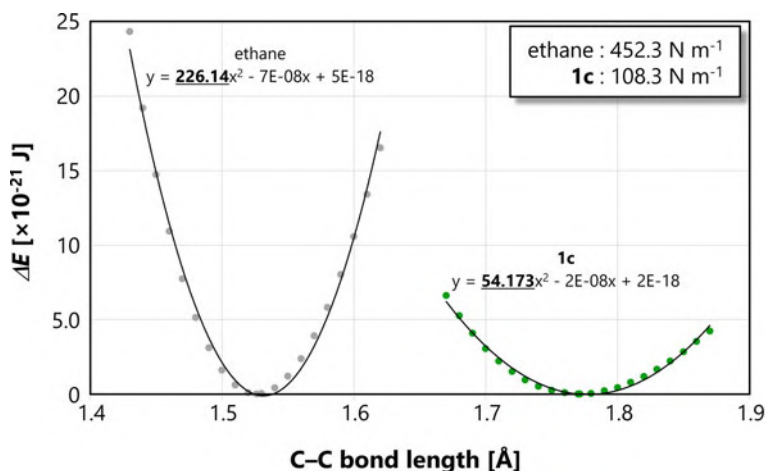


Fig. 2.9 Energy potentials for ethane (black) and **1c** (green) calculated by varying the C1–C2 bond length d_1 in steps of 0.01 Å and by considering the most stable conformation (M06-2X/6-31G*)

2.2.5 Experimentally Determined Bond Length by X-ray Analyses

Next, the author determined the d_1 values in the crystal of these stable hydrocarbons by single-crystal X-ray diffraction. Firstly, X-ray analyses were performed at 200 K to elucidate the precise bond lengths. For **1a**, three crystallographically independent molecules are apparent, all of which adopt a quite similar eclipsed conformation with unsymmetrically bent geometries for the two DBCHT units (Fig. 2.10a–f). The X-ray structure looks very similar to the optimized structure obtained by the above-mentioned DFT calculations. The less symmetrical bent geometry was also observed in crystals of **1b** and **1c** [Fig. 2.10g–j; shortest C...C contact between the vinylic carbons of DBCHT units: 3.25(1), 3.16(1), and 3.23(1) Å for **1a**, 3.19(1) Å for **1b**, and 3.21(1) Å for **1c**]. The d_1 values at 200 K are 1.720(2), 1.723(2), and 1.742(2) Å for **1a**, 1.773(3) Å for **1b**, and 1.7980(18) Å for **1c** (Table 2.2). The value observed in **1c** is greater than that [1.791(3) Å at 413 K] in **DSAP**, which is the previously reported largest value.

As shown in Fig. 2.11 and Table 2.3, the values of bond angles around the C1 and C2 atoms clearly show that these carbon atoms exhibit standard sp^3 hybridization. By considering the π -orbital axis vector (POAV) angles ($\theta_{\sigma\pi}$), which are more often used as an indicator for a structural deformation analysis of an sp^2 carbon atom from planarity [18, 19], these angles of both C1 and C2 atoms are similar to those of the standard Csp^3 carbon, as represented by ethane (109.5°). These results indicate that the C1 and C2 atoms maintain the normal sp^3 hybridization despite their unsymmetrical geometries.

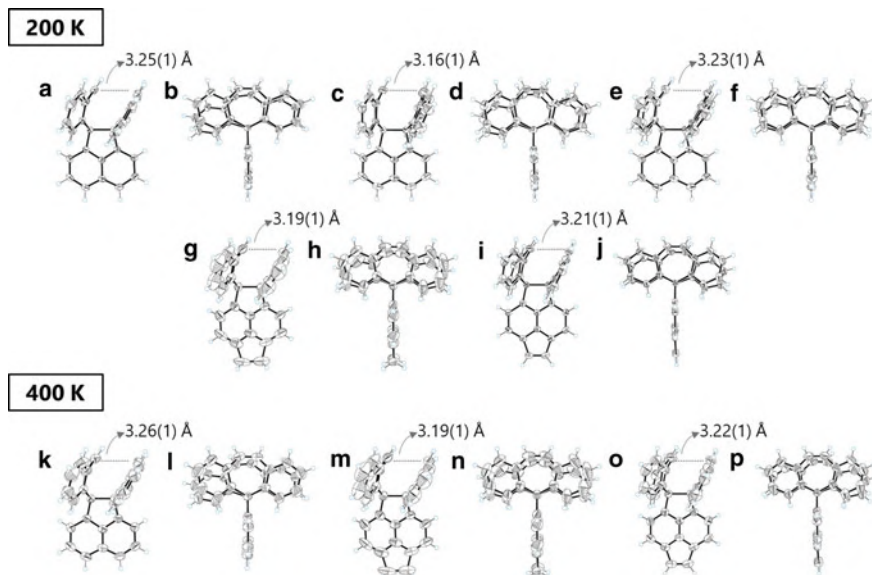


Fig. 2.10 ORTEP drawings at 200 K for **1a** (**a**, **c**, **e**) front, (**b**, **d**, **f**) side views of three crystallographically independent molecules, **1b**; (**g**) front, (**h**) side views and **1c**; (**i**) front, (**j**) side views, and at 400 K for **1a** (**k**) front, (**l**) side views, **1b**; (**m**) front, (**n**) side views and **1c**; (**o**) front, (**p**) side views. At 400 K, three independent molecules of **1a** adopt similar structure, so the other two molecules are omitted for clarity. Thermal ellipsoids are shown at the 50% probability level

Table 2.2 Torsion angles α and d_I values of X-ray structures for **1a–1c**

| Temp. | | 1a | | | 1b | 1c |
|--------------|--------------|-----------|-----------|----------|-----------|-----------------|
| 200 K | α [°] | -3.50(13) | -3.44(14) | 0.38(15) | 0.24(18) | 2.48(10) |
| | d_I [Å] | 1.746(3) | 1.720(2) | 1.723(2) | 1.773(3) | 1.7980(18) |
| 400 K | α [°] | -3.40(16) | -3.20(17) | 0.35(17) | 0.17(18) | 2.68(12) |
| | d_I [Å] | 1.746(3) | 1.723(3) | 1.726(3) | 1.771(3) | 1.806(2) |

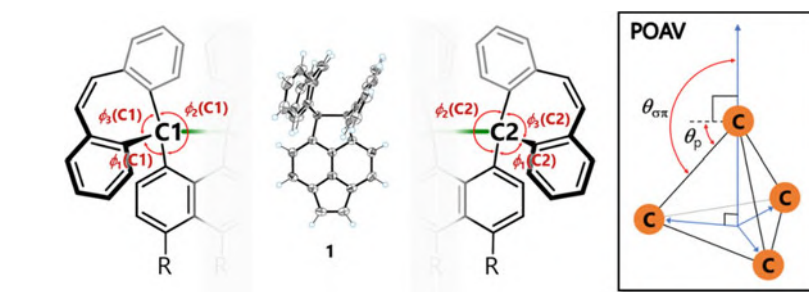


Fig. 2.11 Definition of each angle

Table 2.3 Bond angles ϕ [°] and average of POAV angles $\theta_{\sigma\pi}$ [°] of X-ray structures for **1a–1c**

| | | C1 | | | | C2 | | | |
|-----------|--------------|------------|------------|------------|----------------------|------------|------------|------------|----------------------|
| | | ϕ_1 | ϕ_2 | ϕ_3 | $\theta_{\sigma\pi}$ | ϕ_1 | ϕ_2 | ϕ_3 | $\theta_{\sigma\pi}$ |
| 1a | 200 K mol. 1 | 110.52(13) | 110.89(13) | 110.00(12) | 108.45 | 106.04(11) | 104.53(13) | 122.22(13) | 107.76 |
| | 200 K mol. 2 | 108.35(12) | 109.19(13) | 112.71(13) | 108.84 | 105.94(14) | 105.80(13) | 119.99(13) | 108.20 |
| | 200 K mol. 3 | 110.55(14) | 110.07(14) | 110.58(12) | 108.53 | 104.42(12) | 105.65(13) | 121.25(14) | 108.29 |
| | 400 K mol. 1 | 110.62(15) | 111.04(14) | 109.71(14) | 108.47 | 105.97(13) | 104.85(15) | 122.11(15) | 107.72 |
| | 400 K mol. 2 | 108.56(14) | 108.83(16) | 112.87(15) | 108.84 | 106.49(16) | 105.84(16) | 119.62(15) | 108.14 |
| | 400 K mol. 3 | 110.48(17) | 109.91(17) | 110.62(15) | 108.59 | 104.38(15) | 105.79(16) | 121.44(16) | 108.19 |
| 1b | 200 K | 110.97(17) | 111.69(16) | 110.30(15) | 107.91 | 105.17(16) | 105.41(15) | 122.13(15) | 107.80 |
| | 400 K | 111.0(2) | 111.5(2) | 110.28(17) | 107.97 | 105.11(17) | 105.31(16) | 122.19(18) | 107.83 |
| 1c | 200 K | 110.95(10) | 110.32(9) | 111.53(10) | 107.97 | 106.50(9) | 105.85(10) | 122.1(1) | 107.20 |
| | 400 K | 111.03(12) | 110.28(12) | 111.81(12) | 107.85 | 106.60(12) | 106.07(12) | 121.92(13) | 107.16 |

The Fo–Fc map [20, 21], which visualizes the distribution of electron density based on the X-ray diffraction data, obviously indicates the presence of bonding electrons between C1 and C2 atoms in **1c** (Fig. 2.12a). Although the trends of the bond lengths and their structures by X-ray analyses are in good agreement with those by DFT calculations, the d_I values in the X-ray structures of **1a–1c** are greater than those in the optimized structures. The observed expansion would be accounted for by the shallow energy potential (Fig. 2.9) of the elongated and weak bond with a small BDE.

To investigate the stability of these hydrocarbons in crystal form at elevated temperature, the author carried out variable-temperature (VT) X-ray analyses (from 200 to 400 K every 40 K) by using the same single crystals of **1a–1c** (at 400 K: Fig. 2.10k–p). No degradation was suggested in any of the measurements. Even when the X-ray analyses of **1a–1c** were conducted at 400 K, the estimated standard deviations of the C1–C2 bond length were less than 0.003 Å, indicating that the measurement was highly accurate even at high temperature (Table 2.3).

Moreover, the Fo–Fc map indicates the presence of bonding electrons between C1 and C2 in **1c** even at 400 K (Fig. 2.12b) because of the high accuracy of the X-ray measurements. The thermal ellipsoids of the carbon atoms are still small at 400 K, particularly in **1c** (Fig. 2.10o, p), yet the C1–C2 bonds marginally expand upon heating. Thus, the greatest d_I value of 1.806(2) Å in **1c** was determined at 400 K, which is impressive for an accurately determined C–C bond length. Therefore, the assumed limit for the C–C bond length (1.803 Å) [4] by supposing a linear correlation between the bond length and BDE was proven to be invalid in other types of hydrocarbons including the present examples.

2.2.6 Stability of the Hydrocarbon **1c** with a Very Weak C–C Bond

To gain insight into the stability of weak bonds of d_I greater than 1.80 Å, the author conducted ^1H NMR spectroscopy on **1a–1c** in solution. The ^1H NMR spectrum of **1c** in CDCl_3 at 296 K (Fig. 2.13b) is similar to those of **1a** and **1b**. The spectrum did

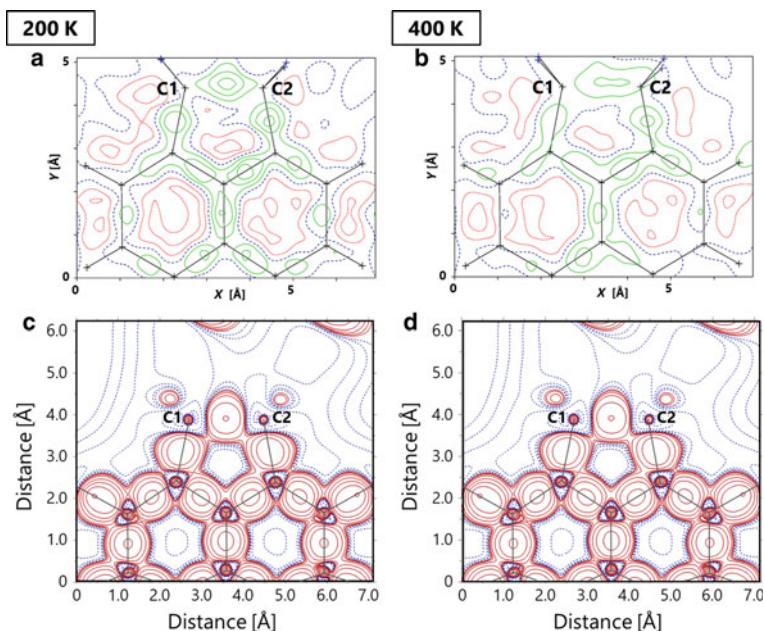


Fig. 2.12 Experimentally obtained Fo–Fc maps around the ultralong C1–C2 bond in **1c** at (a) 200 K and (b) 400 K. The contour interval is $0.05 \text{ e}\text{\AA}^{-3}$: solid lines are positive values (green), and dotted lines are zero (blue) and negative values (red). Theoretically electron deformation maps (B3LYP-D3/6-311+G**) at (c) 200 K and (d) 400 K: red solid lines represent positive value from 0.01 to $0.05 \text{ e}\text{\AA}^{-3}$ in steps of $0.01 \text{ e}\text{\AA}^{-3}$ and from 0.10 to $0.50 \text{ e}\text{\AA}^{-3}$ in steps of $0.05 \text{ e}\text{\AA}^{-3}$. The blue dashed lines represent negative contours from -0.05 to -0.50 in steps of $-0.05 \text{ e}\text{\AA}^{-3}$

not change when the solution was left to stand at ambient temperature for 100 days under air (Scheme 2.3 and Fig. 2.13a). Furthermore, no signs of line broadening and decomposition were observed for signals in the ^1H NMR spectrum of **1c** in $\text{C}_6\text{D}_5\text{Br}$ even at 400 K (Fig. 2.13c), which are assigned to a single species in the singlet state. The spectrum consists of peaks that can be assigned to a single species with C_{2v} symmetry despite the unsymmetrically bent structure in the solid state because a thermal equilibrium with the skewed conformation predicted by the DFT calculations (Figs. 2.4, 2.5 and Table 2.1) is faster than the NMR timescale. No broadening or peak separation occurred even at 190 K in CD_2Cl_2 (Fig. 2.13d), indicating a rapid degenerated conformational change in solution on the NMR timescale.

The same conclusion was reached when the author investigated the ^{13}C NMR spectra of **1a–1c** in CDCl_3 . The spectra showed the signals assigned to the carbon atoms involved in the ultralong bond, which appeared in the quaternary C_{sp^3} region (81.82 ppm for **1a**, 86.30 ppm for **1b**, and 87.46 ppm for **1c**). A slight downfield shift was observed with an increase in the C–C bond length, which keeps the carbon nuclei away from bonding electrons. If the central bond was cleaved, the author would have seen an obvious upfield shift, which was caused by a shielding effect as a result of bond-dissociated radicals.

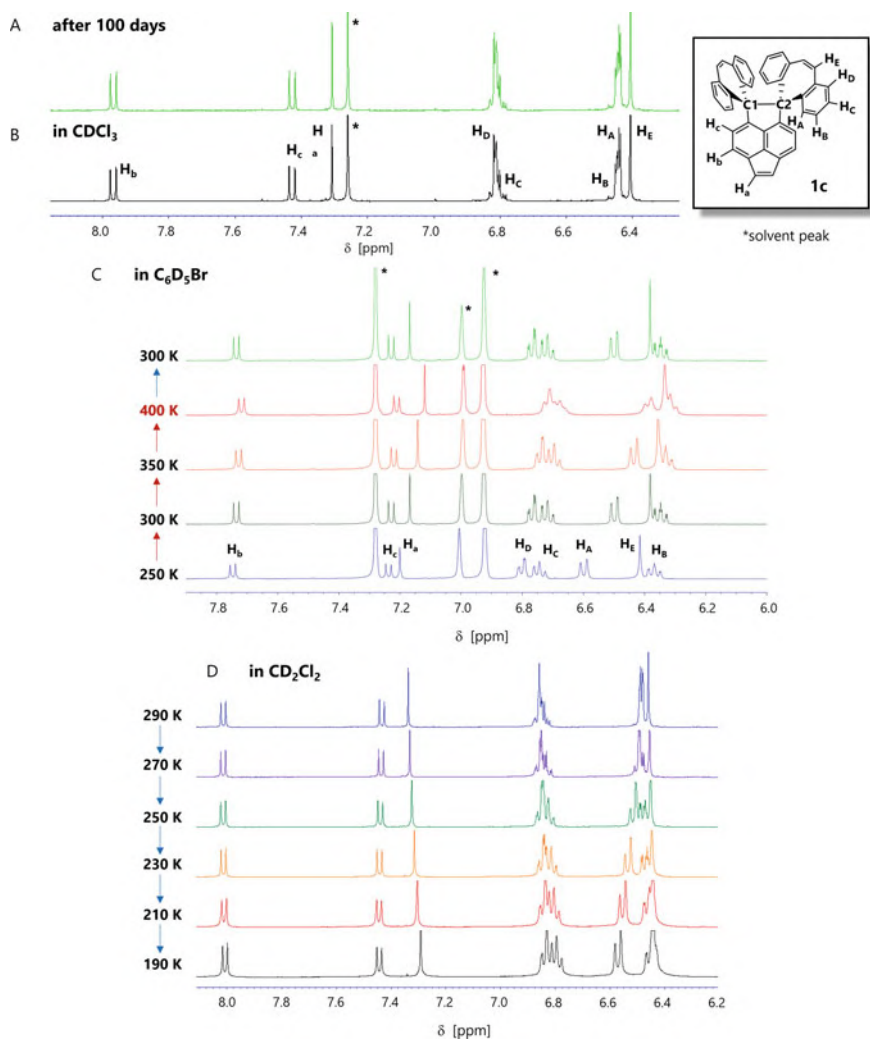
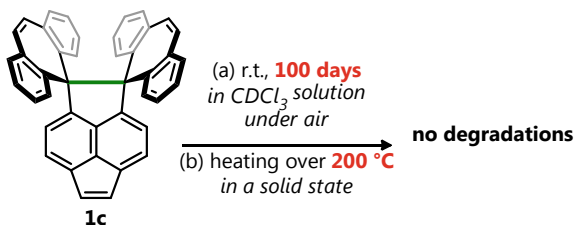
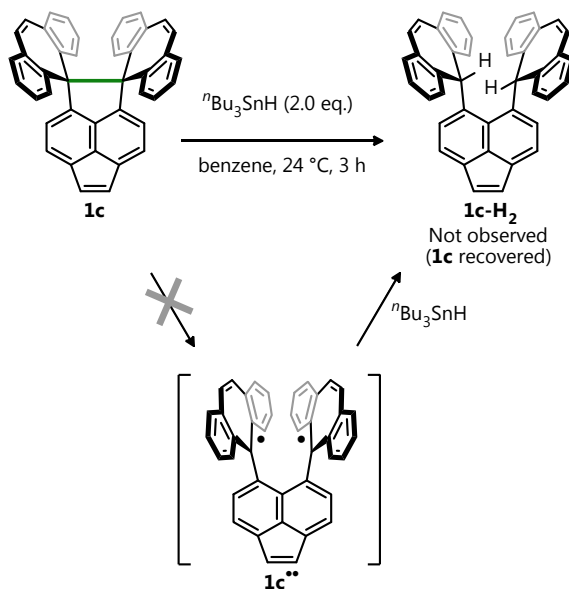


Fig. 2.13 ^1H NMR Spectra of **1c** in CDCl_3 at 296 K (a) after the solution was allowed to stand at ambient temperature for 100 days under air, and (b) before standing. A VT ^1H -NMR spectra of **1c** (c) in $\text{C}_6\text{D}_5\text{Br}$ at higher temperatures and (d) in CD_2Cl_2 at lower temperatures

Scheme 2.3 Investigation of the stability of **1c**



Scheme 2.4 Attempts to trap the bond dissociated species



The absence of diradical contribution was also confirmed by the reaction of **1c** with ${}^n\text{Bu}_3\text{SnH}$. If the long C–C bond in **1c** has some diradical character, the hydrocarbon would react with ${}^n\text{Bu}_3\text{SnH}$ to produce hydrogen adducts [22]. Actually, the starting material was completely recovered, meaning that spiro-DBCHT **1c** does not have a diradical character in solution (Scheme 2.4). These experimental results of ${}^1\text{H}$ and ${}^{13}\text{C}$ NMR spectroscopy and the reaction with ${}^n\text{Bu}_3\text{SnH}$ demonstrated that hydrocarbon **1c** with an ultralong C1–C2 bond is extremely stable both kinetically and thermodynamically, even in solution.

2.2.7 Theoretical Analysis for the Nature of Ultralong C–C Single Bond

The nature of the ultralong C–C single bond beyond 1.80 Å is of interest because this is the first demonstration of the presence of such an elongated bond. The electronic interaction between C1 and C2 atoms was investigated by atoms in molecules (AIM) [23], electron localization function (ELF) [24], and natural bond orbital (NBO) analyses. The results of AIM analysis for **1a–1c** revealed that there is a path of maximum electron density (bond path) between C1 and C2 atoms, partitioned in parts of equal lengths by bond critical points (BCPs; Fig. 2.14). The topological parameters of the BCPs between C1 and C2 atoms for **1a–1c** reflect a slightly reduced electron density ρ , negative total energy H , and negative Laplacian $\nabla^2\rho$, corresponding to shared-shell interaction (Table 2.4) [25]. Maps of the Laplacian of the electron density related to

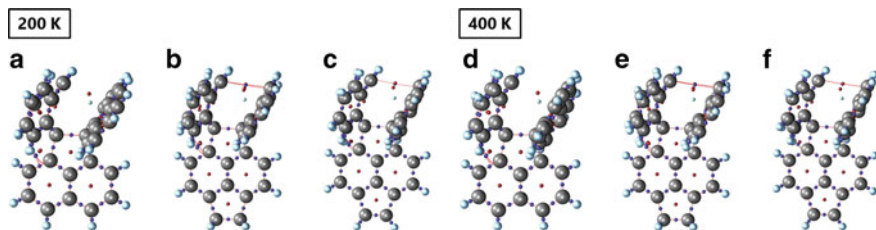


Fig. 2.14 Molecular graphs of (a, d) **1a**, (b, e) **1b** and (c, f) **1c** based on the atom in molecules (AIM) analyses calculated by B3LYP-D3/6-311+G** level of theory at each temperature. Color dots are corresponding to bond critical points (BCPs; blue), ring critical points (RCPs; red), and cage critical points (CCPs; light blue). Crystal structures were elected as an initial structure. Three independent molecules of **1a** adopt similar structure, so the molecule with the longest C–C bond was selected as a representative structure

valence electron for **1c**, which were calculated at the B3LYP-D3/6-311+G** level of theory by using the crystal structure as the initial structure, obviously indicate the presence of bonding electrons between C1 and C2 atoms (Fig. 2.15b, f). As shown in Fig. 2.16a, b, the presence of the C1–C2 bond is also supported by ELF analysis, which shows the localization of electrons: in regions where Pauli repulsion is strong (atomic shells, chemical bonds, lone electron pairs, etc.), the ELF value is close to 1, whereas in the regions where the probability of the same-spin electrons being close is high, the ELF value is close to 0. The maximum value of ELF along the C1–C2 axis is 0.93, indicating the localization of electrons on the ultralong C–C bond (Fig. 2.16c, d).

In addition, the C1–C2 bonding orbital was visualized by NBO analysis based on DFT calculations for **1a–1c** at the B3LYP-D3/6-311+G** level of theory (Fig. 2.17). The bonding orbital of the C1–C2 bond for **1a–1c** is distributed on the C1–C2 axis, which is consistent with the notion that the C1–C2 bond path obtained by AIM linearly connects each atom and certainly exhibits the σ -bonding property. As shown in Table 2.5, the predicted Wiberg bond indexes (WBI) of 0.87 for **1a**, 0.86 for **1b**, and 0.85 for **1c**, respectively, are each smaller than that for ethane (WBI: 1.04). On the other hand, the NBO analysis revealed that the occupancy of the C1–C2 bonding orbital for **1a–1c** is in the range of 1.92–1.93 e, which is only a small decrease (~4%) compared to the ideal value (2.00 e for ethane). The *s*-character of the C1 and C2 atoms for the C1–C2 single bond is 20% for **1a**, 19–20% for **1b**, and 19% for **1c**, respectively. This result can be explained by an increased contribution of the *p*-orbitals away from the nucleus due to the formation of longer bonds. Thus, the extremely elongated C–C bond of **1a–1c** is weak, but maintains the covalently bonding properties with two electrons.

Table 2.4 Topological parameters of the BCPs highlighted in Fig. 2.9. Crystal structure of **1a-1c** and optimized ethane were used for calculations (B3LYP-D3/6-311+G**)

| | 200 K | | | 400 K | | | Ethane | Carborane |
|--|-----------------|-----------|-----------|------------|-----------|-----------|---------|-----------|
| | 1a | 1b | 1c | 1a | 1b | 1c | | |
| | Bond length [Å] | 1.742(2) | 1.773(3) | 1.7980(18) | 1.746(3) | 1.771(3) | | |
| Density of all electrons: ρ_b | 0.1629 | 0.1538 | 0.1469 | 0.1616 | 0.1544 | 0.1444 | 0.2373 | 0.1090 |
| Energy density: $H(\mathbf{r})$ | -0.08810 | -0.07893 | -0.07234 | -0.08682 | -0.07958 | -0.07013 | -0.1864 | -0.0396 |
| Laplacian of electron density: $\nabla^2 \rho$ | -0.2105 | -0.1825 | -0.1625 | -0.2066 | -0.1845 | -0.1555 | -0.5288 | 0.0637 |
| Electron localization function (ELF) | 0.9392 | 0.9354 | 0.9319 | 0.9387 | 0.9357 | 0.9303 | 0.9587 | 0.6230 |
| Localized orbital locator (LOL) | 0.7972 | 0.7920 | 0.7872 | 0.7966 | 0.7923 | 0.7851 | 0.8282 | 0.5625 |
| Ellipticity of electron density ε | 0.01822 | 0.01302 | 0.01073 | 0.01751 | 0.01301 | 0.01054 | 0.0000 | 6.7825 |

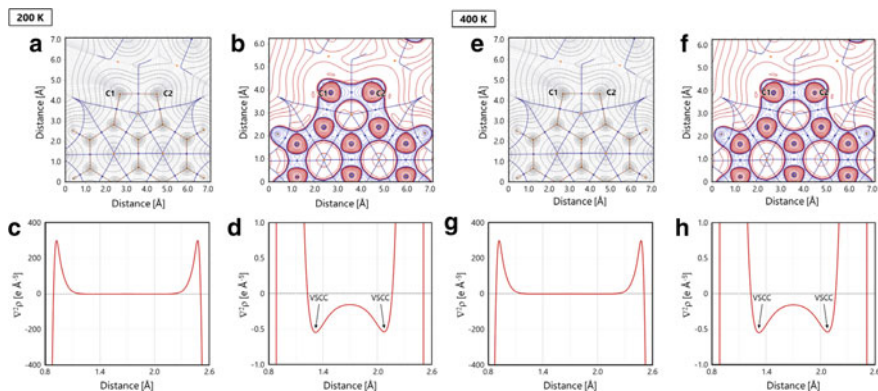


Fig. 2.15 (a, e) Electron density map, and (b, f) 2D- and (c, d, g, h) 1D-Laplacian profiles of electron density $\nabla^2\rho$ around the C1–C2 bond of **1c**. Red solid lines are positive values and blue dotted lines represent negative values

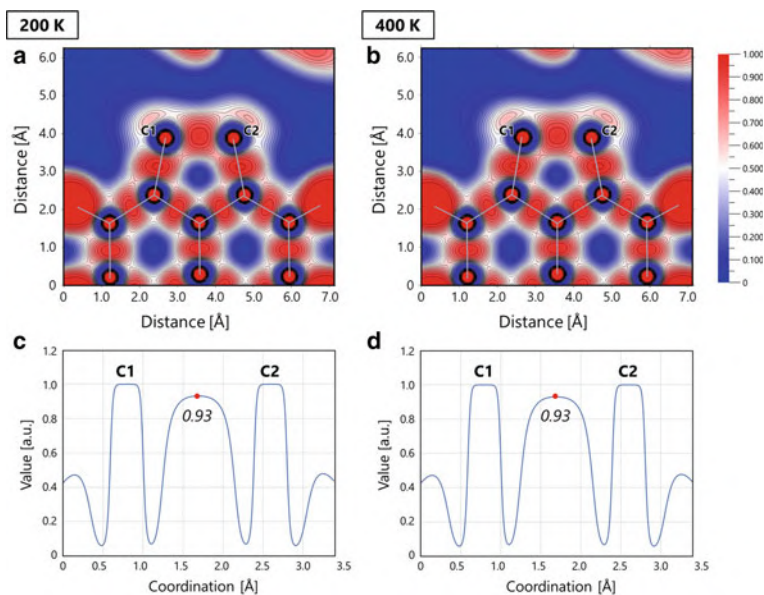


Fig. 2.16 Electron localization function (ELF) maps of **1c** at (a) 200 K and (b) 400 K. 1D-ELF profiles along the C1–C2 bond path of **1c** at (c) 200 K and (d) 400 K

2.3 Conclusion

On the basis of the proposed intramolecular core–shell strategy to make a weak and elongated bond stable enough, the author has designed a series of dispiro(dibenzocycloheptatriene)-type HPE derivatives, **1a–1c**. The weak bond in

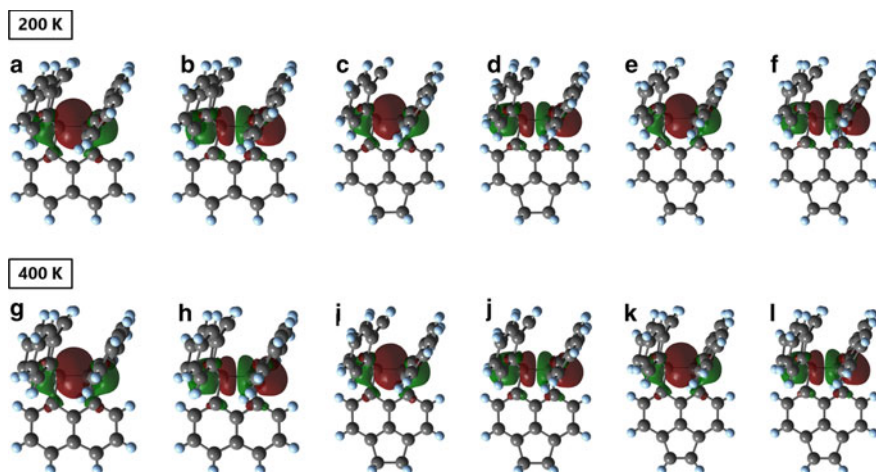


Fig. 2.17 Calculated NBOs between C1 and C2 atoms of **1a** (a, b, g, h), **1b** (c, d, i, j), and **1c** (e, f, k, l) at the B3LYP-D3/6-311+G** level of theory. Crystal structures were elected as an initial structure. Three independent molecules of **1a** adopt similar structure, so the molecule with the longest C–C bond was selected as a representative structure

Table 2.5 NBO analysis parameters of the bonding orbital between C1 and C2 atoms for **1a–1c** at the B3LYP-D3/6-311+G**

| | | 200 K | | | 400 K | | |
|-------------------------|---------------------|-----------|-----------|------------|-----------|-----------|-----------|
| | | 1a | 1b | 1c | 1a | 1b | 1c |
| Bond length [Å] | | 1.742(2) | 1.773(3) | 1.7980(18) | 1.746(3) | 1.771(3) | 1.806(2) |
| Occupancy | | 1.919 | 1.912 | 1.910 | 1.919 | 1.912 | 1.908 |
| WBI | | 0.8604 | 0.8416 | 0.8345 | 0.8594 | 0.8427 | 0.8302 |
| <i>s</i> -character [%] | C1 | 20.40 | 19.47 | 19.16 | 20.36 | 19.55 | 18.83 |
| | C2 | 20.05 | 19.15 | 18.64 | 19.92 | 19.22 | 18.43 |
| NBO-energy [eV] | <i>Bonding</i> | −11.65 | −11.16 | −11.12 | −11.59 | −11.65 | −11.01 |
| | <i>Anti-bonding</i> | 5.551 | 5.491 | 4.922 | 5.852 | 5.551 | 4.816 |

the hydrocarbons the author prepared is expanded by the forced adoption of an eclipsed conformation, which can maximize the steric repulsion around the central C–C bond. For dihydropyracylene derivative **1c**, further expansion was achieved through a scissor effect. The very small Raman shift corresponding to the C–C stretching vibration as well as the greatest d_1 value accurately determined by X-ray analysis revealed that **1c** has a very weak C–C bond. The extensive theoretical studies identified that an extremely elongated C–C bond of **1a–1c** has a small bond index but keeps pure σ -bonded character with two electrons. Nonetheless, **1c** and other dispiro(dibenzocycloheptatriene)s are kinetically and thermodynamically stable entities with no signs of diradical contribution even in solution.

Because the observed value is greater than the shortest non-bonded contact in the [1.1.1] propellane derivative [8], the covalently bonded state and non-bonded state would be seamlessly connected in terms of the interatomic distance. According to the present results, it is highly likely that the author could find an even longer C–C bond (“hyper covalent bond” with a bond length greater than the distance of the shortest non-bonded C...C contact) under the proper molecular design following the intramolecular core–shell strategy.

2.4 Experimental Section

General Procedures

All reactions were carried out under an argon atmosphere. All commercially available compounds were used without further purification unless otherwise indicated. Dry MeCN was obtained by distillation from CaH₂ prior to use. Column chromatography was performed on silica gel I-6-40 (YMC) of particle size 40–63 μm or a silica gel 60N (Kanto, spherical neutral, 40–50 μm). ¹H and ¹³C NMR spectra were recorded on a BRUKER Ascend™ 400 (¹H/400 MHz and ¹³C/100 MHz) spectrometer. IR spectra were measured as a KBr pellet on a JEOL JIR-WINSPEC100 FT/IR spectrophotometer. Mass spectra were recorded on a JEOL JMS-T100GCV spectrometer in FD mode (GC-MS&NMR Laboratory, Research Faculty of Agriculture, Hokkaido University). Melting points were measured on a Yamato MP-21 melting point apparatus and are uncorrected. The analysis of Raman spectroscopy was carried out with in Via Reflex at the OPEN FACILITY, Hokkaido University Sousei Hall. DFT calculations were performed with the Gaussian 09W [26] and 16W [27] program package. The geometries of the compounds were optimized by using the M06-2X method in combination with the 6-31G* basis set unless otherwise indicated. Version 3.8 of the Multiwfn software [28] was used for topological analysis of the electron density that is obtained by DFT calculations. The NBO analyses were performed with the Version 7.0 of the NBO [29] which was implemented in the Gaussian 16W program. The atomic coordinates were obtained from crystal structures of **1a–1c** at each temperature and the wave function was calculated at B3LYP-D3/6-311+G** for Laplacian maps, AIM, NBO, and ELF analyses.

Preparation

- Preparation of hydrocarbons **1a–1c**

5,6-Dibromoacenaphthene **6b**

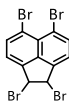


6b

To a suspension of acenaphthene (5.00 g, 32.4 mmol) in DMF (20 mL) was added a suspension of N-bromosuccinimide (NBS, 12.7 g, 71.5 mmol) in DMF (20 mL) at 0 °C. The mixture was stirred at 23 °C for 21 h in the dark, cooled to 0 °C, and filtered to obtain the crude product. To the crude solid was added EtOH (30 mL), and the suspension was refluxed for 21 h. After cooling to 22 °C, the resulting precipitates were filtered and washed with EtOH to give **6b** (1.58 g, 16%) as a pink solid.

¹H NMR data were identical to those in literature [30].

1,2,5,6-Tetrabromoacenaphthene **6b-Br₂**



6b-Br₂

A mixture of **6b** (1.00 g, 3.21 mmol), NBS (1.26 g, 7.05 mmol), and benzoyl peroxide (201 mg, 858 μmol) in CHCl₃ (40 mL) was refluxed for 5 h. After cooling to 25 °C, the resulting solution was diluted with water and extracted with CHCl₃. The organic layer was washed with water, saturated NaHCO₃ aq. and brine, and dried over MgSO₄. After filtration, the solvent was concentrated under reduced pressure. The residue was purified by column chromatography on silica gel (hexane only) to give **6b-Br₂** (872 mg, 58%) as a yellow solid.

¹H NMR data were identical to those in literature [31].

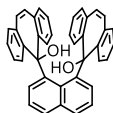
1,8-Dibromoacenaphthylene **6c**



6c

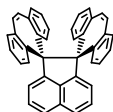
A mixture of **6b-Br₂** (2.00 g, 4.26 mmol) and nonactivated Zn powder (835 mg, 12.8 mmol) in AcOH (200 mL) was refluxed for 1 h. After cooling to 24 °C, the resulting suspension was diluted with water and extracted with CHCl₃. The organic layer was washed with water, saturated NaHCO₃ aq. and brine, and dried over MgSO₄. After filtration, the solvent was concentrated under reduced pressure. The residue was purified by column chromatography on silica gel (hexane only) to give **13c** (1.24 g, 94%) as a yellow solid.

¹H NMR data were identical to those in literature [31].

1,8-Bis(5-hydroxydibenzo[*a,d*]cycloheptatrien-5-yl)naphthalene 7a**7a**

To a suspension of 1,8-diiodonaphthalene (999 mg, 2.63 mmol) in dry ether (100 mL) was added ⁿBuLi in hexane (1.55 M, 4.07 mL, 6.31 mmol) at 24 °C. After stirring for 1 h at 24 °C, dibenzosuberone (1.30 g, 6.31 mmol) was added and the mixture was refluxed for 4 h. Then, the mixture was cooled to 24 °C, and diluted with water. The resulting mixture was extracted with CHCl₃. The organic layer was washed with water and brine, and dried over MgSO₄. After filtration, the solvent was concentrated under reduced pressure. The residue was purified by reprecipitation (CHCl₃/hexane) and column chromatography on silica gel (CHCl₃/hexane = 1.5) to give **7a** (844 mg, 59%) as a colorless solid.

mp: 282–288 °C (decomp.); ¹H NMR (CDCl₃): δ 8.04 (dd, *J* = 1.2, 8.0 Hz, 2H), 7.93 (dd, *J* = 1.3, 8.1 Hz, 2H), 7.72 (ddd, *J* = 1.3, 8.0, 8.6 Hz, 2H), 7.41 (ddd, *J* = 1.2, 7.6, 8.6 Hz, 2H), 7.36 (dd, *J* = 1.1, 7.5 Hz, 2H), 7.23 (ddd, *J* = 1.4, 8.1, 8.6 Hz, 2H), 7.06 (dd, *J* = 1.3, 7.6 Hz, 2H), 6.98 (ddd, *J* = 1.3, 7.5, 8.6 Hz, 2H), 6.90 (t, *J* = 7.5 Hz, 2H), 6.74 (dd, *J* = 1.4, 7.5 Hz, 2H), 6.70 (dd, *J* = 1.1, 7.5 Hz, 2H), 5.63 (d, *J* = 11.4 Hz, 2H), 5.56 (d, *J* = 11.4 Hz, 2H), 1.25 (s, 2H); ¹³C NMR (CDCl₃): δ 149.11, 139.33, 138.93, 134.64, 133.03, 132.66, 132.00, 131.87, 129.94, 129.59, 128.18, 128.11, 127.71, 127.68, 127.42, 126.79, 125.90, 125.34, 122.81, 121.73, 79.39; IR (KBr): 3551, 3061, 3048, 1920, 1621, 1595, 1482, 1433, 1312, 1219, 1152, 1119, 1050, 1038, 1002, 813, 801, 789, 769, 755, 743, 648 cm⁻¹; LR-MS (FD) *m/z* (%): 542.19 (10), 541.19 (46), 540.19 (M⁺, bp); HR-MS (FD): [M⁺] calcd. for C₄₀H₂₈O₂, 540.20893; found, 540.20837.

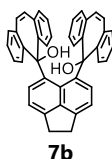
Dispiro[(dibenzo[*a,d*]cycloheptatriene)-5,1'-acenaphthene-2',5''-(dibenzo[*a,d*]cycloheptatriene)]1a**1a**

To a suspension of **7a** (99.9 mg, 185 μmol) in dry CH₂Cl₂ (3 mL) and 1,1,1,3,3,3-hexafluoro-2-propanol (HFIP, 3 mL) was added trifluoromethanesulfonic acid (TfOH, 160 μL, 1.81 mmol) at 25 °C. The mixture was stirred for 1 h, and the solvent was evaporated. To the residue were added dry MeCN (10 mL) and activated Zn powder (1.81 g, 27.7 mmol) at 25 °C. After stirring for 1 h at 25 °C, the mixture

was diluted with water, and extracted with CHCl_3 . The organic layer was washed with water and brine, and dried over MgSO_4 . After filtration, the solvent was concentrated under reduced pressure. The residue was purified by column chromatography on silica gel (hexane/ $\text{CHCl}_3 = 5$) to give **1a** (85.0 mg, 91%) as a colorless solid.

mp: 245–249 °C (decomp.); ^1H NMR (CDCl_3): δ 7.92 (dd, $J = 0.7, 8.1$ Hz, 2H), 7.69 (dd, $J = 7.1, 8.1$ Hz, 2H), 7.30 (dd, $J = 0.7, 7.1$ Hz, 2H), 6.83–6.78(m, 8H), 6.46 (ddd, $J = 3.5, 5.0, 8.5$ Hz, 4H), 6.39 (s, 4H), 6.38 (br. d, $J = 8.5$ Hz, 4H); ^{13}C NMR (CDCl_3): δ 152.48, 141.18, 138.15, 136.08, 134.04, 132.47, 130.80, 130.67, 128.41, 126.98, 126.11, 125.69, 123.53, 81.82; IR (KBr): 3107, 3048, 3029, 2925, 1944, 1620, 1594, 1581, 1495, 1489, 1431, 878, 806, 796, 766, 722, 645 cm^{-1} ; LR-MS (FD) m/z (%): 508.20 (9), 507.20 (43), 506.20 (M^+ , bp); HR-MS (FD): [M^+] calcd. for $\text{C}_{40}\text{H}_{26}$, 506.20345; found, 506.20193.

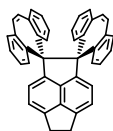
5,6-Bis(5-hydroxydibenzo[*a,d*]cycloheptatrien-5-yl)acenaphthene **7b**



To a suspension of 5,6-dibromoacenaphthene **6b** (5.00 g, 16.0 mmol) in dry ether (200 mL) was added $n\text{BuLi}$ in hexane (1.60 M, 24.0 mL, 38.4 mmol) at 25 °C. The mixture was stirred for 1 h at 25 °C, and added dibenzosuberone (7.94 g, 38.5 mmol) was added. After stirring for 18 h at 25 °C, the mixture was diluted with water, and extracted with CH_2Cl_2 . The organic layer was washed with water and brine, and dried over Na_2SO_4 . After filtration, the solvent was concentrated under reduced pressure. The residue was purified by reprecipitation (CHCl_3 /hexane) and short column chromatography on silica gel (CH_2Cl_2) to give **7b** (6.66 g, 73%) as a colorless solid.

mp: 264–273 °C (decomp.); ^1H NMR (CDCl_3): δ 7.99 (dd, $J = 1.2, 7.9$ Hz, 2H), 7.94 (dd, $J = 1.2, 7.9$ Hz, 2H), 7.70 (ddd, $J = 1.3, 7.9, 8.7$ Hz, 2H), 7.39 (ddd, $J = 1.2, 7.5, 8.7$ Hz, 2H), 7.26 (ddd, $J = 1.3, 7.9, 8.6$ Hz, 2H), 7.07 (dd, $J = 1.3, 7.5$ Hz, 2H), 6.99 (ddd, $J = 1.2, 7.5, 8.6$ Hz, 2H), 6.77 (dd, $J = 1.3, 7.5$ Hz, 2H), 6.73 (d, $J = 7.4$ Hz, 2H), 6.62 (d, $J = 7.4$ Hz, 2H), 5.68 (d, $J = 11.4$ Hz, 2H), 5.59 (d, $J = 11.4$ Hz, 2H), 3.30–3.13 (m, 4H), 1.07 (s, 2H); ^{13}C NMR (CDCl_3): δ 149.59, 145.90, 139.70, 138.33, 135.49, 134.92, 134.34, 132.00, 131.39, 130.37, 129.19, 128.06, 127.69, 127.35, 126.60, 126.29, 125.20, 121.72, 116.94, 79.12, 29.83; IR (KBr): 3553, 3059, 3018, 3001, 2932, 1597, 1480, 1446, 1435, 1311, 1217, 1154, 1034, 1022, 790, 770, 763, 653 cm^{-1} ; LR-MS (FD) m/z (%): 568.21 (12), 567.20 (47), 566.20 (M^+ , bp); HR-MS (FD): [M^+] calcd. for $\text{C}_{42}\text{H}_{30}\text{O}_2$, 566.22458; found, 566.22575.

Dispiro[(dibenzo[*a,d*]cycloheptatriene)-5,1'-pyracene-2',5''-(dibenzo[*a,d*]cycloheptatriene)] **1b**

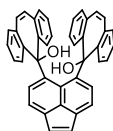


1b

To a suspension of **7b** (1.32 g, 2.32 mmol) in HFIP (5 mL) and dry CH₂Cl₂ (5 mL) was added TfOH (2.10 mL, 23.9 mmol) at 24 °C. The mixture was stirred for 2 h at 24 °C, and the solvent was evaporated. To the residue were added dry MeCN (20 mL), and activated Zn powder (22.8 g, 348 mmol). After stirring for 2 h at 24 °C, the mixture was diluted with water, and extracted with CH₂Cl₂. The organic layer was washed with water and brine, and dried over Na₂SO₄. After filtration, the solvent was concentrated under reduced pressure. The residue was purified by short column chromatography on silica gel (CH₂Cl₂) to give **1b** (1.07 g, 87%) as a colorless solid.

mp: 250–260 °C (decomp.); ¹H NMR (CDCl₃): δ 7.46 (d, *J* = 7.0 Hz, 2H), 7.27 (d, *J* = 7.0 Hz, 2H), 6.81–6.77 (m, 8H), 6.54 (br. d, *J* = 8.4 Hz, 4H), 6.46 (ddd, *J* = 3.6, 4.9, 8.4 Hz, 4H), 6.38 (s, 4H), 3.63 (s, 4H); ¹³C NMR (CDCl₃): δ 147.22, 142.18, 141.19, 137.88, 136.65, 135.67, 133.76, 132.55, 130.48, 127.87, 126.13, 125.53, 121.25, 86.30, 31.83; IR (KBr): 3107, 3027, 2917, 1919, 1623, 1496, 1428, 1068, 877, 840, 808, 799, 769, 724, 690, 646 cm⁻¹; LR-MS (FD) *m/z* (%): 534.21 (11), 533.20 (49), 532.20 (M⁺, bp); HR-MS (FD): [M⁺] calcd. for C₄₂H₂₈, 532.21910; found, 532.21825.

5,6-Bis(5-hydroxydibenzo[*a,d*]cycloheptatrien-5-yl)acenaphthylene **7c**

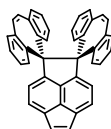


7c

To a suspension of 5,6-dibromoacenaphthylene **6c** (60.3 mg, 1.94 mmol) in dry ether (50 mL) was added ⁿBuLi in hexane (1.64 M, 2.80 mL, 4.67 mmol) at 25 °C. After stirring for 1 h at 25 °C, dibenzosuberone (96.4 mg, 4.67 mmol) was added, and the mixture was refluxed for 5 h. Then, the mixture was cooled to 25 °C, and diluted with water. The resulting mixture was extracted with CHCl₃. The organic layer was washed with water and brine, and dried over MgSO₄. After filtration, the solvent was concentrated under reduced pressure. The residue was purified by reprecipitation (CHCl₃/hexane) and column chromatography on silica gel (hexane/EtOAc = 10) to give **7c** (46.9 mg, 43%) as a pale yellow solid.

mp: 281–290 °C (decomp.); ^1H NMR (CDCl_3): δ 7.99 (dd, $J = 1.2, 8.0$ Hz, 2H), 7.92 (dd, $J = 1.2, 8.1$ Hz, 2H), 7.71 (ddd, $J = 1.3, 8.0, 8.7$ Hz, 2H), 7.41 (ddd, $J = 1.2, 7.5, 8.7$, 2H), 7.27 (ddd, $J = 1.3, 8.1, 8.6$ Hz, 2H), 7.09 (dd, $J = 1.3, 7.5$ Hz, 2H), 7.02 (ddd, $J = 1.2, 7.5, 8.6$ Hz, 2H), 7.00 (d, $J = 7.2$ Hz, 2H), 6.80 (dd, $J = 1.3, 7.5$ Hz, 2H), 6.71 (s, 2H), 6.65 (d, $J = 7.2$ Hz, 2H), 5.73 (d, $J = 11.4$ Hz, 2H), 5.69 (d, $J = 11.4$ Hz, 2H), 1.11 (s, 2H); ^{13}C NMR (CDCl_3): δ 149.11, 142.13, 139.73, 139.42, 134.60, 134.48, 132.04, 130.83, 130.24, 129.67, 128.756, 128.32, 128.09, 127.79, 127.51, 127.40, 126.84, 126.01, 125.44, 121.70, 121.46, 79.15; IR (KBr): 3558, 3059, 3018, 2922, 1620, 1596, 1477, 1434, 1315, 1218, 1152, 1132, 1037, 836, 792, 761, 746, 671, 656 cm^{-1} ; LR-MS (FD) m/z (%): 566.20 (13), 565.20 (46), 564.19 (M^+ , bp), 547.18 (11), 546.18 (19); HR-MS (FD): [M^+] calcd. for $\text{C}_{42}\text{H}_{28}\text{O}_2$, 564.20893; found, 564.20734.

Dispiro[(dibenzo[*a,d*]cycloheptatriene)-5,1'-(1',2'-dihydropyracylene)-2',5''-(dibenzo[*a,d*]cycloheptatriene)] **1c**

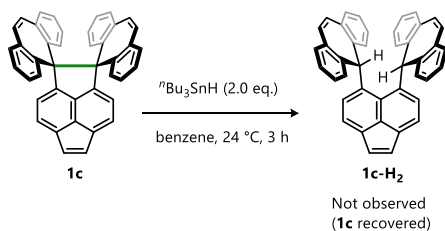


1c

To a suspension of **7c** (188 mg, 332 μmol) in HFIP (6 mL) was added TMSClO_4 in toluene (0.79 M, 1.70 mL, 1.33 mmol) at 24 °C. The mixture was stirred for 1 h at 24 °C, and the solvent was evaporated. To the residue were added dry MeCN (20 mL) and activated Zn powder (3.27 g). After stirring for 30 min at 24 °C, the mixture was diluted with water, and extracted with CHCl_3 . The organic layer was washed with water and brine, and dried over MgSO_4 . After filtration, the solvent was concentrated under reduced pressure. The residue was purified by reprecipitation ($\text{CHCl}_3/\text{MeOH}$) and column chromatography on silica gel (hexane/ $\text{CHCl}_3 = 5$) to give **1c** (77.8 mg, 50%) as a yellow solid.

mp: 250–258 °C (decomp.); ^1H NMR (CDCl_3): δ 7.97 (d, $J = 7.1$ Hz, 2H), 7.43 (d, $J = 7.1$ Hz, 2H), 7.31 (s, 2H), 6.83–6.78 (m, 8H), 6.46–6.43 (m, 8H), 6.41 (s, 4H); ^{13}C NMR (CDCl_3): δ 153.22, 140.70, 136.04, 135.66, 133.72, 132.57, 130.69, 129.43, 127.64, 127.01, 126.24, 125.99, 125.78, 87.46; ^1H NMR (CD_2Cl_2): δ 8.01 (d, $J = 7.1$ Hz, 2H), 7.43 (d, $J = 7.1$ Hz, 2H), 7.34 (s, 2H), 6.89–6.80 (m, 8H), 6.52–6.47 (m, 8H), 6.46 (s, 4H); ^{13}C NMR (CD_2Cl_2): δ 153.18, 140.76, 136.14, 135.65, 133.65, 133.61, 132.52, 130.64, 129.37, 127.57, 126.85, 126.19, 126.02, 125.72, 87.30; IR (KBr): 3037, 2923, 2853, 1924, 1619, 1488, 1466, 1419, 1083, 953, 846, 835, 770, 724, 719, 677, 646 cm^{-1} ; LR-MS (FD) m/z (%): 532.20 (12), 531.20 (M^+ , bp); HR-MS (FD): [M^+] calcd. for $\text{C}_{42}\text{H}_{26}$, 530.20345; found, 530.20345.

- Attempts to trap the bond dissociated species.



To a suspension of **1c** (20.0 mg, 37.7 μmol) in benzene (4 mL) was added $n\text{Bu}_3\text{SnH}$ (20 μL , 744 μmol) at 24 $^\circ\text{C}$. The mixture was stirred for 3 h at 24 $^\circ\text{C}$, and the solvent was evaporated. The residue was purified by column chromatography on silica gel (hexane/ $\text{CHCl}_3 = 3$) to recover **1c** (19.7 mg, 99%) as a yellow solid.

X-ray analyses

Data collection was conducted with a Rigaku Mercury 70 diffractometer (Mo- $K\alpha$ radiation, $\lambda = 0.71075 \text{ \AA}$). The structure was solved by the direct method (SIR2007) and refined by the full-matrix least-squares method on F^2 with anisotropic temperature factors for non-hydrogen atoms. All the hydrogen atoms were located at the calculated positions and refined with riding.

Crystal data for **1a**

Crystals were obtained by recrystallizing from CHCl_3 /hexane. MF: $\text{C}_{40}\text{H}_{26}$, FW: 506.65, colorless platelet, $0.500 \times 0.400 \times 0.200 \text{ mm}^3$.

At 120 K

Triclinic $P\bar{1}$, $a = 10.902(2) \text{ \AA}$, $b = 15.063(2) \text{ \AA}$, $c = 23.622(3) \text{ \AA}$, $\alpha = 98.955(3)^\circ$, $\beta = 90.783(2)^\circ$, $\gamma = 94.699(2)^\circ$, $V = 3817.7(9) \text{ \AA}^3$, $\rho(Z = 6) = 1.322 \text{ g/cm}^3$. A total of 29,355 reflections ($2\theta_{\text{max}} = 55.0^\circ$) were measured at $T = 120 \text{ K}$. Numerical absorption correction was applied ($\mu = 0.748 \text{ cm}^{-1}$). The final R and $wR2$ values are 0.0488 ($I > 2\sigma I$) and 0.1247 (all data) for 14,838 reflections and 1081 parameters. Estimated standard derivatives are 0.002–0.004 \AA for bond length and 0.11–0.3 $^\circ$ for angles, respectively. CCDC 1586191.

At 160 K

Triclinic $P\bar{1}$, $a = 10.9156(4) \text{ \AA}$, $b = 15.0873(8) \text{ \AA}$, $c = 23.660(2) \text{ \AA}$, $\alpha = 98.975(4)^\circ$, $\beta = 90.724(3)^\circ$, $\gamma = 94.562(3)^\circ$, $V = 3835.4(4) \text{ \AA}^3$, $\rho(Z = 6) = 1.316 \text{ g/cm}^3$. A total of 29,501 reflections ($2\theta_{\text{max}} = 55.0^\circ$) were measured at $T = 160 \text{ K}$. Numerical absorption correction was applied ($\mu = 0.744 \text{ cm}^{-1}$). The final R and $wR2$ values are 0.0485 ($I > 2\sigma I$) and 0.1257 (all data) for 14,920 reflections and 1081 parameters. Estimated standard derivatives are 0.002–0.004 \AA for bond length and 0.11–0.3 $^\circ$ for angles, respectively. CCDC 1586192.

At 200 K

Triclinic $P\bar{1}$, $a = 10.931(2)$ Å, $b = 15.103(3)$ Å, $c = 23.692(5)$ Å, $\alpha = 98.979(4)^\circ$, $\beta = 90.644(3)^\circ$, $\gamma = 94.544(3)^\circ$, $V = 3850(2)$ Å³, $\rho(Z = 6) = 1.311$ g/cm³. A total of 29,608 reflections ($2\theta_{\max} = 55.0^\circ$) were measured at $T = 200$ K. Numerical absorption correction was applied ($\mu = 0.741$ cm⁻¹). The final R and $wR2$ values are 0.0507 ($I > 2\sigma I$) and 0.1322 (all data) for 14,970 reflections and 1081 parameters. Estimated standard derivatives are 0.002–0.004 Å for bond length and 0.11–0.3° for angles, respectively. CCDC 1567390.

At 240 K

Triclinic $P\bar{1}$, $a = 10.949(2)$ Å, $b = 15.115(3)$ Å, $c = 23.719(4)$ Å, $\alpha = 98.957(3)^\circ$, $\beta = 90.541(3)^\circ$, $\gamma = 94.657(2)^\circ$, $V = 3863.7(12)$ Å³, $\rho(Z = 6) = 1.306$ g/cm³. A total of 29,835 reflections ($2\theta_{\max} = 55.0^\circ$) were measured at $T = 240$ K. Numerical absorption correction was applied ($\mu = 0.739$ cm⁻¹). The final R and $wR2$ values are 0.0520 ($I > 2\sigma I$) and 0.1396 (all data) for 15,037 reflections and 1081 parameters. Estimated standard derivatives are 0.002–0.005 Å for bond length and 0.12–0.3° for angles, respectively. CCDC 1567391.

At 280 K

Triclinic $P\bar{1}$, $a = 10.967(3)$ Å, $b = 15.141(4)$ Å, $c = 23.757(5)$ Å, $\alpha = 98.935(5)^\circ$, $\beta = 90.513(5)^\circ$, $\gamma = 94.649(3)^\circ$, $V = 3883(2)$ Å³, $\rho(Z = 6) = 1.311$ g/cm³. A total of 29,928 reflections ($2\theta_{\max} = 55.0^\circ$) were measured at $T = 280$ K. Numerical absorption correction was applied ($\mu = 0.735$ cm⁻¹). The final R and $wR2$ values are 0.0522 ($I > 2\sigma I$) and 0.1423 (all data) for 14,970 reflections and 1081 parameters. Estimated standard derivatives are 0.002–0.005 Å for bond length and 0.11–0.3° for angles, respectively. CCDC 1567392.

At 320 K

Triclinic $P\bar{1}$, $a = 10.976(2)$ Å, $b = 15.158(3)$ Å, $c = 23.792(5)$ Å, $\alpha = 98.983(5)^\circ$, $\beta = 90.449(3)^\circ$, $\gamma = 94.482(3)^\circ$, $V = 3897(2)$ Å³, $\rho(Z = 6) = 1.295$ g/cm³. A total of 29,993 reflections ($2\theta_{\max} = 55.0^\circ$) were measured at $T = 320$ K. Numerical absorption correction was applied ($\mu = 0.732$ cm⁻¹). The final R and $wR2$ values are 0.0544 ($I > 2\sigma I$) and 0.1467 (all data) for 15,175 reflections and 1081 parameters. Estimated standard derivatives are 0.002–0.005 Å for bond length and 0.12–0.3° for angles, respectively. CCDC 1567392.

At 360 K

Triclinic $P\bar{1}$, $a = 10.985(3)$ Å, $b = 15.180(4)$ Å, $c = 23.813(6)$ Å, $\alpha = 98.959(7)^\circ$, $\beta = 90.456(5)^\circ$, $\gamma = 94.475(4)^\circ$, $V = 3910(2)$ Å³, $\rho(Z = 6) = 1.291$ g/cm³. A total of 30,135 reflections ($2\theta_{\max} = 55.0^\circ$) were measured at $T = 360$ K. Numerical absorption correction was applied ($\mu = 0.730$ cm⁻¹). The final R and $wR2$ values are 0.0553 ($I > 2\sigma I$) and 0.1591 (all data) for 15,215 reflections and 1081 parameters. Estimated standard derivatives are 0.003–0.006 Å for bond length and 0.13–0.4° for angles, respectively. CCDC 1567394.

At 400 K

Triclinic $P\bar{1}$, $a = 11.009(3)$ Å, $b = 15.203(4)$ Å, $c = 23.865(6)$ Å, $\alpha = 98.972(6)^\circ$, $\beta = 90.356(5)^\circ$, $\gamma = 94.448(4)^\circ$, $V = 3933(2)$ Å³, $\rho(Z = 6) = 1.283$ g/cm³. A total of 30,269 reflections ($2\theta_{\max} = 55.0^\circ$) were measured at $T = 400$ K. Numerical absorption correction was applied ($\mu = 0.726$ cm⁻¹). The final R and $wR2$ values are 0.0591 ($I > 2\sigma I$) and 0.1620 (all data) for 15,305 reflections and 1081 parameters. Estimated standard derivatives are 0.003–0.006 Å for bond length and 0.13–0.4° for angles, respectively. CCDC 1567395.

Crystal data for **1b**

Crystals were obtained by recrystallizing from CHCl₃/hexane. MF: C₄₂H₂₈, FW: 532.68, colorless block, 0.400 × 0.200 × 0.200 mm³.

At 200 K

Monoclinic $P2_1/c$, $a = 12.782(2)$ Å, $b = 9.228(2)$ Å, $c = 24.084(4)$ Å, $\beta = 100.159(3)^\circ$, $V = 2796.2(8)$ Å³, $\rho(Z = 4) = 1.265$ g/cm³. A total of 20,262 reflections ($2\theta_{\max} = 55.0^\circ$) were measured at $T = 200$ K. Numerical absorption correction was applied ($\mu = 0.715$ cm⁻¹). The final R and $wR2$ values are 0.0633 ($I > 2\sigma I$) and 0.1968 (all data) for 5484 reflections and 379 parameters. Estimated standard derivatives are 0.003–0.006 Å for bond length and 0.14–0.4° for angles, respectively. CCDC 1567396.

At 240 K

Monoclinic $P2_1/c$, $a = 12.789(3)$ Å, $b = 9.229(2)$ Å, $c = 24.088(5)$ Å, $\beta = 100.106(3)^\circ$, $V = 2798.9(11)$ Å³, $\rho(Z = 4) = 1.264$ g/cm³. A total of 20,447 reflections ($2\theta_{\max} = 55.0^\circ$) were measured at $T = 240$ K. Numerical absorption correction was applied ($\mu = 0.714$ cm⁻¹). The final R and $wR2$ values are 0.0711 ($I > 2\sigma I$) and 0.2379 (all data) for 5407 reflections and 379 parameters. Estimated standard derivatives are 0.003–0.008 Å for bond length and 0.15–0.5° for angles, respectively. CCDC 1567397.

At 280 K

Monoclinic $P2_1/c$, $a = 12.791(3)$ Å, $b = 9.230(2)$ Å, $c = 24.091(5)$ Å, $\beta = 100.153(3)^\circ$, $V = 2799.5(11)$ Å³, $\rho(Z = 4) = 1.264$ g/cm³. A total of 20,755 reflections ($2\theta_{\max} = 55.0^\circ$) were measured at $T = 280$ K. Numerical absorption correction was applied ($\mu = 0.714$ cm⁻¹). The final R and $wR2$ values are 0.0684 ($I > 2\sigma I$) and 0.2052 (all data) for 5486 reflections and 379 parameters. Estimated standard derivatives are 0.003–0.007 Å for bond length and 0.14–0.4° for angles, respectively. CCDC 1567398.

At 320 K

Monoclinic $P2_1/c$, $a = 12.780(5)$ Å, $b = 9.232(3)$ Å, $c = 24.074(9)$ Å, $\beta = 100.101(5)^\circ$, $V = 2796(2)$ Å³, $\rho(Z = 4) = 1.265$ g/cm³. A total of 20,388 reflections ($2\theta_{\max} = 55.0^\circ$) were measured at $T = 320$ K. Numerical absorption correction was

applied ($\mu = 0.715 \text{ cm}^{-1}$). The final RI and $wR2$ values are 0.0702 ($I > 2\sigma I$) and 0.2455 (all data) for 5435 reflections and 379 parameters. Estimated standard derivatives are 0.003–0.008 Å for bond length and 0.15–0.5° for angles, respectively. CCDC 1567399.

At 360 K

Monoclinic $P2_1/c$, $a = 12.784(4) \text{ Å}$, $b = 9.232(3) \text{ Å}$, $c = 24.073(8) \text{ Å}$, $\beta = 100.091(5)^\circ$, $V = 2797(2) \text{ Å}^3$, $\rho(Z = 4) = 1.265 \text{ g/cm}^3$. A total of 20,693 reflections ($2\theta_{\text{max}} = 55.0^\circ$) were measured at $T = 360 \text{ K}$. Numerical absorption correction was applied ($\mu = 0.715 \text{ cm}^{-1}$). The final RI and $wR2$ values are 0.0699 ($I > 2\sigma I$) and 0.2074 (all data) for 5486 reflections and 379 parameters. Estimated standard derivatives are 0.003–0.007 Å for bond length and 0.14–0.5° for angles, respectively. CCDC 1567400.

At 400 K

Monoclinic $P2_1/c$, $a = 12.781(5) \text{ Å}$, $b = 9.231(3) \text{ Å}$, $c = 24.071(9) \text{ Å}$, $\beta = 100.096(5)^\circ$, $V = 2796(2) \text{ Å}^3$, $\rho(Z = 4) = 1.265 \text{ g/cm}^3$. A total of 20,734 reflections ($2\theta_{\text{max}} = 55.0^\circ$) were measured at $T = 400 \text{ K}$. Numerical absorption correction was applied ($\mu = 0.715 \text{ cm}^{-1}$). The final RI and $wR2$ values are 0.0700 ($I > 2\sigma I$) and 0.2228 (all data) for 5476 reflections and 379 parameters. Estimated standard derivatives are 0.003–0.008 Å for bond length and 0.15–0.5° for angles, respectively. CCDC 1567401.

Crystal data for 1c

Crystals were obtained by recrystallizing from CHCl_3 /hexane. MF: $\text{C}_{42}\text{H}_{26}$, FW: 530.67.

At 100 K

Orange platelet, $0.500 \times 0.200 \times 0.100 \text{ mm}^3$, orthorhombic $Pbca$, $a = 17.960(3) \text{ Å}$, $b = 15.813(3) \text{ Å}$, $c = 18.523(4) \text{ Å}$, $V = 5261(2) \text{ Å}^3$, $\rho(Z = 8) = 1.340 \text{ g/cm}^3$. A total of 37,745 reflections ($2\theta_{\text{max}} = 55.0^\circ$) were measured at $T = 100 \text{ K}$. Numerical absorption correction was applied ($\mu = 0.758 \text{ cm}^{-1}$). The final RI and $wR2$ values are 0.0419 ($I > 2\sigma I$) and 0.1033 (all data) for 5162 reflections and 379 parameters. Estimated standard derivatives are 0.0018–0.003 Å for bond length and 0.10–0.15° for angles, respectively. CCDC 1586193.

At 120 K

Orange platelet, $0.500 \times 0.200 \times 0.100 \text{ mm}^3$, orthorhombic $Pbca$, $a = 17.960(3) \text{ Å}$, $b = 15.820(3) \text{ Å}$, $c = 18.509(3) \text{ Å}$, $V = 5259(2) \text{ Å}^3$, $\rho(Z = 8) = 1.340 \text{ g/cm}^3$. A total of 37,892 reflections ($2\theta_{\text{max}} = 55.0^\circ$) were measured at $T = 120 \text{ K}$. Numerical absorption correction was applied ($\mu = 0.759 \text{ cm}^{-1}$). The final RI and $wR2$ values are 0.0395 ($I > 2\sigma I$) and 0.0986 (all data) for 5158 reflections and 379 parameters. Estimated standard derivatives are 0.0016–0.002 Å for bond length and 0.09–0.13° for angles, respectively. CCDC 1586194.

At 160 K

Orange platelet, $0.500 \times 0.200 \times 0.100 \text{ mm}^3$, orthorhombic *Pbca*, $a = 17.977(3) \text{ \AA}$, $b = 15.846(3) \text{ \AA}$, $c = 18.532(3) \text{ \AA}$, $V = 5279(2) \text{ \AA}^3$, $\rho(Z = 8) = 1.335 \text{ g/cm}^3$. A total of 18,440 reflections ($2\theta_{\text{max}} = 55.0^\circ$) were measured at $T = 160 \text{ K}$. Numerical absorption correction was applied ($\mu = 0.756 \text{ cm}^{-1}$). The final *R**I* and *wR**2* values are 0.0415 ($I > 2\sigma I$) and 0.1046 (all data) for 5162 reflections and 379 parameters. Estimated standard derivatives are 0.0018–0.003 \AA for bond length and 0.10–0.15° for angles, respectively. CCDC 1586195.

At 200 K

Orange platelet, $0.500 \times 0.200 \times 0.100 \text{ mm}^3$, orthorhombic *Pbca*, $a = 17.983(3) \text{ \AA}$, $b = 15.870(3) \text{ \AA}$, $c = 18.550(3) \text{ \AA}$, $V = 5294(2) \text{ \AA}^3$, $\rho(Z = 8) = 1.332 \text{ g/cm}^3$. A total of 38,119 reflections ($2\theta_{\text{max}} = 55.0^\circ$) were measured at $T = 200 \text{ K}$. Numerical absorption correction was applied ($\mu = 0.754 \text{ cm}^{-1}$). The final *R**I* and *wR**2* values are 0.0415 ($I > 2\sigma I$) and 0.1032 (all data) for 5190 reflections and 379 parameters. Estimated standard derivatives are 0.0016–0.003 \AA for bond length and 0.09–0.15° for angles, respectively. CCDC 1567402.

At 240 K

Orange platelet, $0.500 \times 0.200 \times 0.100 \text{ mm}^3$, orthorhombic *Pbca*, $a = 18.005(3) \text{ \AA}$, $b = 15.899(3) \text{ \AA}$, $c = 18.579(3) \text{ \AA}$, $V = 5318(2) \text{ \AA}^3$, $\rho(Z = 8) = 1.325 \text{ g/cm}^3$. A total of 18,695 reflections ($2\theta_{\text{max}} = 55.0^\circ$) were measured at $T = 240 \text{ K}$. Numerical absorption correction was applied ($\mu = 0.750 \text{ cm}^{-1}$). The final *R**I* and *wR**2* values are 0.0429 ($I > 2\sigma I$) and 0.1092 (all data) for 5194 reflections and 379 parameters. Estimated standard derivatives are 0.0018–0.003 \AA for bond length and 0.10–0.16° for angles, respectively. CCDC 1567403.

At 280 K

Orange platelet, $0.500 \times 0.200 \times 0.100 \text{ mm}^3$, orthorhombic *Pbca*, $a = 18.030(3) \text{ \AA}$, $b = 15.931(3) \text{ \AA}$, $c = 18.613(3) \text{ \AA}$, $V = 5346(2) \text{ \AA}^3$, $\rho(Z = 8) = 1.318 \text{ g/cm}^3$. A total of 19,536 reflections ($2\theta_{\text{max}} = 55.0^\circ$) were measured at $T = 280 \text{ K}$. Numerical absorption correction was applied ($\mu = 0.746 \text{ cm}^{-1}$). The final *R**I* and *wR**2* values are 0.0445 ($I > 2\sigma I$) and 0.1146 (all data) for 5217 reflections and 379 parameters. Estimated standard derivatives are 0.0019–0.003 \AA for bond length and 0.10–0.17° for angles, respectively. CCDC 1567404.

At 320 K

Orange platelet, $0.500 \times 0.200 \times 0.100 \text{ mm}^3$, orthorhombic *Pbca*, $a = 18.0425(8) \text{ \AA}$, $b = 15.9563(6) \text{ \AA}$, $c = 18.6292(8) \text{ \AA}$, $V = 5346.2(4) \text{ \AA}^3$, $\rho(Z = 8) = 1.314 \text{ g/cm}^3$. A total of 22,457 reflections ($2\theta_{\text{max}} = 55.0^\circ$) were measured at $T = 320 \text{ K}$. Numerical absorption correction was applied ($\mu = 0.744 \text{ cm}^{-1}$). The final *R**I* and *wR**2* values are 0.0457 ($I > 2\sigma I$) and 0.1150 (all data) for 5241 reflections and 379 parameters. Estimated standard derivatives are 0.0019–0.003 \AA for bond length and 0.10–0.18° for angles, respectively. CCDC 1567405.

At 360 K

Orange platelet, $0.500 \times 0.200 \times 0.100 \text{ mm}^3$, orthorhombic *Pbca*, $a = 18.054(3) \text{ \AA}$, $b = 15.970(3) \text{ \AA}$, $c = 18.644(3) \text{ \AA}$, $V = 5375(2) \text{ \AA}^3$, $\rho(Z = 8) = 1.311 \text{ g/cm}^3$. A total of 23,249 reflections ($2\theta_{\text{max}} = 55.0^\circ$) were measured at $T = 360 \text{ K}$. Numerical absorption correction was applied ($\mu = 0.742 \text{ cm}^{-1}$). The final *R* and *wR* values are 0.0465 ($I > 2\sigma I$) and 0.1179 (all data) for 5251 reflections and 379 parameters. Estimated standard derivatives are 0.0019–0.003 \AA for bond length and 0.11–0.19° for angles, respectively. CCDC 1567406.

At 400 K

Red platelet, $0.500 \times 0.200 \times 0.100 \text{ mm}^3$, orthorhombic *Pbca*, $a = 18.076(3) \text{ \AA}$, $b = 15.999(3) \text{ \AA}$, $c = 18.676(4) \text{ \AA}$, $V = 5401(2) \text{ \AA}^3$, $\rho(Z = 8) = 1.305 \text{ g/cm}^3$. A total of 22,281 reflections ($2\theta_{\text{max}} = 55.0^\circ$) were measured at $T = 400 \text{ K}$. Numerical absorption correction was applied ($\mu = 0.739 \text{ cm}^{-1}$). The final *R* and *wR* values are 0.0500 ($I > 2\sigma I$) and 0.1245 (all data) for 5280 reflections and 379 parameters. Estimated standard derivatives are 0.002–0.004 \AA for bond length and 0.11–0.2° for angles, respectively. CCDC 1567407.

References

1. T. Suzuki, Y. Uchimura, Y. Ishigaki, T. Takeda, R. Katoono, H. Kawai, K. Fujiwara, A. Nagaki, J. Yoshida, *Chem. Lett.* **41**, 541–543 (2012)
2. T. Takeda, H. Kawai, R. Herges, E. Mucke, Y. Sawai, K. Murakoshi, K. Fujiwara, T. Suzuki, *Tetrahedron Lett.* **50**, 3693–3697 (2009)
3. A.A. Zavitsas, *J. Phys. Chem. A* **107**, 897–898 (2003)
4. D. Cho, Y. Ikabata, T. Yoshikawa, Y.L. Jin, H. Nakai, *Bull. Chem. Soc. Jpn.* **88**, 1636–1641 (2015)
5. T.R. Battersby, R. VernonClark, J.S. Siegel, *J. Am. Chem. Soc.* **119**, 7048–7054 (1997)
6. K.K. Baldrige, Y. Kasahara, K. Ogawa, J.S. Siegel, K. Tanaka, F. Toda, *J. Am. Chem. Soc.* **120**, 6167–6168 (1998)
7. B. Kahr, C.A. Mitchell, J.M. Chance, R.V. Clark, P. Gantzel, K.K. Baldrige, J.S. Siegel, *J. Am. Chem. Soc.* **117**, 4479–4482 (1995)
8. J.L. Adcock, A.A. Gakh, J.L. Pollitte, C. Woods, *J. Am. Chem. Soc.* **114**, 3980–3981 (1992)
9. Y. Uchimura, T. Shimajiri, Y. Ishigaki, R. Katoono, T. Suzuki, *Chem. Commun.* **54**, 10300–10303 (2018)
10. E.R. Johnson, S. Keinan, P. Mori-Sánchez, J. Contreras-García, A.J. Cohen, W. Yang, *J. Am. Chem. Soc.* **132**, 6498–6506 (2010)
11. Y. Uchimura, T. Takeda, R. Katoono, K. Fujiwara, T. Suzuki, *Angew. Chem. Int. Ed.* **54**, 4010–4013 (2015)
12. T. Suzuki, J. Nishida, M. Ohkita, T. Tsuji, *Angew. Chem. Int. Ed.* **39**, 1804–1806 (2000)
13. H. Kawai, T. Takeda, K. Fujiwara, M. Wakeshima, Y. Hinatsu, T. Suzuki, *Chem.—A Eur. J.* **14**, 5780–5793 (2008)
14. T. Saitoh, S. Yoshida, J. Ichikawa, *Org. Lett.* **6**, 4563–4565 (2004)
15. M.W. Wong, *Chem. Phys. Lett.* **256**, 391–399 (1996)
16. K. Van Helvoort, W. Knippers, R. Fantoni, S. Stolte, *Chem. Phys.* **111**, 445–465 (1987)
17. S. Kammermeier, R. Herges, P.G. Jones, *Angew. Chem. Int. Ed. Engl.* **36**, 1757–1760 (1997)
18. R.C. Haddon, *J. Am. Chem. Soc.* **109**, 1676–1685 (1987)

19. R.C. Haddon, *J. Phys. Chem. A* **105**, 4164–4165 (2001)
20. W.H.E. Schwarz, K. Ruedenberg, L. Mensching, *J. Am. Chem. Soc.* **111**, 6926–6933 (1989)
21. L. Mensching, W. Von Niessen, P. Valtazanos, K. Ruedenberg, W.H.E. Schwarz, *J. Am. Chem. Soc.* **111**, 6933–6941 (1989)
22. T. Nishiuchi, S. Uno, Y. Hirao, T. Kubo, *J. Org. Chem.* **81**, 2106–2112 (2016)
23. R.F.W. Bader, *Acc. Chem. Res.* **18**, 9–15 (1985)
24. A.D. Becke, K.E. Edgecombe, *J. Chem. Phys.* **92**, 5397–5403 (1990)
25. S. Hayashi, K. Matsuiwa, M. Kitamoto, W. Nakanishi, *J. Phys. Chem. A* **117**, 1804–1816 (2013)
26. M.J. Frisch, G.W. Trucks, H.B. Schlegel, G.E. Scuseria, M.A. Robb, J.R. Cheeseman, G. Scalmani, V. Barone, B. Mennucci, G.A. Petersson, H. Nakatsuji, M. Caricato, X. Li, H.P. Hratchian, A.F. Izmaylov, J. Bloino, G. Zheng, J.L. Sonnenberg, M. Hada, M. Ehara, K. Toyota, R. Fukuda, J. Hasegawa, M. Ishida, T. Nakajima, Y. Honda, O. Kitao, H. Nakai, T. Vreven, J.A. Montgomery, J.E. Peralta, F. Ogliaro, M. Bearpark, J.J. Heyd, E. Brothers, K.N. Kudin, V.N. Staroverov, R. Kobayashi, J. Normand, K. Raghavachari, A. Rendell, J.C. Burant, S.S. Iyengar, J. Tomasi, M. Cossi, N. Rega, J.M. Millam, M. Klene, J.E. Knox, J.B. Cross, V. Bakken, C. Adamo, J. Jaramillo, R. Gomperts, R.E. Stratmann, O. Yazyev, A.J. Austin, R. Cammi, C. Pomelli, J.W. Ochterski, R.L. Martin, K. Morokuma, V.G. Zakrzewski, G.A. Voth, P. Salvador, J.J. Dannenberg, S. Dapprich, A.D. Daniels, Ö. Farkas, J.B. Foresman, J.V. Ortiz, J. Cioslowski, D.J. Fox, Gaussian, Inc., Wallingford, CT (2013)
27. J.M. Frisch, W.G. Trucks, B.H. Schlegel, E.G. Scuseria, A.M. Robb, R.J. Cheeseman, G. Scalmani, V. Barone, A. G. Petersson, H. Nakatsuji, X. Li, M. Caricato, V.A. Marenich, J. Bloino, G.B. Janesko, R. Gomperts, B. Mennucci, P.H. Hratchian, V. J. Ortiz, F.A. Izmaylov, L.J. Sonnenberg, D. Williams-Young, F. Ding, F. Lipparini, F. Egidi, J. Goings, B. Peng, A. Petrone, T. Henderson, D. Ranasinghe, G.V. Zakrzewski, J. Gao, N. Rega, G. Zheng, W. Liang, M. Hada, M. Ehara, K. Toyota, R. Fukuda, J. Hasegawa, M. Ishida, T. Nakajima, Y. Honda, O. Kitao, H. Nakai, T. Vreven, K. Throssell, A.J. Montgomery, Jr., E.J. Peralta, F. Ogliaro, J.M. Bearpark, J.J. Heyd, N.E. Brothers, N.K. Kudin, N.V. Staroverov, A.T. Keith, R. Kobayashi, J. Normand, K. Raghavachari, P.A. Rendell, C.J. Burant, S.S. Iyengar, J. Tomasi, M. Cossi, M.J. Millam, M. Klene, C. Adamo, R. Cammi, W.J. Ochterski, L.R. Martin, K. Morokuma, O. Farkas, B.J. Foresman, J.D. Fox, Gaussian, Inc., Wallingford, CT (2019)
28. T. Lu, F. Chen, *J. Comput. Chem.* **33**, 580–592 (2012)
29. E.D. Glendening, J.K. Badenhoop, A.E. Reed, J.E. Carpenter, J.A. Bohmann, C.M. Morales, P. Karafiloglou, C.R. Landis, F. Weinhold, Theoretical Chemistry Institute, University of Wis (2018)
30. J.M. McBride, *Tetrahedron* **30**, 2009–2022 (1974)
31. L.M. Diamond, F.R. Knight, K.S. Athukorala Arachchige, R.A.M. Randall, M. Bühl, A.M.Z. Slawin, J.D. Woollins, *Eur. J. Inorg. Chem.* 1512–1523 (2014)

Chapter 3

Discovery of Flexible Bonds Based on an Extremely Elongated C–C Single Bond



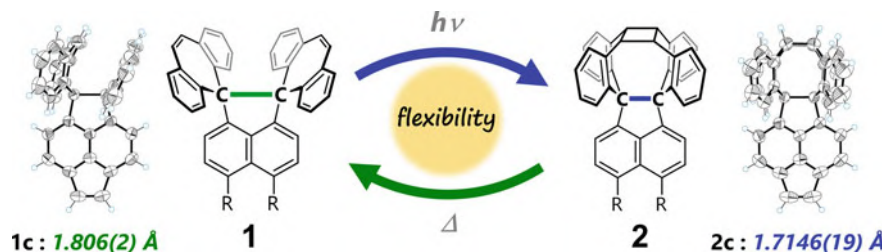
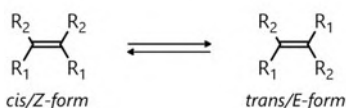
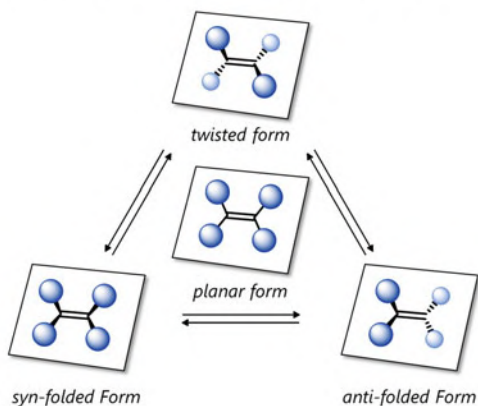
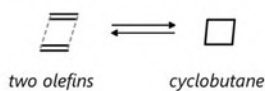
3.1 Introduction

Strained molecules such as sterically congested polycyclic aromatic hydrocarbons [1–8] as well as cyclic π -conjugated compounds [9–15] often exhibit unusual parameters, and thus have attracted much attention due to their potential applications. Chapter 2 demonstrated that spiro-DBCHT **1a–1c** has an unusual C–C single bond beyond 1.8 Å based on the core–shell strategy [16]. The author envisaged that such a “hyper covalent bond” could be weak enough to exhibit reversible expansion, contraction, formation, and scission, which could be visualized by X-ray analyses (Scheme 3.1).

C=C double bonds are known to show stimuli-responsive isomerization such as geometrical isomerization, conformational/configurational isomerization, and valence isomerization (Scheme 3.2), which have been used for the development of functional materials and molecular machines, since such isomerization changes not only the molecular structure but also its physical properties.

In this research, the author focuses on the DBCHT unit, which has been used to construct photoresponsive molecules based on overcrowded ethylenes through *syn/anti* configurational isomerization [17, 18]. Another aspect is a structurally fixed *cis*-stilbene moiety in the DBCHT unit, and thus the intramolecular [2 + 2] cycloaddition reaction could proceed as in DBCHT-dimer to produce a caged molecule based on a pericyclic reaction (Fig. 3.1) [19].

The latter reactivity is more interesting from a topochemical point of view, since the solid-state reaction would be applicable for stimuli-responsive systems toward potential applications such as photoswitching, optical recording, and sensing materials [20–28]. By controlling the crystal packing structure, intermolecular [2 + 2] cyclization could proceed in a single-crystal-to-single-crystal (SCSC) manner upon photoirradiation, which has been realized by the aid of soft matter/lattices such as ionic crystals, metal–organic frameworks, and coordination polymers [29–34]. Furthermore, only a few examples exhibit reversible SCSC thermal cleavage of the

Scheme 3.1 Interconversion between spiro-DBCHT **1** and caged molecule **2****a. Geometrical isomer****b. Conformational/configurational isomer****c. Valence isomer**

Scheme 3.2 Isomerization processes of C=C double bond

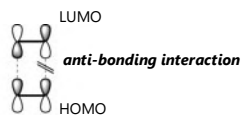
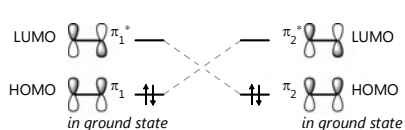
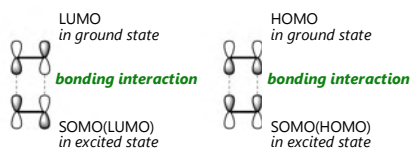
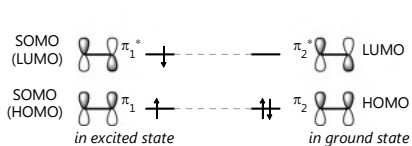
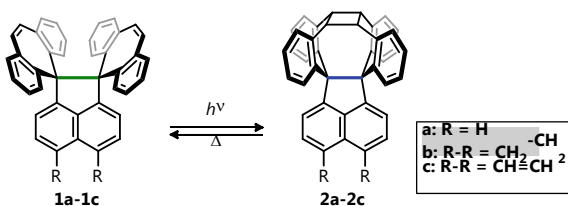
a. Thermal reaction (symmetry forbidden)**b. Photoreaction (photochemically allowed)**

Fig. 3.1 Frontier orbital interaction of [2 + 2] cycloaddition reaction between C=C double bonds

Scheme 3.3 Structural change between spiro-DBCHT **1** and caged molecules **2**



cyclobutane ring resulting from the SCSC photocycloaddition of two C=C bonds [30–32], and none of them are pure neutral organic molecules.

Since *cis*-stilbene moieties connected by an elongated C–C bond face to each other in the outer “shell”-structure of spiro-DBCHT **1a–1c**, as described in Chap. 2, the author expects that a reversible SCSC [2 + 2] photocycloaddition and thermal cycloreversion could proceed in the pure hydrocarbon crystal (Scheme 3.3). Once a [2 + 2] photocycloaddition reaction occurs for the spiro-DBCHT **1a–1c**, changes not only in “shell” structures and physical properties but also in the bond length of the “core” C–C bond should be observed. This chapter describes how the reversible formation and scission of C–C bonds in a single crystal can be induced by external stimulation of light and heat, accompanied by reversible expansion and contraction of the elongated Csp^3 – Csp^3 bond and by a change of the HOMO level by ca. 1 eV.

3.2 Results and Discussions

3.2.1 Intramolecular Photocyclization

According to the X-ray structures of **1a–1c** [16], two DBCHT units are well-overlapped due to π – π interaction with a C–C distance of 3.163(3)–3.357(4) Å between the vinylic carbons. Thus, the author first photoirradiated $CHCl_3$ solutions of **1a–1c** at around 365 nm, which is assigned to an absorption band of DBCHT units by time-dependent density functional theory (TD-DFT) calculations (Fig. 3.2). As a result, [2 + 2] photocyclization proceeded quantitatively in all spiro-DBCHT **1a–1c** to produce caged molecules **2a–2c** with a cyclobutene ring, which was monitored by UV/Vis and NMR spectroscopies (Fig. 3.3). Cleavage of the cyclobutane ring in **2a–2c** did not occur upon photoirradiation at any wavelength. Disappearance of *cis*-stilbene moieties results not only in a blue-shift and hypochromic shift of the absorption band, but also in switching of the major chromophores to the acenaphthene ring which is located far from the cyclobutane ring (Fig. 3.2).

Photocyclization reaction proceeded in preparative scale to produce **2** from **1** in $CHCl_3$ quantitatively (Scheme 3.4). As expected, photoirradiation by using a LED lamp (375 nm) of a solid-state sample of **1a–1c** also underwent photocycloaddition reaction to **2a–2c** quantitatively. Caged molecule **2a–2c** gave high-quality single

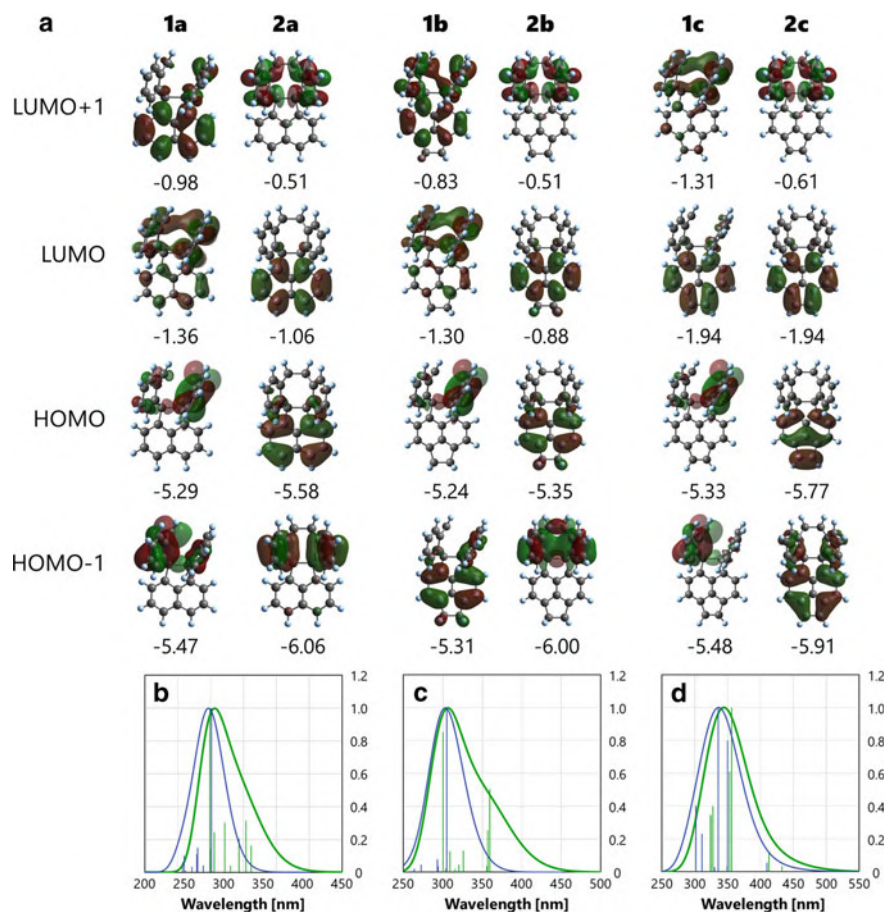


Fig. 3.2 (a) Theoretically obtained Kohn–Sham orbitals (MOs) of the optimized structures by DFT calculations (B3LYP/6-31G*) for **1a–1c** and **2a–2c**. The values of energy level [eV] are shown under the profile of molecular orbitals. Simulated absorption spectra by TD-DFT calculations (B3LYP/6-31G*) of (b) **1a** and **2a**, (c) **1b** and **2b** and (d) **1c** and **2c**; green and blue lines correspond to **1a–1c** and **2a–2c**, respectively

crystals suitable for X-ray diffraction measurement. X-ray analyses revealed that **2a–2c** adopt caged structures with a four-membered ring (Scheme 3.4). A remarkable point is that contraction of the central C–C single bond by as much as about 5%, from 1.720(2)–1.742(2), 1.773(3), and 1.7980(18) Å for spiro-DBCHT **1a**, **1b**, and **1c** to 1.676(6)–1.678(6), 1.7133(16), and 1.7129(19) Å for caged molecules **2a**, **2b**, and **2c**, respectively, was observed at 200 K (Table 3.1).

To verify the bonding nature of the contracted C–C single bond, the author investigated the stretching vibration of caged molecules **2a–2c** by Raman spectroscopy with single crystals at 298 K to attain direct information of the bond strength. Observed Raman shifts corresponding to the central C–C bond were 653, 646, and 648 cm^{-1}

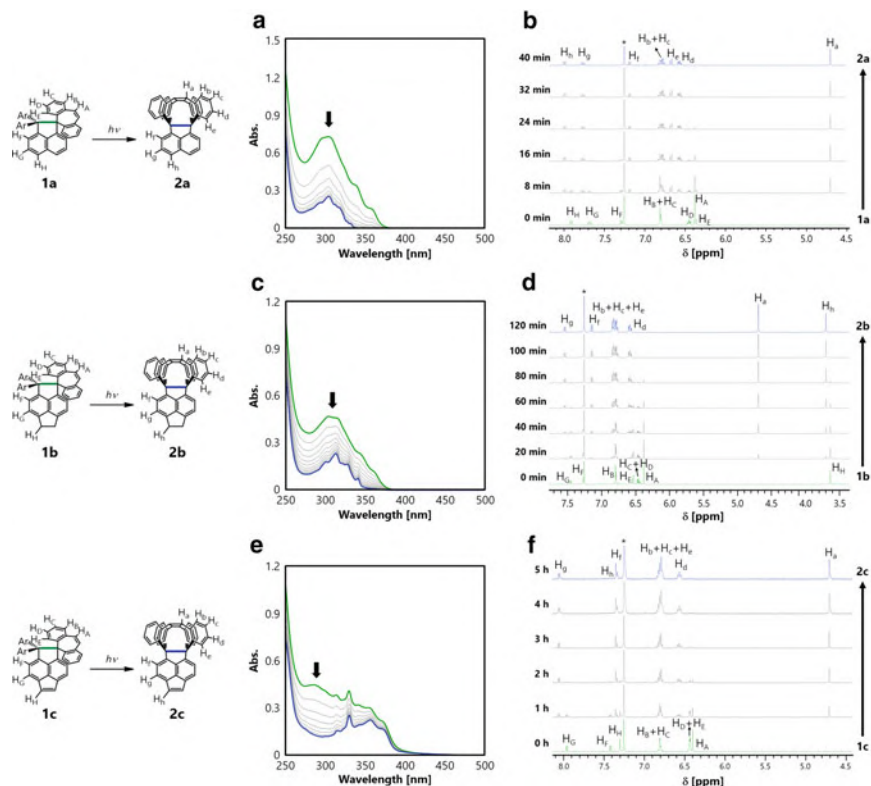
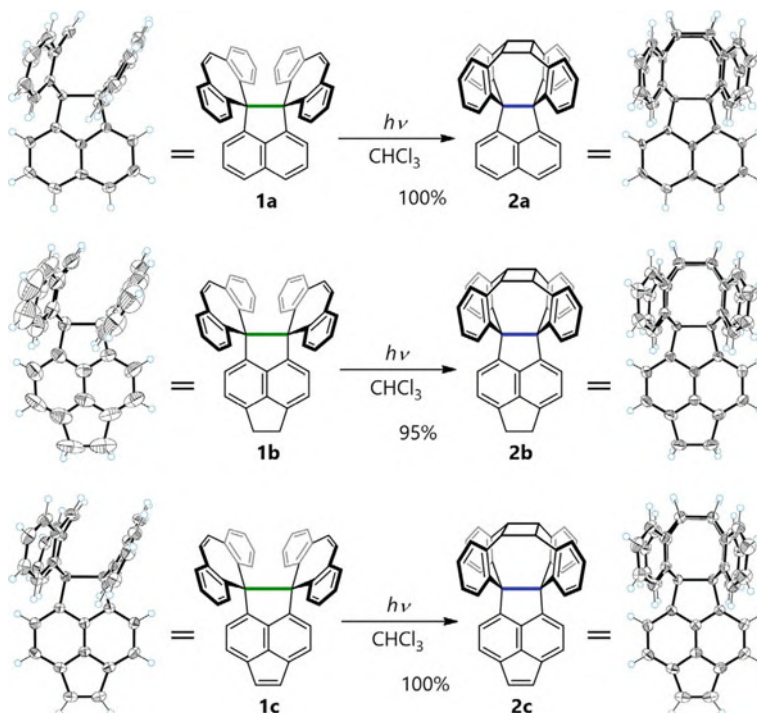


Fig. 3.3 Changes in the UV/Vis spectrum of **1** (green) to **2** (blue) in CHCl_3 (**a**; **1a** to **2a**, **c**; **1b** to **2b**, **e**; **1c** to **2c**) and in the ^1H NMR spectrum of **1** (green) to **2** (blue) in CDCl_3 upon photoirradiation at 365 nm (monochromated light from 150 W Xe lamp, slit width: 10 nm, **b**; **1a** to **2a**, **d**; **1b** to **2b**, **f**; **1c** to **2c**). The residual proton signal of the solvent (CHCl_3 , $\delta = 7.26$ ppm) is marked with an asterisk

for **2a**, **2b**, and **2c**, respectively, which are consistent with the simulated values (663 , 653 , and 658 cm^{-1} without scaling and 637 , 627 and 633 cm^{-1} with a factor [35] of 0.9613 at B3LYP/6-31G). These experimental values of **2a–2c** are approximately 11% greater than those for **1a–1c** (Table 3.1 and Fig. 3.4). The estimated force constant (173.9 N m^{-1}) obtained as a second derivative of the bond length by DFT calculations (M06-2X/6-31G*) for **2c** is 1.6 times as large as that for **1c** (108.3 N m^{-1}) (Fig. 3.5).

While thermal isomerization of caged molecules **2a–2c** did not proceed in solution, long-bonded **1a–1c** were quantitatively regenerated by heating of caged molecules **2a–2c** in a solid state (Scheme 3.5, Fig. 3.6). Although the reason is still unclear, the author supposes that thermal energy by heating was used not for cycloreversion reaction but for some kinds of molecular motion in solution of **2**, and/or caged



Scheme 3.4 Photoirradiation of **1a–1c** with a 375 nm light-emitting diode (yields are for the isolated product), and ORTEP drawings at 200 K of **1a–1c** and **2a–2c**

molecules **2** may be thermodynamically more stable than spiro-DBCHT **1** in the solution state, since the predicted energy levels of **1** and **2** in a gaseous state are very close (vide infra).

3.2.2 Theoretical Study

DFT calculations (B3LYP/6-31G*) were performed to obtain the energy level of each molecule (Scheme 3.6). The predicted energy levels of **1c** and **2c** in a gaseous state are almost the same. Although another reaction pathway (path B) could be considered for cleavage of the cyclobutene ring, the potential isomer has a much higher energy than **1c** and **2c**. Thus, such an isomer with eight-membered rings is not a reasonable product of a thermal reaction and was not observed by the thermal isomerization reaction of **2c** in either the solid state or solution. In addition, NBO and AIM analyses indicated that bond contraction from spiro-DBCHT **1** to caged molecules **2** induces a slight enhancement of the values of *s*-character for **2c**, which are estimated to be 21.05 and 20.83 by using the atomic coordinates of the X-ray

Table 3.1 Central C–C bond lengths and Raman shifts for **1a–1c** and **2a–2c** determined by X-ray analysis (at 200 K) and Raman spectroscopy (at 298 K) with single crystals. Theoretically obtained values are based on DFT calculations at the B3LYP/6-31G* level

| | 1a | 2a | 1b | 2b | 1c | 2c |
|----------------------------------|-----------|-------------------|-------------------|-----------|------------|------------|
| C–C bond length [\AA] | Expt. | 1.720(2)–1.742(2) | 1.676(6)–1.678(6) | 1.773(3) | 1.7133(16) | 1.7980(18) |
| | Calcd. | 1.769 | 1.698 | 1.826 | 1.734 | 1.835 |
| Raman shift [cm^{-1}] | Expt. | 650 | 653 | 582 | 646 | 587 |
| | Calcd. | 657 | 663 | 631 | 653 | 635 |

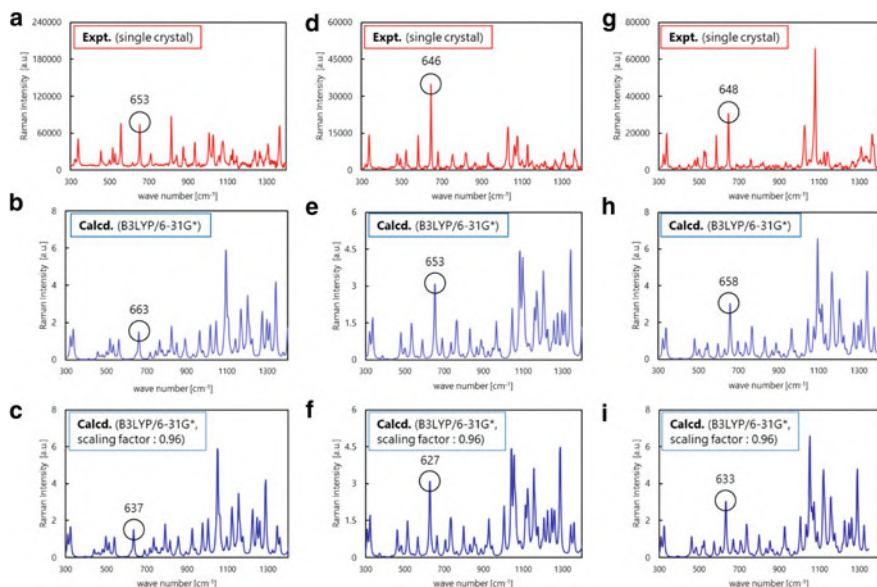


Fig. 3.4 Raman spectra (red) measured by using a single crystal for (a) **1a**, (d) **1b**, and (g) **1c** at 298 K. Simulated spectra predicted by DFT calculations at B3LYP/6-31G* level without scaling (light blue) for (b) **1a**, (e) **1b** and (h) **1c**, at B3LYP/6-31G* level under scaling (blue) for (c) **1a**, (f) **1b** and (i) **1c**

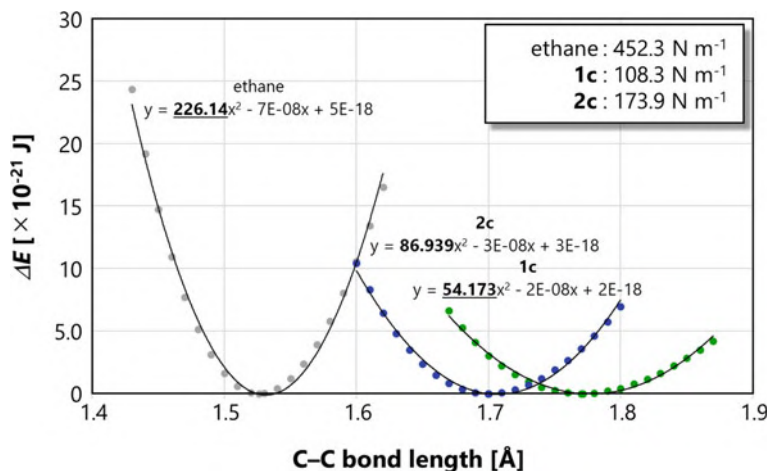
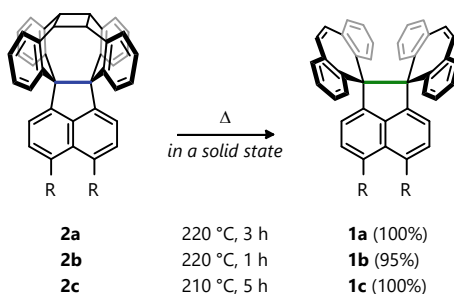


Fig. 3.5 Potential curves for ethane (gray dots) **1c** (green dots) and **2c** (blue dots) calculated by varying the central C–C bond length in steps of 0.01 Å and by considering the most stable conformation (M06-2X/6-31G*)

Scheme 3.5 Thermal isomerization of **2a–2c** in a solid state



crystal structure obtained at 200 K, while those for **1c** are calculated to be 19.16 and 18.64 (Table 3.2).

3.2.3 Single-Crystal-to-Single-Crystal Transformation

By considering the similarity of the crystal packing and lattice parameters of **1b** and **2b**, the author envisaged that both the photocyclization of **1b** and the thermal cycloreversion of **2b** would proceed in a single-crystalline state. When a single crystal of **1b** was photoirradiated at its absorption end ($\lambda > 390$ nm) so that the light can be penetrated into the deep inside of the crystal for 10 h, caged molecule **2b** was generated with maintaining single-crystallinity, and the proportion of **2b** was as high as 45% as determined by a single-crystal X-ray analysis at 200 K by using disorder analysis. This transformation is accompanied by contraction of the central C–C bond from 1.773(3) to 1.738(3) Å (Fig. 3.7a, c). After photoirradiation of **1b** for 60 h, valence isomerization to **2b** was completed while maintaining single-crystallinity, where the contracted bond length [1.7118(15) Å] is essentially the same as that [1.7133(16) Å] in the recrystallized sample of **2b**.

In addition, upon heating of a single crystal of **2b** at 493 K for 10 min, thermal cleavage of the cyclobutane ring proceeded in 18% yield, and thermal isomerization proceeded completely after heating for 60 min, which was followed by single-crystal X-ray diffraction at 300 K (Fig. 3.7b, d). The reason for the difference temperature of X-ray analyses is related to the fact that **1b** undergoes a phase transition of the crystal at lower temperature. As a result of the ring opening of cyclobutane, the central C–C bond was certainly expanded to the original value [1.777(3) Å], which is in good agreement with that [1.772(3) Å] in the recrystallized sample of **1b**, thanks to the outstanding stability of the long-bonded compound **1b** at high temperature. These results show that reversible SCSC transformation occurred between **1b** and **2b**, accompanied by unprecedented expansion and contraction of the elongated C–C bond. Although single-crystallinity was not maintained for the pairs **1a/2a** and **1c/2c**, quantitative [2 + 2] photocyclization and thermal cleavage of the cyclobutane ring were also achieved in the solid state.

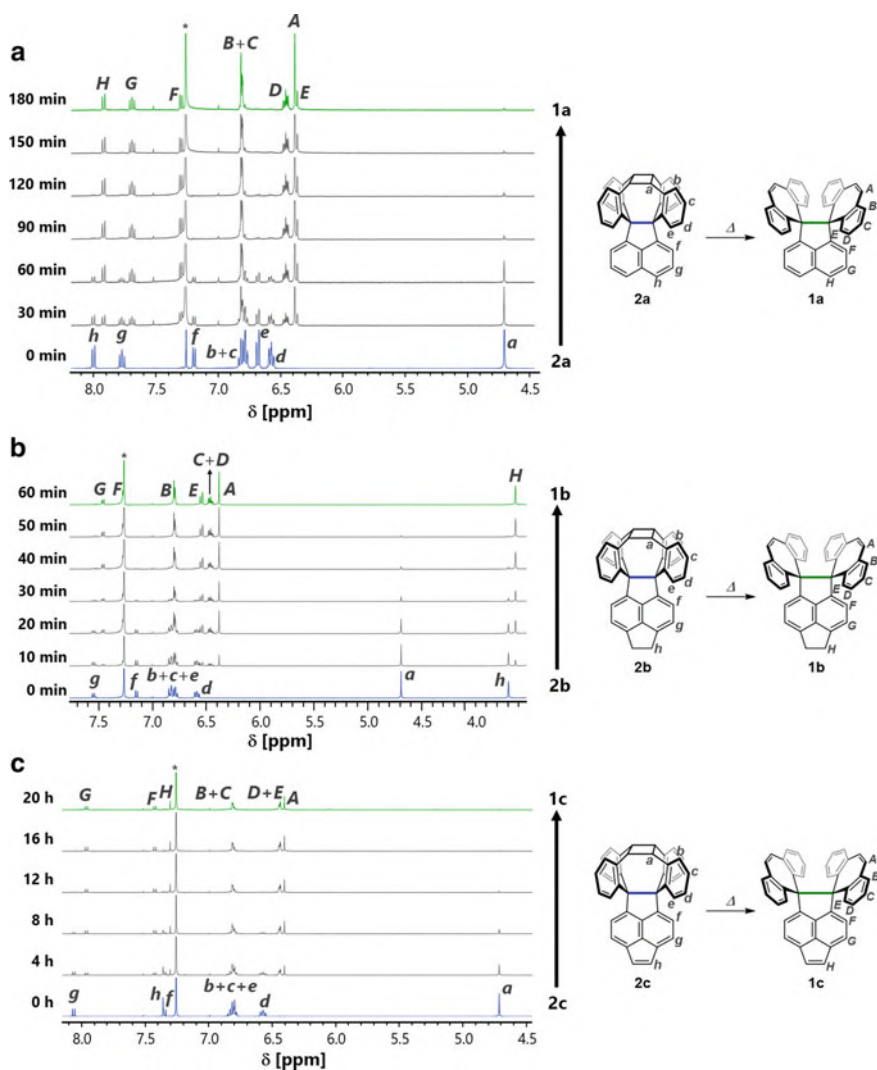


Fig. 3.6 Thermal isomerization was monitored by ^1H NMR spectroscopy in CDCl_3 for (a) **2a**, (b) **2b**, and (c) **2c** upon heating at 493 K, 493 K, and 473 K, respectively, in a solid state. The residual proton signal of the solvent (CHCl_3 , $\delta = 7.26$ ppm) is marked with an asterisk

3.2.4 Redox Behavior

To date, dynamic redox (*dyrex*) systems have been studied based on an HPE skeleton [36, 37], in which neutral electron donors and corresponding dications can be interconvertible upon two-electron transfer. During their interconversion, they show a reversible change in structure such as C–C bond formation/cleavage, accompanied



Scheme 3.6 The optimized structures and relative energies of each state related to thermal isomerization of **2c** predicted by DFT calculations (B3LYP/6-31G*)

Table 3.2 (A) NBO and (B) AIM parameters for C1–C2 bond in **1a–1c** and **2a–2c** at the B3LYP-D3/6-311+G**₂. Atomic coordinates of crystal structures for **1a–1c** and **2a–2c** were used for calculations. Since the single crystals of **2a** were obtained as solvate with hexane molecules, X-ray analysis at 400 K was not performed

| A | 200 K | | | 400 K | | | 200 K | | | 400 K | | | | |
|---|---------------------|----------|------------|----------|----------|----------|----------|------------|------------|--------|----------|------------|--------|--------|
| | 1a | 1b | 1c | 1a | 1b | 1c | 2a | 2b | 2c | 2a | 2b | 2c | | |
| Bond length [Å] | 1.742(2) | 1.773(3) | 1.7980(18) | 1.746(3) | 1.771(3) | 1.806(2) | 1.678(6) | 1.7133(16) | 1.7129(19) | | 1.722(2) | 1.7146(19) | | |
| Occupancy | 1.919 | 1.912 | 1.910 | 1.919 | 1.912 | 1.908 | 1.929 | 1.923 | 1.923 | | 1.922 | 1.927 | | |
| WBI | 0.8604 | 0.8416 | 0.8345 | 0.8594 | 0.8427 | 0.8302 | 0.8858 | 0.8799 | 0.8775 | | 0.8761 | 0.8787 | | |
| <i>s</i> -character [%] | C1 | | | 20.40 | 19.47 | 19.16 | 20.36 | 19.55 | 18.83 | 22.24 | 21.10 | 21.05 | 20.84 | 20.83 |
| | C2 | | | 20.05 | 19.15 | 18.64 | 19.92 | 19.22 | 18.43 | 21.24 | 21.02 | 20.83 | 20.74 | 21.14 |
| NBO-energy [eV] | bonding | | | -11.65 | -11.16 | -11.12 | -11.59 | -11.65 | -11.01 | -12.38 | -11.88 | -12.04 | -11.78 | -12.04 |
| | <i>anti-bonding</i> | | | 5.551 | 5.491 | 4.922 | 5.852 | 5.551 | 4.816 | 7.129 | 6.621 | 6.447 | 6.453 | 6.405 |
| B | 200 K | | | 400 K | | | 200 K | | | 400 K | | | | |
| | 1a | 1b | 1c | 1a | 1b | 1c | 2a | 2b | 2c | 2a | 2b | 2c | | |
| Bond length [Å] | 1.742(2) | 1.773(3) | 1.7980(18) | 1.746(3) | 1.771(3) | 1.806(2) | 1.678(6) | 1.7133(16) | 1.7129(19) | | 1.722(2) | 1.7146(19) | | |
| Density of all electrons : ρ_b | 0.1629 | 0.1538 | 0.1469 | 0.1616 | 0.1544 | 0.1444 | 0.1833 | 0.1721 | 0.1723 | | 0.1691 | 0.1717 | | |
| Energy density : $H(r)$ | -0.08810 | -0.07893 | -0.07234 | -0.08682 | -0.07958 | -0.07013 | -0.1109 | -0.09803 | -0.09823 | | -0.09484 | -0.09761 | | |
| Laplacian of electron density : $\nabla^2 \rho$ | -0.2105 | -0.1825 | -0.1625 | -0.2066 | -0.1845 | -0.1555 | -0.2805 | -0.2424 | -0.2425 | | -0.2324 | -0.2407 | | |
| Electron localization function (ELF) | 0.9392 | 0.9354 | 0.9319 | 0.9387 | 0.9357 | 0.9303 | 0.9453 | 0.9434 | 0.9431 | | 0.9423 | 0.9430 | | |
| Localized orbital locator (LOL) | 0.7972 | 0.7920 | 0.7872 | 0.7966 | 0.7923 | 0.7851 | 0.8061 | 0.8033 | 0.8029 | | 0.8017 | 0.8027 | | |
| Ellipticity of electron density ϵ | 0.01822 | 0.01302 | 0.01073 | 0.01751 | 0.01301 | 0.01054 | 0.01649 | 0.009943 | 0.009495 | | 0.009828 | 0.009177 | | |

by a drastic color change (electrochromism). As a result of a dynamic change in structure, the oxidation potential of the neutral states and the reduction potential of the oxidation states are largely separated, so that they exhibit high electrochemical bistability. Based on such electrochemical behaviors, *dyrex* systems are very useful from the viewpoint of making molecular devices controlled by electric potential.

As presumed by an *s-cis*-type 1,2-diphenylethane model, the σ^+ -orbital of the central C–C bond can interact with the π^+ -orbital on two units of π -electron systems (through-bond interaction; TBI), which could make new orbitals (i.e., $\sigma^+ + \pi^+$ and $\sigma^+ - \pi^+$, Fig. 3.8). As a result, the energy level of the $\sigma^+ - \pi^+$ orbital can be higher than that of the π^- orbital (original HOMO). If we consider that the overlap between Csp^3 orbitals should be depleted, expansion of the central C–C single bond would raise the σ^+ level. The closeness of the σ^+ and π^+ levels could cause a greater energy splitting between $\sigma^+ + \pi^+$ and $\sigma^+ - \pi^+$ orbitals, which results in raising the HOMO level. Therefore, TBI in HPEs plays an important role in modifying the MO level that determines their electron-donating properties.

HPE-type compound **I** [38–41], some of which have been shown to have a longer C–C bond ($>1.60 \text{ \AA}$) than the standard (1.54 \AA), is representative members of *dyrex* systems. As shown in Scheme 3.7, upon two-electron oxidation of HPE derivatives

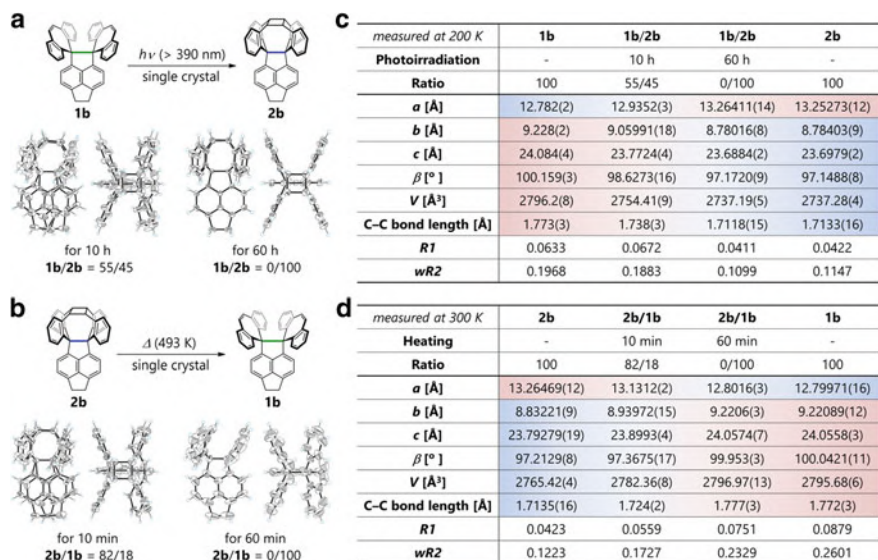


Fig. 3.7 (a) Upon photoirradiation of a single crystal of **1b** with $\lambda > 390$ nm for 10 and 60 h, the SCSC photocycloaddition reaction proceeded in respective yields of 45 and 100%, which were determined by single-crystal X-ray analysis at 200 K. (b) When a single crystal of **2b** was heated at 493 K for 10 and 60 min, SCSC thermal cycloreversion proceeded in respective yields of 18 and 100%, which were determined by single-crystal X-ray analysis at 300 K. Thermal ellipsoids are shown at the 30% probability level for intermediates and the 50% probability level for completely converted samples. (c, d) The crystallographic data for **1b** and **2b** are summarized in the table

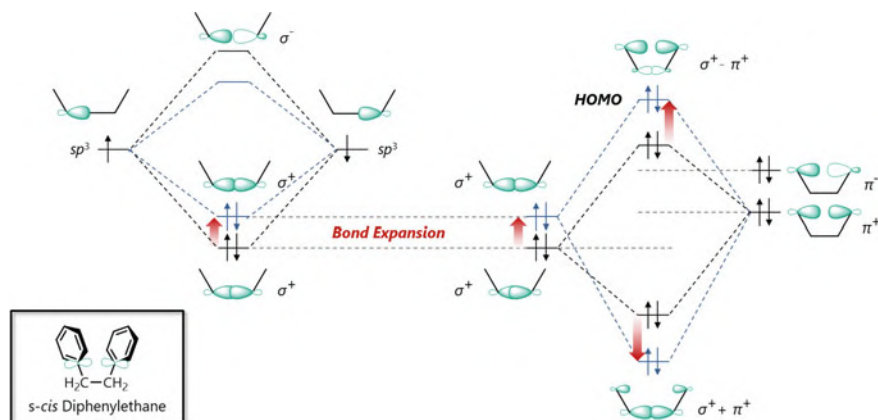
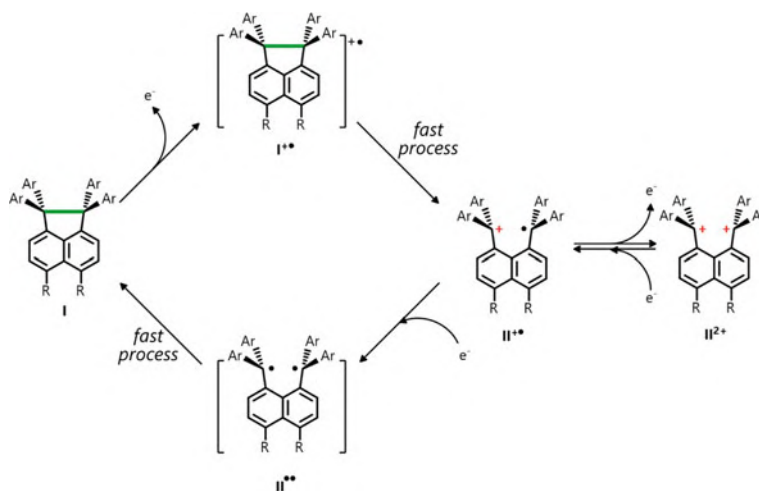


Fig. 3.8 Bond expansion raises the HOMO level via TBI in the diphenylethane model



Scheme 3.7 Redox mechanism in *dyrex* systems

I, C–C bond cleavage occurs to generate bond-dissociated dication II^{2+} , which undergo two-electron reduction to regenerate HPEs **I**. In the voltammograms, both one-wave two-electron oxidation and reduction peaks were observed without any other peaks, whose mechanism was previously proposed [39, 42].

In the oxidation processes of σ -bonded donors **I**, cation radicals $\text{I}^{\bullet\bullet}$ generated by one-electron oxidation would immediately convert to more stable cation radicals $\text{II}^{\bullet\bullet}$ because of rapid bond cleavage. Since the oxidation potential of cation radicals $\text{II}^{\bullet\bullet}$ is much less positive than that of σ -bonded species **I**, cation radicals $\text{II}^{\bullet\bullet}$ preferentially undergo oxidation, and thus the steady-state concentration of both cation radicals $\text{I}^{\bullet\bullet}$ and $\text{II}^{\bullet\bullet}$ would be negligible in the oxidation process. On the other hand, a stepwise reduction process could be observed because reduction potentials of two cationic sites in II^{2+} would be marginally separated due to an electronic interaction of the two triarylmethyl units. However, the steady-state concentration of both cation radicals $\text{II}^{\bullet\bullet}$ and diradicals $\text{II}^{\bullet\bullet}$ would also be negligible because of disproportionation of $\text{II}^{\bullet\bullet}$ into $\text{II}^{\bullet\bullet}/\text{II}^{2+}$ as well as fast bond formation in $\text{II}^{\bullet\bullet}$. Therefore, one-wave two-electron redox waves could be apparently observed.

Based on such background, the author has investigated redox behavior of **1a–1c** and **2a–2c** with a much longer C–C bond. The redox potentials of spiro-DBCHT **1a–1c** and caged molecules **2a–2c** were measured by cyclic voltammetry in CH_2Cl_2 at ambient temperature (Fig. 3.9a). While two electron oxidation occurs at lower potentials for the former with an expanded bond (E^{ox}/V vs. SCE: +0.93 for **1a**, +0.65 for **1b**, and +0.57 and +0.69 for **1c**), one-wave two-electron oxidation peaks appeared at much higher potentials for the latter with a contracted bond (E^{ox}/V : +1.59 for **2a**, +1.36 for **2b**, and +1.66 for **2c**) (Fig. 3.9a, d). Especially in **1c/2c**, the author found the largest difference in potential of about 1.1 eV before and after photocyclization. This change can be explained as follows: (i) the through-bond

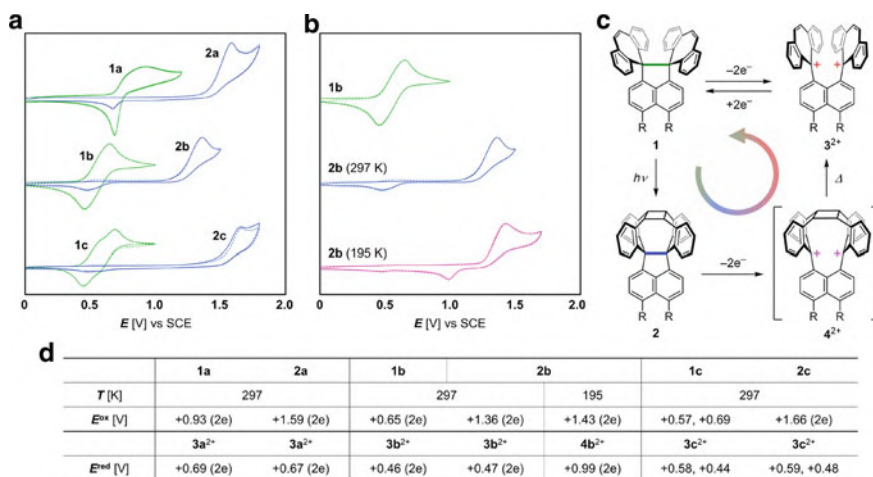


Fig. 3.9 Cyclic voltammograms of (a) **1** and **2** at 297 K and (b) **1b**, **2b** (at 297 K), and **2b** (at 195 K) in CH_2Cl_2 containing 0.1 M Bu_4NBF_4 as a supporting electrolyte (scan rate 0.1 V s^{-1} , Pt electrode). The second cycles are shown by a dotted line. (c) Mechanism of redox interconversion. (d) Redox potentials are summarized, and peak potentials are shown as E^{ox} and E^{red} . (a): R=H; b: R,R= $\text{CH}_2\text{-CH}_2$; c: R,R= CH=CH)

interaction that causes an increasing in the HOMO level would be maximized by expansion of the C–C single bond (Fig. 3.10) [41, 43] and (ii) the coefficients in HOMO are located on the DBCHT unit and the elongated σ -bond in **1**, whereas the coefficients are located on the acenaphthene, pyracene, or dihydropyracene skeleton in **2** based on DFT calculations (Fig. 3.2). On the other hand, two-electron reduction peaks were found in the far cathodic region due to cleavage of the elongated C–C bond to give 3^{2+} or **4** (*dyrex* behavior). It should be noted that reduction peaks in the voltammograms of **1** and **2** appear at almost the same potentials, indicating that the two-electron oxidation of caged molecules **2** could induce not only scission of the central C–C bond but also cleavage of cyclobutane ring.

To gain further insight into the mechanism of three-bond scission in the oxidation of **2**, the author conducted cyclic voltammetry at 195 K in CH_2Cl_2 using **2b**. As shown in Fig. 3.9b, d, another reduction peak appeared at a less cathodic region (E^{red}/V : +0.99), which is far different from that in the reduction of $3b^{2+}$ (E^{red}/V : +0.46), and thus caged dication $4b^{2+}$ was generated by the oxidation of **2b** through scission of the central C–C bond at low temperature, whereas thermal cleavage of the cyclobutane ring of $4b^{2+}$ produces bond-dissociated dication $3b^{2+}$ at room temperature.

Based on the voltammetric analysis, deeply colored dications $3a^{2+}$ – $3c^{2+}$ were successfully isolated as stable $(\text{SbCl}_6^-)_2$ salts by treatment of spiro-DBCHT **1a**–**1c** with two equivalents of $(4\text{-BrC}_6\text{H}_4)_3\text{N}^+\text{SbCl}_6^-$ in CH_2Cl_2 , due to stabilization of the dibenzotropylium units (Scheme 3.7, Fig. 3.10). Although formation of the same dication from caged molecules **2** was demonstrated by the electrochemical oxidation of **1b/2b** and **1c/2c** (Fig. 3.11), **2a**–**2c** with lower HOMO levels need a stronger

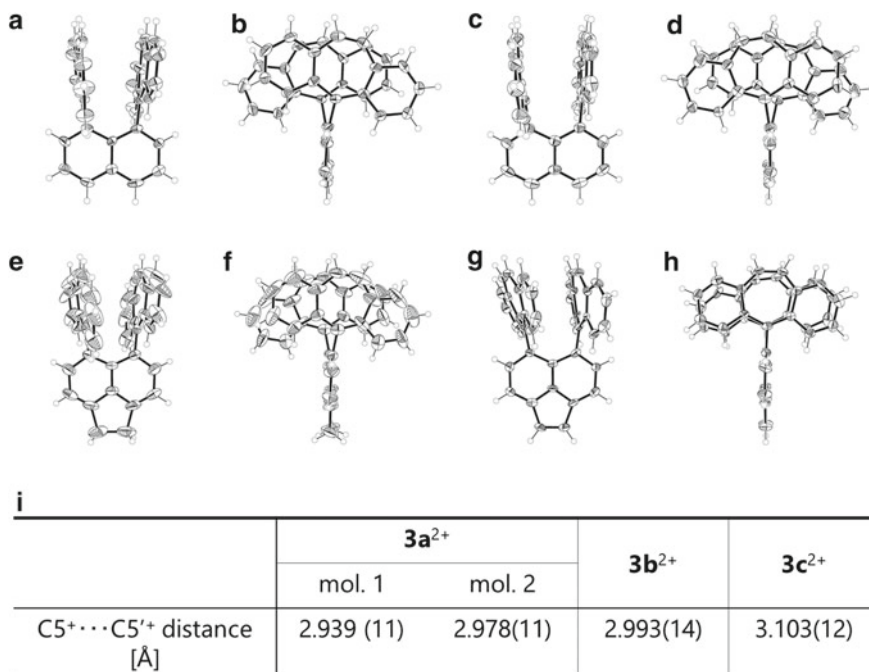


Fig. 3.10 ORTEP drawings of (a) mol. 1 and (b) mol. 2 of $2a^{2+}(\text{SbCl}_6^-)_2$, (c) $2b^{2+}(\text{SbCl}_6^-)_2$, and (d) $2c^{2+}(\text{SbCl}_6^-)_2$. There are two crystallographically independent molecules (mol. 1 and mol. 2) in $2a^{2+}(\text{SbCl}_6^-)_2$. Solvent molecules and counterions are omitted for clarity. Thermal ellipsoids are shown at the 50% probability level. (I) The distance between cationic centers (C5 $^+$...C5 $^+$ atoms) on the X-ray structure for $2a^{2+}$ – $2c^{2+}$

oxidant (2,4-Br $_2$ C $_6$ H $_3$) $_3$ N $^{+}$ SbCl $_6^-$ in CH $_2$ Cl $_2$ to give the same dication $3a^{2+}$ – $3c^{2+}$ (Scheme 3.8). Thus, completely selective oxidation of **1b** in a 1:1 mixture of **1b** and **2b** was achieved by using (4-BrC $_6$ H $_4$) $_3$ N $^{+}$ SbCl $_6^-$ (Scheme 3.9). This means that spiro-DBCHT **1** can be protected against oxidation by photoconversion into caged molecules **2** with a lower HOMO level.

The author then considered that both spiro-DBCHT **1** and caged molecules **2** could react with an oxidant to produce dication 3^{2+} in a solid state. When **1b** was subjected to grinding with two equivalents of blue-colored (4-BrC $_6$ H $_4$) $_3$ N $^{+}$ SbCl $_6^-$, the color changed to deep purple with the formation of dicationic dye $3b^{2+}$, which was confirmed by the appearance of characteristic IR absorptions assigned to $3b^{2+}(\text{SbCl}_6^-)_2$ (e.g., 1601 and 1385 cm $^{-1}$) and the resulting amine (e.g., 1486 and 1311 cm $^{-1}$) (Fig. 3.12a, d). Moreover, grinding of **2b** with two equivalents of green-colored (2,4-Br $_2$ C $_6$ H $_3$) $_3$ N $^{+}$ SbCl $_6^-$ smoothly led to the formation of a deep purple powder of dication salt $3b^{2+}(\text{SbCl}_6^-)_2$, where three-bond scission proceeded in a solid state (Fig. 3.12b, e). Additionally, upon grinding of $3b^{2+}(\text{SbCl}_6^-)_2$ with an excess amount of Zn powder, $3b^{2+}$ underwent two-electron reduction to give long bonded **1b** (Fig. 3.12c, f). This is the first example of flexible C–C bond exhibiting

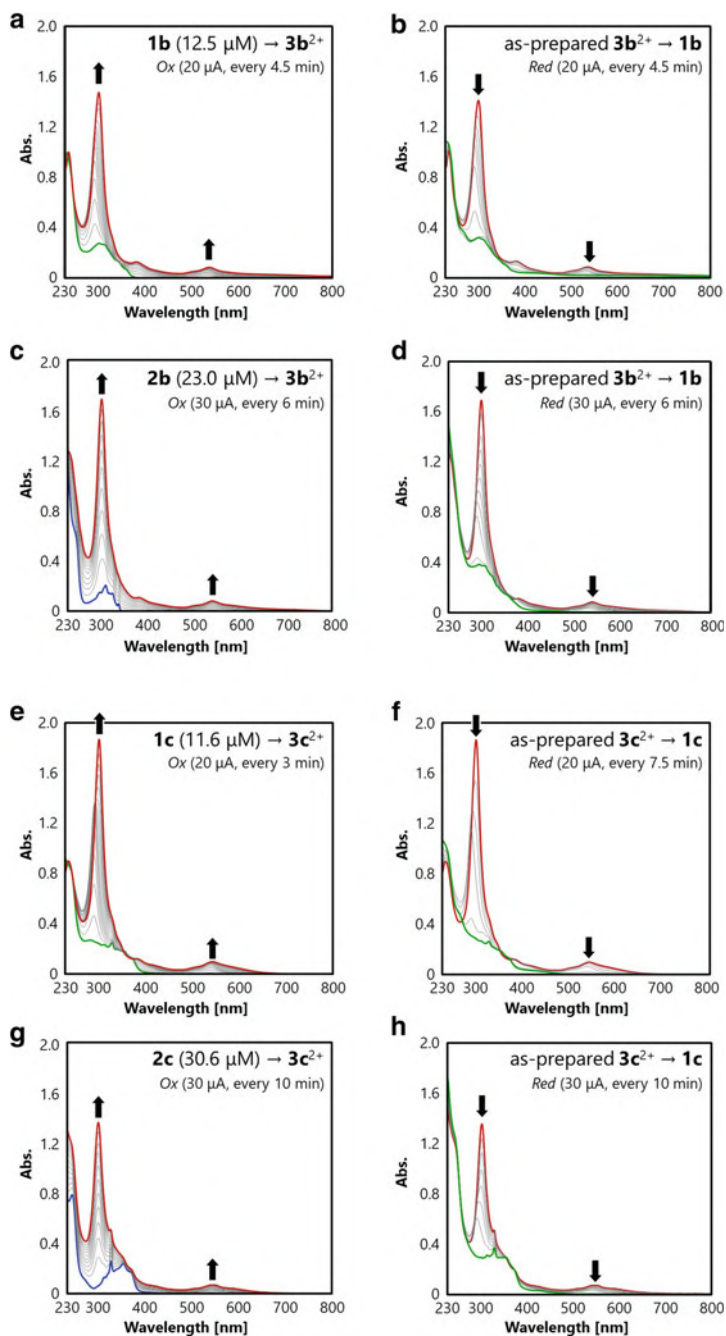
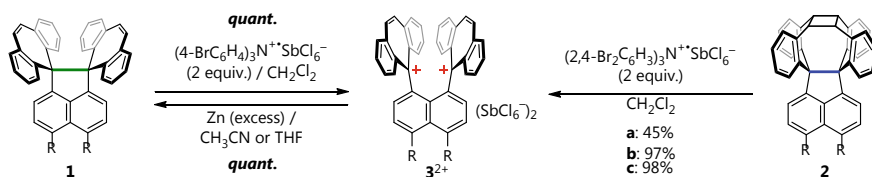
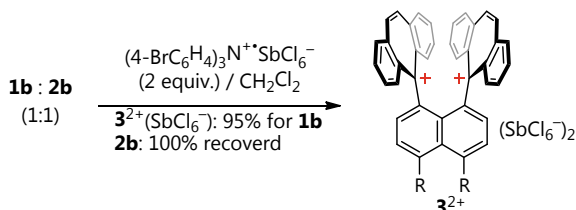


Fig. 3.11 Changes in the UV/Vis spectra of **1b/2b** and **1c/2c** upon constant-current electrochemical oxidation and as-prepared **3b²⁺** and **3c²⁺** upon constant-current electrochemical reduction in CH_2Cl_2 containing 0.05 M Bu_4NBF_4 as a supporting electrolyte



Scheme 3.8 Chemical oxidation of **1a–1c** and **2a–2c** and reduction of **3a²⁺–3c²⁺**

Scheme 3.9 Selective oxidation of the mixture of **1b:2b** (1:1)



the reversible expansion, contraction, formation, and scission of a Csp^3 – Csp^3 single bond in a simple organic compound, especially in a pure hydrocarbon.

3.3 Conclusion

The author has demonstrated that photo- and thermal isomerization between spiro-DBCHT **1** and caged molecules **2** proceeded quantitatively in a solid state, where the reversible formation and scission of two C–C bonds were accompanied by expansion and contraction of the central C–C bond (Scheme 3.10). Since formation of the cyclobutane ring and contraction of the C–C bond induce lowering of the HOMO level through an efficient TBI, oxidative properties can be deactivated/activated by light/heat. Caged molecules **2** generated by the photoirradiation of spiro-DBCHT **1** undergo two-electron oxidation to transiently produce bond-dissociated dications **4²⁺** followed by thermal cleavage of the cyclobutane ring to give stable dications **3²⁺**. An elongated C–C bond was reformed by two-electron reduction of dications **3²⁺**, resulting in the formation of original spiro-DBCHT **1**. Notably, all of these processes can proceed in a solid state. This study in this chapter provides a new perspective on C–C bonds that exhibit reversible expansion, contraction, formation, and scission. Thus, hydrocarbons that contain a “flexible” C–C bond could be promising candidates for the development of functional materials, whose crystals, films, or polymers can respond to the external stimuli such as light and heat with anisotropic expansion and contraction of the matter as well as reversible switching of oxidative properties.

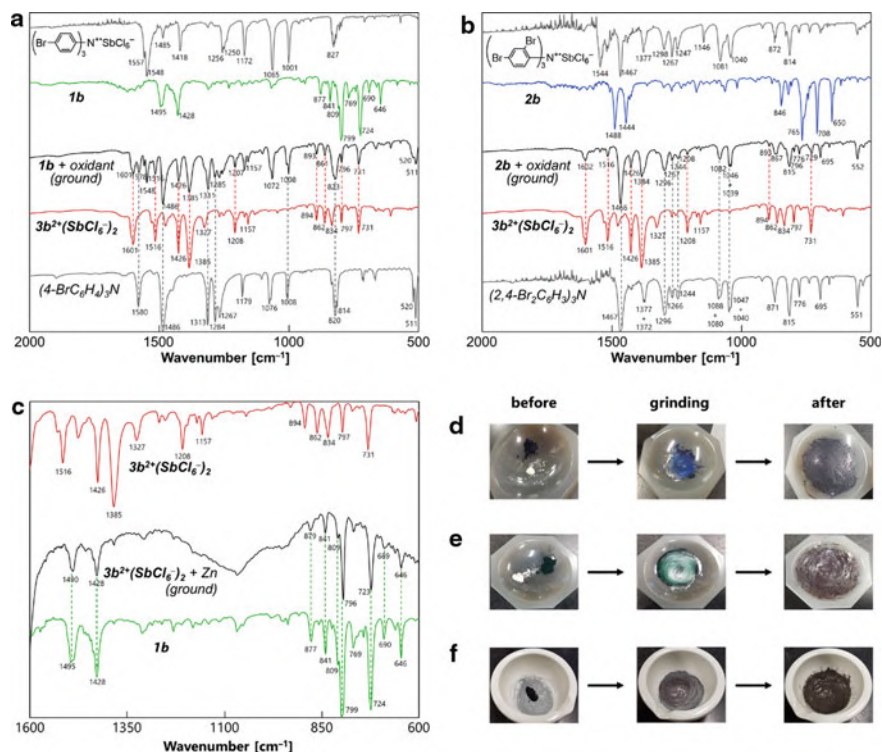
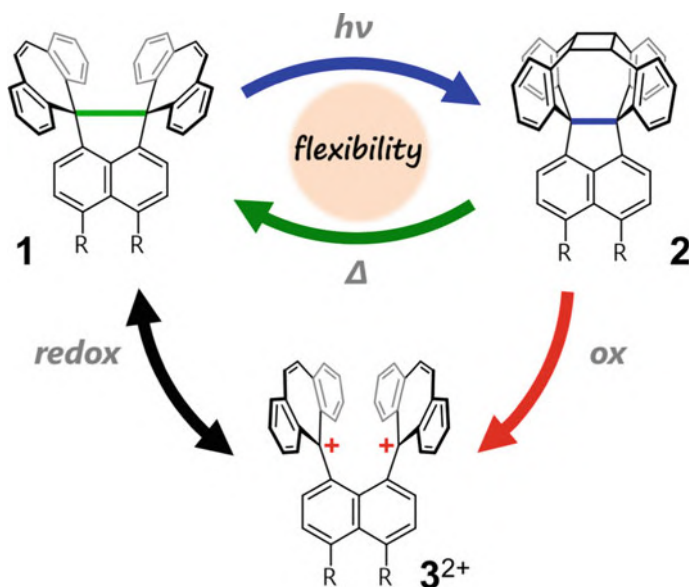


Fig. 3.12 (a) Solid-state oxidation of **1b** with two equivalents of $(4\text{-BrC}_6\text{H}_4)_3\text{N}^+\text{SbCl}_6^-$ was confirmed by IR spectroscopy. (b) Solid-state oxidation of **2b** with two equivalents of $(2,4\text{-Br}_2\text{C}_6\text{H}_3)_3\text{N}^+\text{SbCl}_6^-$ as a stronger oxidant was confirmed by IR spectroscopy. (c) Solid-state reduction of $3\text{b}^{2+}(\text{SbCl}_6^-)_2$ with an excess amount of Zn powder was confirmed by IR spectroscopy. Photographs showing mechano-oxidation of (d) **1b** with $(4\text{-BrC}_6\text{H}_4)_3\text{N}^+\text{SbCl}_6^-$ and (e) **2b** with $(2,4\text{-Br}_2\text{C}_6\text{H}_3)_3\text{N}^+\text{SbCl}_6^-$, and (f) mechano-reduction of $3\text{b}^{2+}(\text{SbCl}_6^-)_2$ with an excess amount of Zn powder

3.4 Experimental Section

General Procedures

All reactions were carried out under an argon atmosphere. All commercially available compounds were used without further purification unless otherwise indicated. Dry CH_3CN was obtained by distillation from CaH_2 prior to use. Column chromatography was performed on silica gel 60N (KANTO KAGAKU, spherical neutral) of particle size 40–50 μm or Wakogel[®] 60N (neutral) of particle size 38–100 μm . ^1H and ^{13}C NMR spectra were recorded on a BRUKER Ascend[™] 400 ($^1\text{H}/400$ MHz and $^{13}\text{C}/100$ MHz) spectrometer. IR spectra were measured as a KBr pellet on a JEOL JIR-WINSPEC100 FT/IR spectrophotometer. Mass spectra were recorded on a JMS-T100GCV spectrometer in FD mode by Dr. Eri Fukushi and Mr. Yusuke



Scheme 3.10 Graphical summary of this chapter

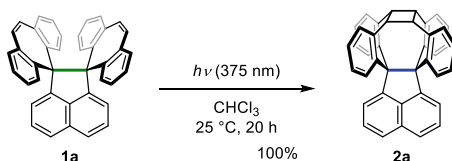
Takata (GC-MS & NMR Laboratory, Research Faculty of Agriculture, Hokkaido University). Melting points were measured on a Yamato MP-21 and are uncorrected. UV/Vis spectra were recorded on a Hitachi U-3500 spectrophotometer. Fluorescence spectra were measured on a Hitachi F-7000 spectrofluorometer. Fluorescence quantum yields were determined by using 9,10-diphenylanthracene ($\Phi_F = 0.97$) as an external standard [44]. For photoisomerization reaction, the Hitachi F-7000 spectrofluorometer was used for UV/Vis and NMR monitoring, and a Contec black light PW-UV943H-04 [375 nm light-emitting diode (LED)] and an Ushiospax SX-UID501XAMQ light source device with a CORNING COLOR FILTER (No. 3-73) were used on a preparative scale and on a single crystal, respectively. The analysis of Raman spectroscopy was carried out with inVia Reflex at the OPEN FACILITY, Hokkaido University Sousei Hall. Redox potentials (E^{ox} and E^{red}) were measured by cyclic voltammetry in dry CH_2Cl_2 containing 0.1 M Bu_4NBF_4 as a supporting electrolyte. All of the values shown in the text are in E/V versus SCE measured at the scan rate of 0.1 V s^{-1} . Pt electrodes were used as the working (disk) and counter electrodes. The working electrode was polished using a water suspension of aluminum oxide ($0.05 \mu\text{m}$) before use. DFT calculations were performed with the Gaussian 16W program package [45]. Version 3.8 of the Multiwfn software [46] was used for topological analysis of the electron density that is obtained by DFT calculations. The NBO analyses were performed with the Version 7.0 of the NBO [47] which was implemented in the Gaussian 16W program. The atomic coordinates were obtained from crystal structures of **1a–1c** and **2a–2c** at each temperature and the wave function was calculated at B3LYP-D3/6-311+G** for AIM and NBO analyses.

Preparation

- Preparation of caged molecules **2a–2c**

Caged molecule **2a**

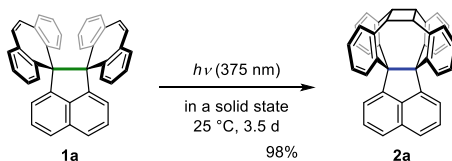
Photoisomerization of **1a** in solution:



A solution of **1a** (246 mg, 485 μmol) in CHCl_3 (100 mL) was photoirradiated with a 375 nm LED at 25 $^\circ\text{C}$ for 20 h, and then the solution was evaporated under reduced pressure. The residue was dissolved in CH_2Cl_2 , and the resulting solution was filtered through a silica gel pad. The filtrate was concentrated under reduced pressure and dried in vacuo to give **2a** (245 mg) as a white solid in 100% yield.

mp: same as **1a** [245–249 $^\circ\text{C}$ (decomp.)] [16] because of thermal isomerization from **2** to **1a**; ^1H NMR (CDCl_3): δ 8.00 (d, $J = 8.1$ Hz, 2H), 7.78 (dd, $J = 7.1$ Hz, 8.1 Hz, 2H), 7.19 (d, $J = 7.1$ Hz, 2H), 6.84–6.76 (m, 8H), 6.68 (dd, $J = 0.9$ Hz, 8.2 Hz, 4H), 6.57 (ddd, $J = 2.0$ Hz, 6.9 Hz, 8.2 Hz, 4H), 4.71 (s, 4H); ^{13}C NMR (CD_2Cl_2): δ 148.79, 143.72, 139.51, 137.10, 132.28, 131.69, 131.56, 127.90, 127.73, 127.06, 125.35, 123.65, 76.61, 47.76; IR (KBr): 3054, 3023, 2941, 1487, 1444, 1364, 1298, 1268, 1175, 1066, 1016, 817, 792, 764, 742, 711, 650, 590 cm^{-1} ; LRMS (FD): m/z (%) 508.25 (10), 507.25 (45), 506.25 (M^+ , bp); HRMS (FD) m/z : [M] $^+$ calcd. for $\text{C}_{40}\text{H}_{28}$, 506.20345; found, 506.20320; UV/Vis (CH_2Cl_2): $\lambda_{\text{max}}/\text{nm}$ ($\epsilon/\text{L mol}^{-1} \text{cm}^{-1}$) 291 (5900), 303 (7400), 312 (5150), 317 (4500), 330 (800); UV/Vis (CHCl_3): 291 (5930), 303 (7550), 312 (5450), 317 (4880), 331 (1080); Fluorescence (CHCl_3 , $\lambda_{\text{ex}} = 300$ nm): $\lambda_{\text{em}}/\text{nm}$ (Φ_{F}) 340, 350 (0.11).

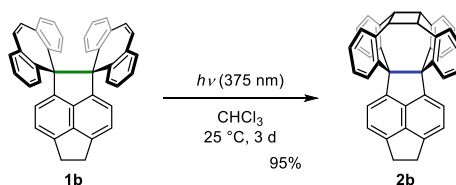
Photoisomerization of **1a** in a solid state:



A solid of **1a** (4.0 mg, 7.90 μmol) was photoirradiated with a 375 nm LED at 25 $^\circ\text{C}$ for 3.5 d to give **2a** (3.9 mg) as a white solid in 98% yield.

Caged molecule **2b**

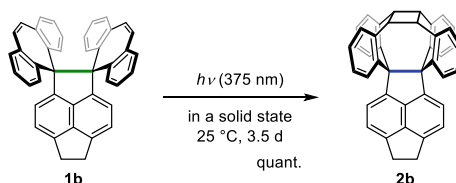
Photoisomerization of **1b** in solution:



A solution of **1b** (52.8 mg, 99.1 μmol) in CHCl_3 (15 mL) was photoirradiated with a 375 nm LED at 25 $^\circ\text{C}$ for 3 d, and then the solution was evaporated under reduced pressure. The residue was dissolved in CH_2Cl_2 , and the resulting solution was filtered through a silica gel pad. The filtrate was concentrated under reduced pressure and dried in vacuo to give **2b** (50.2 mg) as a white solid in 95% yield.

mp: same as **1b** [250–260 $^\circ\text{C}$ (decomp.)] [16] because of thermal isomerization from **2** to **1b**; $^1\text{H NMR}$ (CDCl_3): δ 7.55 (d, $J = 7.0$ Hz, 2H), 7.15 (d, $J = 7.0$ Hz, 2H), 6.84–6.76 (m, 12H), 6.58 (ddd, $J = 2.0$ Hz, 7.1 Hz, 8.5 Hz, 4H), 4.71 (s, 4H), 3.70 (s, 4H); $^{13}\text{C NMR}$ (CDCl_3): δ 143.49, 143.35, 143.39, 139.30, 139.18, 135.73, 131.67, 131.59, 128.86, 127.14, 125.54, 120.55, 80.30, 47.85, 31.98; IR (KBr): 3052, 3015, 2934, 1488, 1444, 1299, 1268, 1230, 1173, 1063, 1016, 943, 881, 846, 818, 806, 765, 733, 708, 650, 643, 616, 551 cm^{-1} ; LRMS (FD): m/z (%) 534.27 (12), 533.27 (50), 532.26 (M^+ , bp); HRMS (FD) m/z : [M] $^+$ calcd. for $\text{C}_{42}\text{H}_{28}$, 532.21910; found, 532.21988; UV/Vis (CH_2Cl_2): $\lambda_{\text{max}}/\text{nm}$ ($\epsilon/\text{L mol}^{-1} \text{ cm}^{-1}$) 298 (6870), 310 (9400), 318 (6430), 325 (6400), 338 (2370); UV/Vis (CHCl_3): 298 (6950), 310 (9550), 318 (6730), 325 (6800), 338 (2780); Fluorescence (CHCl_3 , $\lambda_{\text{ex}} = 300$ nm): $\lambda_{\text{em}}/\text{nm}$ (Φ_{F}) 347, 354 (0.01).

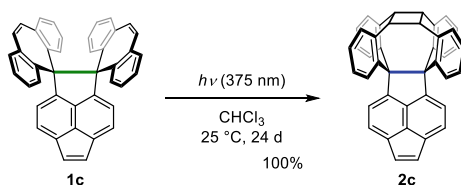
Photoisomerization of **1b** in a solid state:



A solid of **1b** (9.7 mg, 18.2 μmol) was photoirradiated with a 375 nm LED at 25 $^\circ\text{C}$ for 3.5 d to give **2b** (9.8 mg) as a white solid in quantitative yield.

Caged molecule **2c**

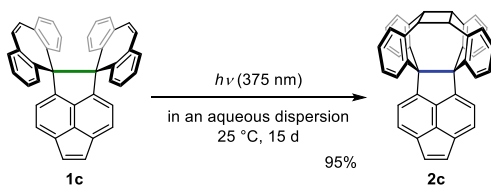
Photoisomerization of **1c** in solution:



A solution of **1c** (155 mg, 292 μmol) in CHCl_3 (100 mL) was photoirradiated with a 375 nm LED at 25 $^\circ\text{C}$ for 24 d, and then the solution was evaporated under reduced pressure. The residue was purified by silica gel column chromatography (hexane/ $\text{CH}_2\text{Cl}_2 = 5$) to give **2c** (155 mg) as a pale yellow solid in 100% yield.

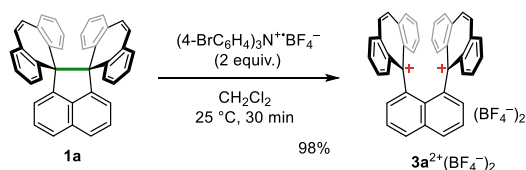
mp: same as **1c** [250–258 $^\circ\text{C}$ (decomp.)] [16] because of thermal isomerization from **2** to **1c**; $^1\text{H NMR}$ (CDCl_3): δ 8.07 (d, $J = 7.1$ Hz, 2H), 7.36 (s, 2H), 7.35 (d, $J = 7.1$ Hz, 2H), 6.85–6.78 (m, 12H), 6.57 (ddd, $J = 2.0$ Hz, 6.9 Hz, 8.5 Hz, 4H), 4.71 (s, 4H); $^{13}\text{C NMR}$ (CDCl_3): δ 150.57, 142.65, 139.30, 136.27, 132.60, 131.78, 131.36, 129.25, 128.83, 127.38, 127.21, 126.36, 125.64, 81.27, 47.76; IR (KBr): 3053, 3024, 2939, 1625, 1596, 1488, 1468, 1443, 1417, 1364, 1173, 1081, 955, 846, 765, 726, 707, 671, 650, 615 cm^{-1} ; LRMS (FD) m/z (%): 532.25 (13), 531.25 (46), 530.25 (M^+ , bp); HRMS (FD) m/z : [M] $^+$ calcd. for $\text{C}_{42}\text{H}_{26}$, 530.20345; found, 530.20410; UV/Vis (CH_2Cl_2): $\lambda_{\text{max}}/\text{nm}$ ($\epsilon/\text{L mol}^{-1} \text{cm}^{-1}$) 314 (3800), 329 (8250), 340 (6200), 355 (7850), 370 (5780); UV/Vis (CHCl_3): 314 (4120), 329 (8440), 340 (6380), 356 (8060), 372 (6060); Fluorescence (CHCl_3 , $\lambda_{\text{ex}} = 300$ nm): $\lambda_{\text{em}}/\text{nm}$ (Φ_{F}) 347, 364, 385 (0.004).

Photoisomerization of **1c** in a solid state:



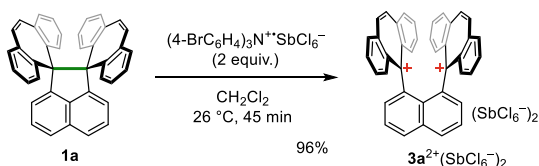
An aqueous dispersion of **1c** (8.5 mg, 16.0 μmol) in water (6 mL) was photoirradiated with a 375 nm LED at 25 $^\circ\text{C}$ for 15 d, and then filtered to give **2c** (8.4 mg) as a pale yellow solid in 95% yield (NMR).

- Preparation of dication **3a** $^{2+}$ –**3c** $^{2+}$

Dicationic salt $3a^{2+}(BF_4^-)_2$ Oxidation of **1a** in solution:

To a solution of **1a** (40.5 mg, 79.9 μmol) in dry CH_2Cl_2 (5 mL) was added tris(4-bromophenyl)aminium tetrafluoroborate (90.9 mg, 160 μmol) at 25 $^\circ\text{C}$ to generate a deep purple solution, and the mixture was stirred at 25 $^\circ\text{C}$ for 30 min. The addition of dry Et_2O led to precipitation of the dication salt. The precipitates were collected, washed with dry Et_2O three times, and dried in vacuo to give $3a^{2+}(\text{BF}_4^-)_2$ (53.2 mg) as a deep purple powder in 98% yield.

mp: 213–216 $^\circ\text{C}$ (decomp.); $^1\text{H NMR}$ (CD_3CN): δ 8.75 (dd, $J = 1.2, 8.4$ Hz, 2H), 8.70 (s, 4H), 8.38 (dd, $J = 1.4, 8.1$ Hz, 4H), 8.24 (ddd, $J = 1.1, 6.9, 8.1$ Hz, 4H), 8.03 (dd, $J = 7.1, 8.4$ Hz, 2H), 7.83 (d, $J = 1.1, 8.3$ Hz, 4H), 7.53 (ddd, $J = 1.4, 6.9, 8.3$ Hz, 4H), 7.47 (dd, $J = 1.2, 7.1$ Hz, 2H); $^{13}\text{C NMR}$ (CD_3CN): δ 179.44, 146.01, 145.29, 141.32, 138.78, 138.72, 136.83, 136.60, 135.83, 134.86, 132.87, 132.40, 130.61, 126.79; IR (KBr): 3059, 2360, 1603, 1519, 1478, 1427, 1385, 1331, 1197, 1055, 899, 855, 799, 733 cm^{-1} ; LRMS (FD) m/z (%): 508.17 (11), 507.17 (45), 506.17 (M^+ , bp); HRMS (FD) m/z : [M] $^+$ calcd. for $\text{C}_{40}\text{H}_{26}$, 506.20345; found, 506.20484; UV/Vis (CH_2Cl_2): $\lambda_{\text{max}}/\text{nm}$ ($\epsilon/\text{L mol}^{-1} \text{cm}^{-1}$) 302 (78,300), 382 (5730), 540 (3400).

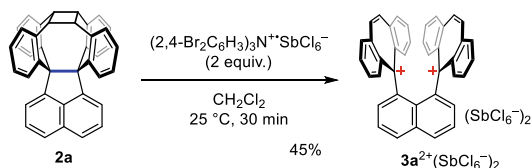
Dicationic salt $3a^{2+}(\text{SbCl}_6^-)_2$ Oxidation of **1a** in solution:

To a solution of **1a** (20.0 mg, 39.4 μmol) in dry CH_2Cl_2 (2 mL) was added tris(4-bromophenyl)aminium hexachloroantimonate (64.0 mg, 78.3 μmol) at 0 $^\circ\text{C}$ to generate a deep purple solution, and the mixture was stirred at 26 $^\circ\text{C}$ for 45 min. The addition of dry Et_2O led to precipitation of the dication salt. The precipitates were collected, washed with dry Et_2O three times, and dried in vacuo to give $3a^{2+}(\text{SbCl}_6^-)_2$ (44.4 mg) as a deep purple powder in 96% yield.

mp: 192–195 $^\circ\text{C}$ (decomp.); $^1\text{H NMR}$ (CD_3CN containing 10 vol% TFAA): δ 8.76 (dd, $J = 1.2, 8.4$ Hz, 2H), 8.69 (s, 4H), 8.38 (dd, $J = 1.4, 8.1$ Hz, 4H), 8.26

(ddd, $J = 1.1, 6.9, 8.1$ Hz, 4H), 8.05 (dd, $J = 7.1, 8.4$ Hz, 2H), 7.84 (d, $J = 1.1, 8.3$ Hz, 4H), 7.55 (ddd, $J = 1.4, 6.9, 8.3$ Hz, 4H), 7.49 (dd, $J = 1.2, 7.1$ Hz, 2H); IR (KBr): 3062, 2927, 1607, 1600, 1530, 1516, 1474, 1425, 1384, 1329, 1262, 1196, 1171, 1133, 1046, 1009, 895, 855, 834, 816, 801, 787, 769, 734 cm^{-1} ; LRMS (FD) m/z (%): 576.21 (6), 543.24 (6), 542.24 (18), 541.24 (22), 540.23 (43), 508.27 (11), 507.27 (44), 506.27 (M^+ , bp); HRMS (FD) m/z : $[M]^+$ calcd. for $C_{40}H_{26}$, 506.20345; found, 506.20228.

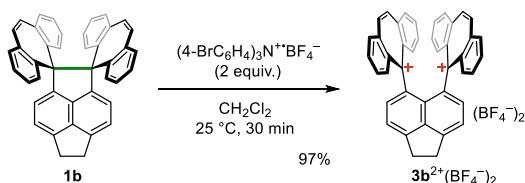
Oxidation of **2a** in solution:



To a solution of **2a** (8.5 mg, 16.8 μmol) in dry CH_2Cl_2 (2 mL) was added tris(2,4-dibromophenyl)aminium hexachloroantimonate (35.3 mg, 33.5 μmol) at 25 $^\circ\text{C}$ to generate a deep purple solution, and the mixture was stirred at 25 $^\circ\text{C}$ for 30 min. The addition of dry Et_2O led to the precipitation of the dication salt. The precipitates were collected, washed with dry Et_2O three times, and dried in vacuo to give $3\mathbf{a}^{2+}(\text{SbCl}_6^-)_2$ (8.8 mg) as a deep purple powder in 45% yield.

Dicationic salt $3\mathbf{b}^{2+}(\text{BF}_4^-)_2$

Oxidation of **1b** in solution:



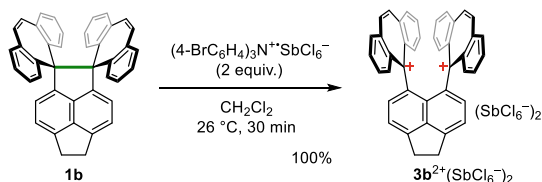
To a solution of **1b** (53.6 mg, 101 μmol) in dry CH_2Cl_2 (5 mL) was added tris(4-bromophenyl)aminium tetrafluoroborate (115 mg, 201 μmol) at 25 $^\circ\text{C}$ to generate a deep purple solution, and the mixture was stirred at 25 $^\circ\text{C}$ for 30 min. The addition of dry Et_2O led to the precipitation of the dication salt. The precipitates were collected, washed with dry Et_2O three times, and dried in vacuo to give $3\mathbf{b}^{2+}(\text{BF}_4^-)_2$ (69.5 mg) as a deep purple powder in 97% yield.

Mp: > 300 $^\circ\text{C}$; ^1H NMR (CD_3CN): δ 8.72 (s, 4H), 8.33 (dd, $J = 1.5, 8.1$ Hz, 4H), 8.17 (ddd, $J = 1.0, 7.0, 8.1$ Hz, 4H), 7.97 (dd, $J = 1.0, 8.9$ Hz, 4H), 7.86 (d, $J = 7.2$ Hz, 2H), 7.57 (ddd, $J = 1.5, 7.0, 8.9$ Hz, 4H), 7.44 (d, $J = 7.2$ Hz, 2H), 3.91 (s, 4H); ^{13}C NMR (CD_3CN): δ 180.66, 152.00, 145.52, 145.40, 141.45, 140.49, 139.37, 138.66, 136.32, 134.29, 134.17, 132.74, 129.60, 120.81, 31.11; IR (KBr):

3059, 2927, 2360, 1601, 1516, 1478, 1385, 1329, 1208, 1053, 896, 862, 838, 798, 732 cm^{-1} ; LRMS (FD) m/z (%): 551.18 (7), 550.18 (15), 534.20 (11), 533.19 (46), 532.19 (M^+ , bp), 531.18 (8), 530.18 (17); HRMS (FD) m/z : $[\text{M}]^+$ calcd. for $\text{C}_{42}\text{H}_{28}$, 532.21910; found, 532.21750; UV/Vis (CH_2Cl_2): $\lambda_{\text{max}}/\text{nm}$ ($\epsilon/\text{L mol}^{-1} \text{cm}^{-1}$) 302 (114,000), 380 (8310), 536 (5510).

Dicationic salt $3\mathbf{b}^{2+}(\text{SbCl}_6^-)_2$

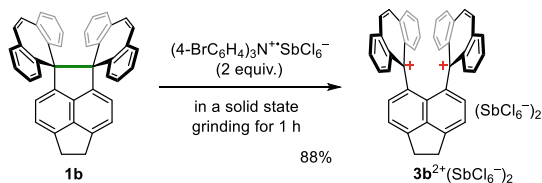
Oxidation of $1\mathbf{b}$ in solution:



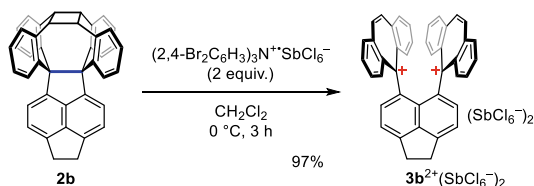
To a solution of **1b** (100 mg, 188 μmol) in dry CH_2Cl_2 (8 mL) was added tris(4-bromophenyl)aminium hexachloroantimonate (307 mg, 376 μmol) at $25\text{ }^\circ\text{C}$ to generate a deep purple solution, and the mixture was stirred at $25\text{ }^\circ\text{C}$ for 30 min. The addition of dry Et_2O led to the precipitation of the dication salt. The precipitates were collected, washed with dry Et_2O three times, and dried in vacuo to give $3\mathbf{b}^{2+}(\text{SbCl}_6^-)_2$ (226 mg) as a deep purple powder in 100% yield.

mp: $181\text{--}182\text{ }^\circ\text{C}$; $^1\text{H NMR}$ (CD_3CN containing 10 vol% TFAA): δ 8.70 (s, 4H), 8.32 (dd, $J = 1.5, 8.1\text{ Hz}$, 4H), 8.18 (ddd, $J = 1.0, 7.0, 8.1\text{ Hz}$, 4H), 7.99 (dd, $J = 1.0, 8.9\text{ Hz}$, 4H), 7.87 (d, $J = 7.2\text{ Hz}$, 2H), 7.59 (ddd, $J = 1.5, 7.0, 8.9\text{ Hz}$, 4H), 7.45 (d, $J = 7.2\text{ Hz}$, 2H), 3.91 (s, 4H); IR (KBr): 3174, 3107, 2927, 2360, 1601, 1529, 1516, 1476, 1426, 1385, 1327, 1268, 1253, 1208, 1172, 1157, 1132, 1077, 1044, 1007, 894, 862, 834, 797, 771, 731 cm^{-1} ; LRMS (FD) m/z (%): 602.22 (26), 600.22 (39), 568.26 (30), 567.26 (35), 566.25 (74), 533.29 (43), 532.29 (M^+ , bp), 530.27 (26); HRMS (FD) m/z : $[\text{M}]^+$ calcd. for $\text{C}_{42}\text{H}_{28}$, 532.21910, found, 532.22009.

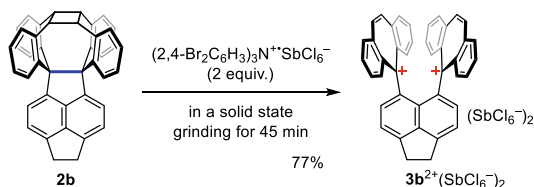
Oxidation of $1\mathbf{b}$ in a solid state:



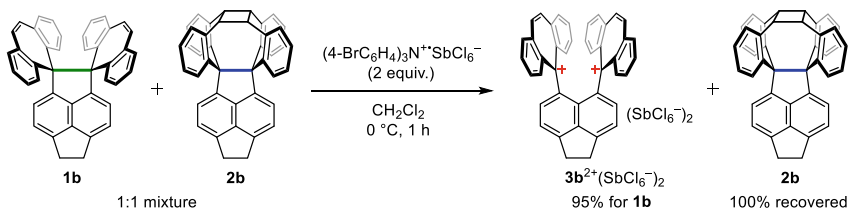
A mixture of **1b** (50.4 mg, 94.6 μmol) and tris(4-bromophenyl)aminium hexachloroantimonate (154 mg, 188 μmol) was ground for 1 h at $25\text{ }^\circ\text{C}$ to generate a deep purple solid. The resulting powder was collected, washed with dry Et_2O three times, and dried in vacuo to give $3\mathbf{b}^{2+}(\text{SbCl}_6^-)_2$ (100 mg) as a deep purple powder in 88% yield.

Oxidation of **2b** in solution:

To a solution of **2b** (20.5 mg, 38.5 μmol) in dry CH_2Cl_2 (3 mL) was added tris(2,4-dibromophenyl)ammonium hexachloroantimonate (81.2 mg, 77.1 μmol) at $0\text{ }^\circ\text{C}$ to generate a deep purple solution, and the mixture was stirred at $0\text{ }^\circ\text{C}$ for 3 h. The addition of dry Et_2O led to the precipitation of the dication salt. The precipitates were collected, washed with dry Et_2O three times, and dried in vacuo to give **3b**²⁺(SbCl_6^-)₂ (45.0 mg) as a deep purple powder in 97% yield.

Oxidation of **2b** in a solid state:

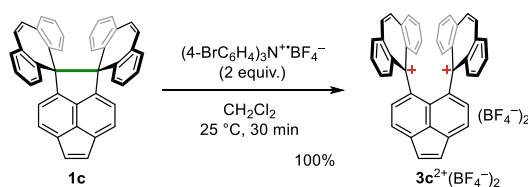
A mixture of **2b** (49.2 mg, 92.4 μmol) and tris(2,4-dibromophenyl)ammonium hexachloroantimonate (194 mg, 184 μmol) was ground for 45 min at $25\text{ }^\circ\text{C}$ to generate a deep purple solid. The resulting powder was collected, washed with dry Et_2O three times, and dried in vacuo to give **3b**²⁺(SbCl_6^-)₂ (84.6 mg) as a deep purple powder in 77% yield.

Selective oxidation of **1b** in a mixture of **1b** and **2b**:

To a solution of mixture of **1b** (49.1 mg, 92.2 μmol) and **2b** (49.2 mg, 92.4 μmol) in dry CH_2Cl_2 (4 mL) was added tris(4-bromophenyl)aminium hexachloroantimonate (151 mg, 184 μmol) at 0 $^\circ\text{C}$, and the mixture was stirred for 1 h. The addition of dry Et_2O led to the precipitation of the dication salt. The supernatant solution was removed by decantation. Then, the residue was suspended in dry CH_2Cl_2 , and the supernatant solution was removed by decantation. These procedures were repeated 3 times. The resulting residue was dried in vacuo to give **3b**²⁺(SbCl_6^-)₂ (105 mg) as a deep purple powder in 95% yield for **1b**. On the other hand, the combined filtrate was evaporated under reduced pressure. The residue was purified by silica gel column chromatography (hexane to CH_2Cl_2) to recover **2b** (49.2 mg) as a white solid in 100% yield for **2b**.

Dicationic salt **3c**²⁺(BF_4^-)₂

Oxidation of **1c** in solution:

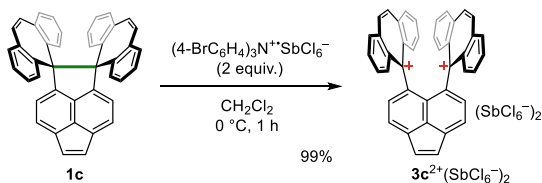


To a solution of **1c** (40.2 mg, 75.8 μmol) in dry CH_2Cl_2 (5 mL) was added tris(4-bromophenyl)aminium tetrafluoroborate (86.1 mg, 151 μmol) at 25 $^\circ\text{C}$ to generate a deep purple solution, and the mixture was stirred at 25 $^\circ\text{C}$ for 30 min. The addition of dry Et_2O led to the precipitation of the dication salt. The precipitates were collected, washed with dry Et_2O three times, and dried in vacuo to give **3c**²⁺(BF_4^-)₂ (53.7 mg) as a deep purple powder in 100% yield.

Mp: > 300 $^\circ\text{C}$; ¹H NMR (CD_3CN containing 10 vol% TFA-*d*): δ 8.76 (s, 4H), 8.36 (dd, $J = 1.2, 8.0$ Hz, 4H), 8.19 (ddd, $J = 1.1, 6.9, 8.0$ Hz, 4H), 8.17 (d, $J = 7.0$ Hz, 2H), 8.06 (brd, $J = 8.8$ Hz, 4H), 7.58 (s, 2H), 7.57 (ddd, $J = 1.2, 6.9, 8.8$ Hz, 4H), 7.51 (d, $J = 7.0$ Hz, 2H); ¹³C NMR (CD_3CN containing 10 vol% TFA-*d*): δ 179.38, 146.01, 145.53, 143.74, 141.79, 139.53, 138.57, 137.66, 136.64, 134.77, 133.66, 132.48, 129.87, 127.15, 125.40; IR (KBr): 3059, 2360, 2343, 1604, 1516, 1478, 1427, 1385, 1331, 1197, 1055, 899, 855, 840, 799, 775, 733 cm^{-1} ; LRMS (FD) m/z (%): 566.15 (8), 549.17 (6), 548.16 (13), 546.16 (5), 532.18 (12), 531.18 (46), 530.17 (M^+ , bp); HRMS (FD) m/z : [M]⁺ calcd. for $\text{C}_{42}\text{H}_{26}$, 530.20345; found, 530.20405; UV/Vis (CH_2Cl_2): λ_{max} /nm ($\epsilon/\text{L mol}^{-1} \text{cm}^{-1}$) 302 (82,400), 384 (7740), 542 (5630).

Dicationic salt $3c^{2+}(\text{SbCl}_6^-)_2$

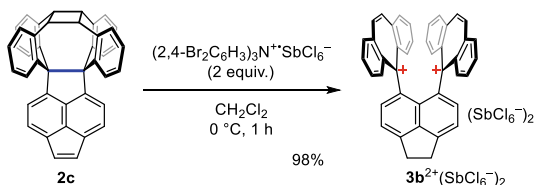
Oxidation of **1c** in solution:



To a solution of **1c** (20.1 mg, 37.9 μmol) in dry CH_2Cl_2 (2 mL) was added tris(4-bromophenyl)aminium hexachloroantimonate (61.6 mg, 75.4 μmol) at 0 $^\circ\text{C}$ to generate a deep purple solution, and the mixture was stirred at 0 $^\circ\text{C}$ for 1 h. The addition of dry Et_2O led to the precipitation of the dication salt. The precipitates were collected, washed with dry Et_2O three times, and dried in vacuo to give $3c^{2+}(\text{SbCl}_6^-)_2$ (45.0 mg) as a deep purple powder in 99% yield.

mp: 190–195 $^\circ\text{C}$; ^1H NMR (CD_3CN containing 10 vol% TFAA): δ 8.74 (s, 4H), 8.37 (brd, $J = 7.8$ Hz, 4H), 8.22–8.19 (m, 6H), 8.06 (brd, $J = 8.8$ Hz, 4H), 7.60–7.56 (m, 6H), 7.52 (d, $J = 7.0$ Hz, 2H); IR (KBr): 3081, 1666, 1660, 1602, 1530, 1515, 1504, 1495, 1480, 1463, 1453, 1427, 1387, 1357, 1331, 1265, 1209, 1197, 1172, 1158, 1132, 1094, 1044, 939, 893, 865, 834, 796, 780, 773, 731, 675, 642, 608 cm^{-1} ; LRMS (FD) m/z (%): 600.20 (23), 599.21 (26), 598.20 (26), 566.24 (18), 565.24 (23), 564.24 (44), 547.27 (13), 546.27 (31), 532.28 (13), 531.28 (51), 530.27 (M^+ , bp); HRMS (FD) m/z : [M] $^+$ calcd. for $\text{C}_{42}\text{H}_{26}$, 530.20345; found, 530.20437.

Oxidation of **2c** in solution:

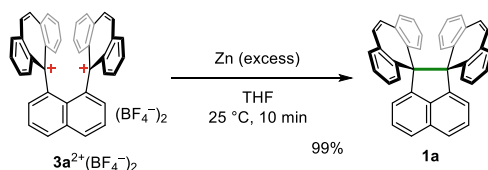


To a solution of **2c** (10.4 mg, 19.6 μmol) in dry CH_2Cl_2 (1.0 mL) was added tris(2,4-dibromophenyl)aminium hexachloroantimonate (41.2 mg, 39.1 μmol) at 0 $^\circ\text{C}$ to generate a deep purple solution, and the mixture was stirred at 0 $^\circ\text{C}$ for 1 h. The addition of dry Et_2O led to the precipitation of the dication salt. The precipitates were collected, washed with dry Et_2O three times, and dried in vacuo to give $3c^{2+}(\text{SbCl}_6^-)_2$ (23.1 mg) as a deep purple powder in 98% yield.

- Preparation of spiro-DBCHT **1a–1c**

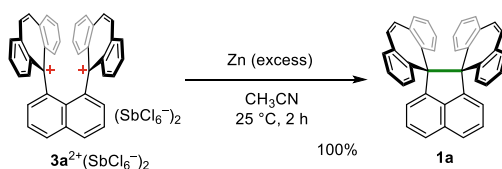
Spiro-DBCHT 1a

Reduction of $3a^{2+}(BF_4^-)_2$ in solution:



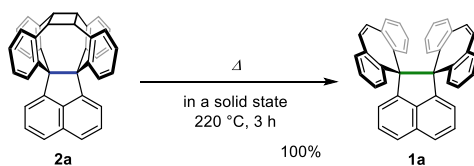
To a solution of $3a^{2+}(BF_4^-)_2$ (30.0 mg, 44.1 μmol) in dry THF (2 mL) was added activated zinc powder (434 mg, 6.64 mmol) at 25 $^\circ\text{C}$. The mixture was stirred for 10 min, and then diluted with water. The whole mixture was extracted with CHCl_3 three times. The combined organic layers were washed with water and brine, and dried over anhydrous MgSO_4 . After filtration through a silica gel pad, the solvent was concentrated under reduced pressure and dried in vacuo to give **1a** (22.2 mg) as a white solid in 99% yield.

Reduction of $3a^{2+}(SbCl_6^-)_2$ in solution:



To a solution of $3a^{2+}(SbCl_6^-)_2$ (104 mg, 88.2 μmol) in dry CH_3CN (4 mL) was added activated zinc powder (865 mg, 13.2 mmol) at 25 $^\circ\text{C}$ in the dark. The mixture was stirred for 2 h in the dark, and then diluted with water. The whole mixture was extracted with CHCl_3 three times. The combined organic layers were washed with water and brine, and dried over anhydrous MgSO_4 . After filtration, the solvent was concentrated under reduced pressure and dried in vacuo to give **1a** (44.5 mg) as a white solid in 100% yield.

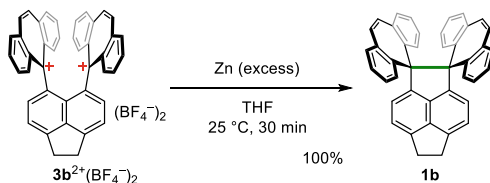
Thermal isomerization of **2a** in a solid state:



A solid of **2a** (1.6 mg, 3.16 μmol) was heated at 220 $^\circ\text{C}$ for 3 h to give **1a** (1.6 mg) as a white solid in 100% yield.

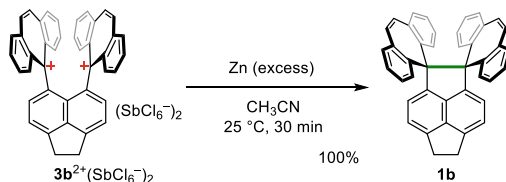
Spiro-DBCHT 1b

Reduction of $3b^{2+}(BF_4^-)_2$ in solution:



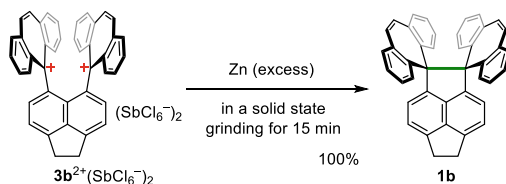
To a solution of $3b^{2+}(BF_4^-)_2$ (54.4 mg, 44.1 μmol) in dry THF (4 mL) was added activated zinc powder (756 mg, 11.6 mmol) at 25 °C. The mixture was stirred for 30 min, and then diluted with water. The whole mixture was extracted with CHCl_3 three times. The combined organic layers were washed with water and brine, and dried over anhydrous MgSO_4 . After filtration through a silica gel pad, the solvent was concentrated under reduced pressure and dried in vacuo to give **1b** (40.9 mg) as a white solid in 100% yield.

Reduction of $3b^{2+}(SbCl_6^-)_2$ in solution:



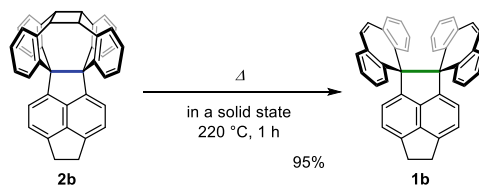
To a solution of $3b^{2+}(SbCl_6^-)_2$ (116 mg, 96.9 μmol) in dry CH_3CN (4 mL) was added activated zinc powder (974 mg, 14.9 mmol) at 25 °C. The mixture was stirred for 30 min, and then diluted with water. The whole mixture was extracted with CHCl_3 three times. The combined organic layers were washed with water and brine, and dried over anhydrous MgSO_4 . After filtration, the solvent was concentrated under reduced pressure and dried in vacuo to give **1b** (51.4 mg) as a white solid in 100% yield.

Reduction of $3b^{2+}(SbCl_6^-)_2$ in a solid state:



A mixture of $3\mathbf{b}^{2+}(\text{SbCl}_6^-)_2$ (100 mg, 83.4 μmol) and activated zinc powder (1.09 g, 16.6 mmol) was ground for 15 min at 25 $^\circ\text{C}$. The resulting powder was dissolved in CHCl_3 , and then the resulting suspension was filtered through filter paper. The filtrate was washed with water and brine, and dried over anhydrous MgSO_4 . After filtration through a silica gel pad, the solvent was evaporated and dried in vacuo to give $\mathbf{1b}$ (44.3 mg) as a white solid in 100% yield.

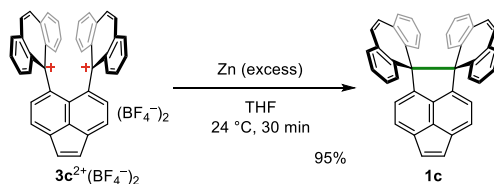
Thermal isomerization of $\mathbf{2b}$ in a solid state:



A solid of $\mathbf{2b}$ (2.1 mg, 3.94 μmol) was heated at 220 $^\circ\text{C}$ for 1 h to give $\mathbf{1b}$ (2.0 mg) as a white solid in 95% yield.

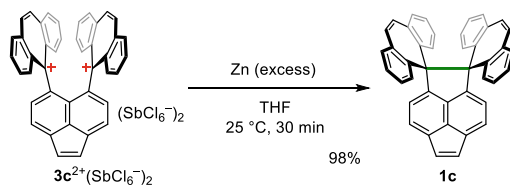
Spiro-DBCHT $\mathbf{1c}$

Reduction of $3\mathbf{c}^{2+}(\text{BF}_4^-)_2$ in solution:



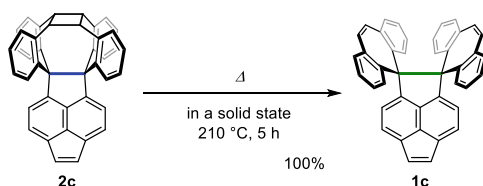
To a solution of $3\mathbf{c}^{2+}(\text{BF}_4^-)_2$ (20.7 mg, 29.4 μmol) in dry THF (2 mL) was added activated zinc powder (288 mg, 4.40 mmol) at 24 $^\circ\text{C}$. The mixture was stirred for 30 min, and then diluted with water. The whole mixture was extracted with CHCl_3 three times. The combined organic layers were washed with water and brine, and dried over anhydrous MgSO_4 . After filtration through a silica gel pad, the solvent was concentrated under reduced pressure and dried in vacuo to give $\mathbf{1c}$ (14.8 mg) as a yellow solid in 95% yield.

Reduction of $3\mathbf{c}^{2+}(\text{SbCl}_6^-)_2$ in solution:



To a solution of $3\mathbf{c}^{2+}(\text{SbCl}_6^-)_2$ (19.1 mg, 15.9 μmol) in dry THF (2 mL) was added activated zinc powder (157 mg, 2.39 mmol) at 25 $^\circ\text{C}$. The mixture was stirred for 30 min, and then diluted with water. The whole mixture was extracted with CHCl_3 three times. The combined organic layers were washed with water and brine, and dried over anhydrous MgSO_4 . After filtration through a silica gel pad, the solvent was concentrated under reduced pressure and dried in vacuo to give $\mathbf{1c}$ (8.2 mg) as a yellow solid in 98% yield.

Thermal isomerization of $2\mathbf{c}$ in a solid state:



A solid of $2\mathbf{c}$ (3.1 mg, 5.84 μmol) was heated at 210 $^\circ\text{C}$ for 5 h to give $\mathbf{1c}$ (3.1 mg) as a yellow solid in 100% yield.

X-ray Analyses

Data were collected with a Rigaku Mercury 70 diffractometer (Mo- $\text{K}\alpha$ radiation, $\lambda = 0.71075 \text{ \AA}$) for dications or a Rigaku XtaLAB Synergy (Cu- $\text{K}\alpha$ radiation, $\lambda = 1.54184 \text{ \AA}$) for others. The structure was solved by the direct method (SIR2004) and ShelXT (Sheldrick) for dications and others, respectively, and refined by the full-matrix least-squares method on F^2 with anisotropic temperature factors for non-hydrogen atoms. All the hydrogen atoms were located at the calculated positions and refined with riding. A Rigaku Crystal Structure crystallographic software package and Olex2 [48] were used for all calculations for dications and others, respectively.

Crystal data for $\mathbf{1a}$: CCDC 1586191 (at 120 K), 1586192 (at 160 K), 1567390 (at 200 K), 1567391 (at 240 K), 1567392 (at 280 K), 1567393 (at 320 K), 1567394 (at 360 K), 1567395 (at 400 K) [16].

Crystal data for $\mathbf{1b}$: CCDC 1567396 (200 K), 1567397 (at 240 K), 1567398 (at 280 K), 1567399 (at 320 K), 1567400 (at 360 K), 1567401 (at 400 K) [16].

At 300 K (CCDC 2005623)

Crystals, colorless block, $0.8 \times 0.4 \times 0.2 \text{ mm}^3$, were obtained by recrystallization from $\text{CHCl}_3/\text{hexane}$.

Crystal Data for $\text{C}_{42}\text{H}_{28}$ ($M = 532.64 \text{ g/mol}$): monoclinic, space group $P2_1/c$ (#14), $a = 12.79971(16) \text{ \AA}$, $b = 9.22089(12) \text{ \AA}$, $c = 24.0558(3) \text{ \AA}$, $\beta = 100.0421(11)^\circ$, $V = 2795.68(6) \text{ \AA}^3$, $Z = 4$, $T = 300 \text{ K}$, μ ($\text{CuK}\alpha$) = 0.543 mm^{-1} , $D_{\text{calc}} = 1.265 \text{ g/cm}^3$, 18,751 reflections measured ($7.014^\circ \leq 2\theta \leq 151.596^\circ$), 5646 unique ($R_{\text{int}} = 0.0447$, $R_{\text{sigma}} = 0.0314$) which were used in all calculations. The final R_1 was 0.0879 ($I > 2\sigma(I)$) and wR_2 was 0.2601 (all data).

Crystal data for 1c: CCDC 1586193 (100 K), 1586194 (120 K), 1586195 (160 K), 1567402 (200 K), 1567403 (240 K), 1567404 (280 K), 1567405 (320 K), 1567406 (360 K), 1567407 (400 K) [16].

Crystal data for 2a·0.5CH₂Cl₂: Crystals, colorless plate, $0.6 \times 0.2 \times 0.05 \text{ mm}^3$, were obtained by recrystallization from $\text{CH}_2\text{Cl}_2/\text{hexane}$.

At 100 K (CCDC 2005624)

Crystal Data for $\text{C}_{40.5}\text{H}_{27}\text{Cl}$ ($M = 549.07 \text{ g/mol}$): monoclinic, space group $P2_1$ (#4), $a = 10.57274(8) \text{ \AA}$, $b = 29.7730(2) \text{ \AA}$, $c = 8.67995(7) \text{ \AA}$, $\beta = 104.9856(8)^\circ$, $V = 2639.37(4) \text{ \AA}^3$, $Z = 4$, $T = 100 \text{ K}$, μ ($\text{CuK}\alpha$) = 1.500 mm^{-1} , $D_{\text{calc}} = 1.382 \text{ g/cm}^3$, 18,866 reflections measured ($5.936^\circ \leq 2\theta \leq 151.872^\circ$), 9715 unique ($R_{\text{int}} = 0.0534$, $R_{\text{sigma}} = 0.0501$) which were used in all calculations. The final R_1 was 0.0528 ($I > 2\sigma(I)$) and wR_2 was 0.1606 (all data). Solvent mask procedure was used for the analysis.

At 200 K (CCDC 2005625)

Crystal Data for $\text{C}_{40.5}\text{H}_{27}\text{Cl}$ ($M = 549.07 \text{ g/mol}$): monoclinic, space group $P2_1$ (#4), $a = 10.61353(10) \text{ \AA}$, $b = 29.8550(2) \text{ \AA}$, $c = 8.72432(7) \text{ \AA}$, $\beta = 104.9965(8)^\circ$, $V = 2670.30(4) \text{ \AA}^3$, $Z = 4$, $T = 200 \text{ K}$, μ ($\text{CuK}\alpha$) = 1.483 mm^{-1} , $D_{\text{calc}} = 1.366 \text{ g/cm}^3$, 18,712 reflections measured ($5.92^\circ \leq 2\theta \leq 151.402^\circ$), 9078 unique ($R_{\text{int}} = 0.0390$, $R_{\text{sigma}} = 0.0403$) which were used in all calculations. The final R_1 was 0.0529 ($I > 2\sigma(I)$) and wR_2 was 0.1620 (all data).

At 300 K (CCDC 2005626)

Crystal Data for $\text{C}_{40.5}\text{H}_{27}\text{Cl}$ ($M = 549.07 \text{ g/mol}$): monoclinic, space group $P2_1/c$ (#14), $a = 10.66505(11) \text{ \AA}$, $b = 29.9399(3) \text{ \AA}$, $c = 8.77371(8) \text{ \AA}$, $\beta = 105.0238(9)^\circ$, $V = 2705.77(5) \text{ \AA}^3$, $Z = 4$, $T = 300 \text{ K}$, μ ($\text{CuK}\alpha$) = 1.463 mm^{-1} , $D_{\text{calc}} = 1.348 \text{ g/cm}^3$, 19,356 reflections measured ($5.904^\circ \leq 2\theta \leq 151.35^\circ$), 5481 unique ($R_{\text{int}} = 0.0301$, $R_{\text{sigma}} = 0.0257$) which were used in all calculations. The final R_1 was 0.0429 ($I > 2\sigma(I)$) and wR_2 was 0.1235 (all data). Solvent mask procedure was used for the analysis.

Crystal data for 2b: Crystals, colorless plate, $0.6 \times 0.2 \times 0.01 \text{ mm}^3$, were obtained by recrystallization from $\text{CHCl}_3/\text{hexane}$.

100 K (CCDC 2005627)

Crystal Data for $C_{42}H_{28}$ ($M = 532.64$ g/mol): monoclinic, space group $P2_1/c$ (#14), $a = 13.25388(13)$ Å, $b = 8.74148(10)$ Å, $c = 23.6015(2)$ Å, $\beta = 97.1751(8)^\circ$, $V = 2713.02(5)$ Å³, $Z = 4$, $T = 100$ K, μ (CuK α) = 0.559 mm⁻¹, $D_{calc} = 1.304$ g/cm³, 19,174 reflections measured ($6.722^\circ \leq 2\theta \leq 151.564^\circ$), 5451 unique ($R_{int} = 0.0286$, $R_{sigma} = 0.0244$) which were used in all calculations. The final R_1 was 0.0416 ($I > 2\sigma(I)$) and wR_2 was 0.1087 (all data).

At 200 K (CCDC 2005628)

Crystal Data for $C_{42}H_{28}$ ($M = 532.64$ g/mol): monoclinic, space group $P2_1/c$ (#14), $a = 13.25273(12)$ Å, $b = 8.78403(9)$ Å, $c = 23.6979(2)$ Å, $\beta = 97.1488(8)^\circ$, $V = 2737.28(4)$ Å³, $Z = 4$, $T = 200$ K, μ (CuK α) = 0.554 mm⁻¹, $D_{calc} = 1.292$ g/cm³, 18,497 reflections measured ($6.722^\circ \leq 2\theta \leq 151.798^\circ$), 5485 unique ($R_{int} = 0.0248$, $R_{sigma} = 0.0224$) which were used in all calculations. The final R_1 was 0.0422 ($I > 2\sigma(I)$) and wR_2 was 0.1147 (all data).

At 300 K (CCDC 2005629)

Crystal Data for $C_{42}H_{28}$ ($M = 532.64$ g/mol): monoclinic, space group $P2_1/c$ (#14), $a = 13.26469(12)$ Å, $b = 8.83221(9)$ Å, $c = 23.79279(19)$ Å, $\beta = 97.2129(8)^\circ$, $V = 2765.42(4)$ Å³, $Z = 4$, $T = 300$ K, μ (CuK α) = 0.549 mm⁻¹, $D_{calc} = 1.279$ g/cm³, 19,896 reflections measured ($6.716^\circ \leq 2\theta \leq 151.63^\circ$), 5525 unique ($R_{int} = 0.0254$, $R_{sigma} = 0.0245$) which were used in all calculations. The final R_1 was 0.0423 ($I > 2\sigma(I)$) and wR_2 was 0.1223 (all data).

At 400 K (CCDC 2005630)

Crystal Data for $C_{42}H_{28}$ ($M = 532.64$ g/mol): monoclinic, space group $P2_1/c$ (#14), $a = 13.3028(8)$ Å, $b = 8.9258(6)$ Å, $c = 23.8898(17)$ Å, $\beta = 97.369(7)^\circ$, $V = 2813.2(3)$ Å³, $Z = 4$, $T = 400$ K, μ (CuK α) = 0.539 mm⁻¹, $D_{calc} = 1.258$ g/cm³, 14,819 reflections measured ($6.7^\circ \leq 2\theta \leq 151.576^\circ$), 5620 unique ($R_{int} = 0.0636$, $R_{sigma} = 0.0585$) which were used in all calculations. The final R_1 was 0.0940 ($I > 2\sigma(I)$) and wR_2 was 0.2884 (all data).

Crystal data of 2c: Crystals, yellow plate, $0.3 \times 0.3 \times 0.03$ mm³, were obtained by recrystallization from CH₂Cl₂/hexane.

100 K (CCDC 2005631)

Crystal Data for $C_{42}H_{26}$ ($M = 530.63$ g/mol): monoclinic, space group $P2_1/n$ (#14), $a = 10.0184(2)$ Å, $b = 17.6572(3)$ Å, $c = 15.6318(3)$ Å, $\beta = 106.398(2)^\circ$, $V = 2652.73(9)$ Å³, $Z = 4$, $T = 100$ K, μ (CuK α) = 0.572 mm⁻¹, $D_{calc} = 1.329$ g/cm³, 17,007 reflections measured ($7.734^\circ \leq 2\theta \leq 151.748^\circ$), 5342 unique ($R_{int} = 0.0347$, $R_{sigma} = 0.0293$) which were used in all calculations. The final R_1 was 0.0543 ($I > 2\sigma(I)$) and wR_2 was 0.1503 (all data).

At 200 K (CCDC 2005632)

Crystal Data for $C_{42}H_{26}$ ($M = 530.63$ g/mol): monoclinic, space group $P2_1/n$ (#14), $a = 10.02597(16)$ Å, $b = 17.7295(2)$ Å, $c = 15.7006(3)$ Å, $\beta = 106.5276(17)^\circ$, $V = 2675.56(7)$ Å³, $Z = 4$, $T = 200$ K, μ (CuK α) = 0.567 mm⁻¹, $D_{calc} = 1.317$ g/cm³, 16,695 reflections measured ($7.704^\circ \leq 2\theta \leq 151.728^\circ$), 5397 unique ($R_{int} = 0.0468$, $R_{sigma} = 0.0337$) which were used in all calculations. The final R_1 was 0.0597 ($I > 2\sigma(I)$) and wR_2 was 0.1655 (all data).

At 300 K (CCDC 2005633)

Crystal Data for $C_{42}H_{26}$ ($M = 530.63$ g/mol): monoclinic, space group $P2_1/n$ (#14), $a = 10.03723(15)$ Å, $b = 17.8005(2)$ Å, $c = 15.7928(2)$ Å, $\beta = 106.6931(15)^\circ$, $V = 2702.74(7)$ Å³, $Z = 4$, $T = 300$ K, μ (CuK α) = 0.561 mm⁻¹, $D_{calc} = 1.304$ g/cm³, 18,421 reflections measured ($7.67^\circ \leq 2\theta \leq 151.552^\circ$), 5430 unique ($R_{int} = 0.0311$, $R_{sigma} = 0.0242$) which were used in all calculations. The final R_1 was 0.0464 ($I > 2\sigma(I)$) and wR_2 was 0.1285 (all data).

At 400 K (CCDC 2005634)

Crystal Data for $C_{42}H_{26}$ ($M = 530.63$ g/mol): monoclinic, space group $P2_1/n$ (#14), $a = 10.0545(2)$ Å, $b = 17.8873(3)$ Å, $c = 15.8817(3)$ Å, $\beta = 106.890(2)^\circ$, $V = 2733.10(9)$ Å³, $Z = 4$, $T = 400$ K, μ (CuK α) = 0.555 mm⁻¹, $D_{calc} = 1.290$ g/cm³, 16,746 reflections measured ($7.634^\circ \leq 2\theta \leq 152.658^\circ$), 5509 unique ($R_{int} = 0.0346$, $R_{sigma} = 0.0268$) which were used in all calculations. The final R_1 was 0.0512 ($I > 2\sigma(I)$) and wR_2 was 0.1477 (all data).

Crystal data for $3a^{2+}(\text{SbCl}^6)_2 \cdot \text{CH}_3\text{CN}$: Crystals, purple plate, $0.4 \times 0.1 \times 0.02$ mm³, were obtained by recrystallization from $\text{CH}_3\text{CN}/\text{Et}_2\text{O}$.

Crystal Data for $C_{42}H_{29}Cl_{12}NSb_2$ ($M = 1216.63$ g/mol): monoclinic, space group $P2_1/c$ (#14), $a = 28.596(8)$ Å, $b = 13.285(4)$ Å, $c = 27.746(8)$ Å, $\beta = 118.185(5)^\circ$, $V = 9291(5)$ Å³, $Z = 8$, $T = 150$ K, μ (MoK α) = 1.8827 mm⁻¹, $D_{calc} = 1.739$ g/cm³, 33,560 reflections measured ($2\theta_{max} = 55.0^\circ$), 17,935 unique ($R_{int} = 0.0484$) which were used in all calculations. The final R_1 was 0.0600 ($I > 2\sigma(I)$) and wR_2 was 0.1878 (all data). CCDC 2005635.

Crystal data for $3b^{2+}(\text{SbCl}^6)_2$: Crystals, purple needle, $0.3 \times 0.05 \times 0.05$ mm³, were obtained by recrystallization from $\text{CH}_3\text{CN}/\text{Et}_2\text{O}$.

Crystal Data for $C_{42}H_{28}Cl_{12}Sb_2$ ($M = 1201.62$ g/mol): orthorhombic, space group $Pbcn$ (#60), $a = 10.220(2)$ Å, $b = 24.166(5)$ Å, $c = 18.191(4)$ Å, $V = 4493(2)$ Å³, $Z = 4$, $T = 150$ K, μ (MoK α) = 1.9449 mm⁻¹, $D_{calc} = 1.776$ g/cm³, 23,381 reflections measured ($2\theta_{max} = 55.0^\circ$), 4396 unique ($R_{int} = 0.1164$) which were used in all calculations. The final R_1 was 0.0851 ($I > 2\sigma(I)$) and wR_2 was 0.2275 (all data). CCDC 2005636.

Crystal data for $3c^{2+}(\text{SbCl}^6)_2 \cdot 0.5\text{C}_4\text{H}_{10}\text{O}$: Crystals, purple plate, $0.6 \times 0.1 \times 0.02$ mm³, were obtained by recrystallization from $\text{CH}_3\text{CN}/\text{Et}_2\text{O}$.

Crystal Data for $C_{44}H_{31}Cl_{12}O_{0.50}Sb_2$ ($M = 1236.66$ g/mol): triclinic, space group $P\bar{1}$ (#2), $a = 12.055(7)$ Å, $b = 13.961(6)$ Å, $c = 14.973(8)$ Å, $\alpha = 73.66(3)^\circ$, $\beta = 78.70(3)^\circ$, $\gamma = 71.47(3)^\circ$, $V = 2277(2)$ Å³, $Z = 2$, $T = 150$ K, μ (MoK α) =

1.9223 mm⁻¹, $D_{calc} = 1.804$ g/cm³, 16,595 reflections measured ($2\theta_{max} = 55.1^\circ$), 8772 unique ($R_{int} = 0.0423$) which were used in all calculations. The final R_1 was 0.0562 ($I > 2\sigma(I)$) and wR_2 was 0.1524 (all data). CCDC 2005637.

SCSC photocyclization of **1b** with $\lambda > 390$ nm

Photoirradiation for 10 h, measured at 200 K (**1b/2b** = 55/45)

Crystals, colorless block, $0.4 \times 0.2 \times 0.2$ mm³, were obtained by recrystallization from CHCl₃/hexane, which was used for photoreaction in a glass tube [Xe lamp with corning color filter (No. 3-73)].

Crystal Data for C₄₂H₂₈ ($M = 532.64$ g/mol): monoclinic, space group $P2_1/c$ (#14), $a = 12.9352(3)$ Å, $b = 9.05991(18)$ Å, $c = 23.7724(4)$ Å, $\beta = 98.6273(16)^\circ$, $V = 2754.41(9)$ Å³, $Z = 4$, $T = 200$ K, μ (CuK α) = 0.551 mm⁻¹, $D_{calc} = 1.284$ g/cm³, 16,829 reflections measured ($6.912^\circ \leq 2\theta \leq 151.766^\circ$), 5575 unique ($R_{int} = 0.0179$, $R_{sigma} = 0.0179$) which were used in all calculations. The final R_1 was 0.0672 ($I > 2\sigma(I)$) and wR_2 was 0.1883 (all data). CCDC 2005638.

Photoirradiation for 60 h, measured at 200 K (**1b/2b** = 0/100)

Crystals, colorless block, $0.6 \times 0.3 \times 0.15$ mm³, were obtained by recrystallization from CHCl₃/hexane, which was used for photoreaction in a glass tube [Xe lamp with corning color filter (No. 3-73)].

Crystal Data for C₄₂H₂₈ ($M = 532.64$ g/mol): monoclinic, space group $P2_1/c$ (#14), $a = 13.26411(14)$ Å, $b = 8.78016(8)$ Å, $c = 23.6884(2)$ Å, $\beta = 97.1720(9)^\circ$, $V = 2737.19(5)$ Å³, $Z = 4$, $T = 200$ K, μ (CuK α) = 0.554 mm⁻¹, $D_{calc} = 1.293$ g/cm³, 17,430 reflections measured ($6.716^\circ \leq 2\theta \leq 151.468^\circ$), 5530 unique ($R_{int} = 0.0239$, $R_{sigma} = 0.0230$) which were used in all calculations. The final R_1 was 0.0411 ($I > 2\sigma(I)$) and wR_2 was 0.1099 (all data). CCDC 2005639.

SCSC thermal isomerization from **2b** upon heating at 493 K

Heating for 10 min, measured at 300 K (**2b/1b** = 82/18)

Crystals, colorless plate, $0.8 \times 0.2 \times 0.05$ mm³, were obtained by recrystallization from CHCl₃/hexane, which was used for thermal reaction in a glass tube.

Crystal Data for C₄₂H₂₈ ($M = 532.64$ g/mol): monoclinic, space group $P2_1/c$ (#14), $a = 13.1312(2)$ Å, $b = 8.93972(15)$ Å, $c = 23.8993(4)$ Å, $\beta = 97.3675(17)^\circ$, $V = 2782.36(8)$ Å³, $Z = 4$, $T = 300$ K, μ (CuK α) = 0.545 mm⁻¹, $D_{calc} = 1.272$ g/cm³, 17,631 reflections measured ($6.788^\circ \leq 2\theta \leq 151.838^\circ$), 5621 unique ($R_{int} = 0.0337$, $R_{sigma} = 0.0322$) which were used in all calculations. The final R_1 was 0.0559 ($I > 2\sigma(I)$) and wR_2 was 0.1727 (all data). CCDC 2005640.

Heating for 60 min, measured at 300 K (**2b/1b** = 0/100)

Crystals, colorless plate, $0.3 \times 0.05 \times 0.02$ mm³, were obtained by recrystallization from CHCl₃/hexane, which was used for thermal reaction in a glass tube.

Crystal Data for C₄₂H₂₈ ($M = 532.64$ g/mol): monoclinic, space group $P2_1/c$ (#14), $a = 12.8016(3)$ Å, $b = 9.2206(3)$ Å, $c = 24.0574(7)$ Å, $\beta = 99.953(3)^\circ$, $V = 2796.97(13)$ Å³, $Z = 4$, $T = 300$ K, μ (CuK α) = 0.543 mm⁻¹, $D_{calc} = 1.265$ g/cm³,

16,555 reflections measured ($7.01^\circ \leq 2\theta \leq 151.956^\circ$), 5627 unique ($R_{\text{int}} = 0.0262$, $R_{\text{sigma}} = 0.0258$) which were used in all calculations. The final R_1 was 0.0751 ($I > 2\sigma(I)$) and wR_2 was 0.2329 (all data). CCDC 200564.

References

1. M.A. Majewski, M. Stępień, *Angew. Chem. Int. Ed.* **58**, 86–116 (2019)
2. M. Saito, H. Shinokubo, H. Sakurai, *Mater. Chem. Front.* **2**, 635–661 (2018)
3. S.H. Pun, Q. Miao, *Acc. Chem. Res.* **51**, 1630–1642 (2018)
4. T. Hosokawa, Y. Takahashi, T. Matsushima, S. Watanabe, S. Kikkawa, I. Azumaya, A. Tsurusaki, K. Kamikawa, *J. Am. Chem. Soc.* **139**, 18512–18521 (2017)
5. P. Hu, T.S. Herng, A. Osuka, W. Zeng, C. Chi, J. Ding, J. Siegel, H. Phan, Q. Wang, T.Y. Gopalakrishna, J. Wu, T. Tanaka, *Chem. Sci.* **9**, 5100–5105 (2018)
6. Y. Nakakuki, T. Hirose, K. Matsuda, *J. Am. Chem. Soc.* **140**, 15461–15469 (2018)
7. Y. Xiao, J.T. Mague, R.H. Schmehl, F.M. Haque, R.A. Pascal, *Angew. Chem. Int. Ed.* **58**, 2831–2833 (2019)
8. Y. Hu, G.M. Paternò, X.-Y. Wang, X.-C. Wang, M. Guizzardi, Q. Chen, D. Schollmeyer, X.-Y. Cao, G. Cerullo, F. Scotognella, K. Müllen, A. Narita, *J. Am. Chem. Soc.* **141**, 12797–12803 (2019)
9. G. Povie, Y. Segawa, T. Nishihara, Y. Miyauchi, K. Itami, *Science* **356**, 172–175 (2017)
10. K.Y. Cheung, S. Gui, C. Deng, H. Liang, Z. Xia, Z. Liu, L. Chi, Q. Miao, *Chem* **5**, 838–847 (2019)
11. Y. Segawa, M. Kuwayama, Y. Hijikata, M. Fushimi, T. Nishihara, J. Pirillo, J. Shirasaki, N. Kubota, K. Itami, *Science* **365**, 272–276 (2019)
12. Y. Ni, T.Y. Gopalakrishna, H. Phan, T. Kim, T.S. Herng, Y. Han, T. Tao, J. Ding, D. Kim, J. Wu, *Nat. Chem.* **12**, 242–248 (2020)
13. M. Rickhaus, M. Jirasek, L. Tejerina, H. Gotfredsen, M.D. Peeks, R. Haver, H.-W. Jiang, T.D.W. Claridge, H.L. Anderson, *Nat. Chem.* **12**, 236–241 (2020)
14. T. Mio, K. Ikemoto, S. Sato, H. Isobe, *Angew. Chem. Int. Ed.* **59**, 6567–6571 (2020)
15. T.A. Schaub, E.A. Prantl, J. Kohn, M. Bursch, C.R. Marshall, E.J. Leonhardt, T.C. Lovell, L.N. Zakharov, C.K. Brozek, S.R. Waldvogel, S. Grimme, R. Jasti, *J. Am. Chem. Soc.* **142**, 8763–8775 (2020)
16. Y. Ishigaki, T. Shimajiri, T. Takeda, R. Katoono, T. Suzuki, *Chem* **4**, 795–806 (2018)
17. J. Luo, K. Song, F.L. Gu, Q. Miao, *Chem. Sci.* **2**, 2029–2034 (2011)
18. Y. Ishigaki, Y. Hayashi, T. Suzuki, *J. Am. Chem. Soc.* **141**, 18293–18300 (2019)
19. M. Pillekamp, W. Alachraf, I.M. Oppel, G. Dyker, *J. Org. Chem.* **74**, 8355–8358 (2009)
20. B.L. Feringa, *J. Org. Chem.* **72**, 6635–6652 (2007)
21. M. Irie, T. Fukaminato, K. Matsuda, S. Kobatake, *Chem. Rev.* **114**, 12174–12277 (2014)
22. V. García-López, D. Liu, J.M. Tour, *Chem. Rev.* **120**, 79–124 (2020)
23. M. Baroncini, S. Silvi, A. Credi, *Chem. Rev.* **120**, 200–268 (2020)
24. P. Ravat, T. Šolomek, D. Häussinger, O. Blacque, M. Juriček, *J. Am. Chem. Soc.* **140**, 10839–10847 (2018)
25. C.L. Fleming, S. Li, M. Grøtli, J. Andréasson, *J. Am. Chem. Soc.* **140**, 14069–14072 (2018)
26. T. Yang, Y. Wang, X. Liu, G. Li, W. Che, D. Zhu, Z. Su, M.R. Bryce, *Chem. Commun.* **55**, 14582–14585 (2019)
27. P. Lentès, E. Stadler, F. Röhricht, A. Brahms, J. Gröbner, F.D. Sönnichsen, G. Gescheidt, R. Herges, *J. Am. Chem. Soc.* **141**, 13592–13600 (2019)
28. N.-Y. Li, J.-M. Chen, X.-Y. Tang, G.-P. Zhang, D. Liu, *Chem. Commun.* **56**, 1984–1987 (2020)
29. K. Novak, V. Enkelmann, G. Wegner, K.B. Wagener, *Angew. Chem. Int. Ed. Engl.* **32**, 1614–1616 (1993)

30. G.K. Kole, T. Kojima, M. Kawano, J.J. Vittal, *Angew. Chem. Int. Ed.* **53**, 2143–2146 (2014)
31. N.Y. Li, D. Liu, B.F. Abrahams, J.P. Lang, *Chem. Commun.* **54**, 5831–5834 (2018)
32. G. Pahari, B. Bhattacharya, C.M. Reddy, D. Ghoshal, *Chem. Commun.* **55**, 12515–12518 (2019)
33. I.E. Claassens, L.J. Barbour, D.A. Haynes, *J. Am. Chem. Soc.* **141**, 11425–11429 (2019)
34. J. Zhang, J. Li, X. Feng, M. Kong, Z.-B. Hu, Y.-X. Zheng, Y. Song, *Chem. Commun.* **55**, 12873–12876 (2019)
35. M.W. Wong, *Chem. Phys. Lett.* **256**, 391–399 (1996)
36. T. Suzuki, E. Ohta, H. Kawai, K. Fujiwara, T. Fukushima, *Synlett* 851–869 (2007)
37. T. Suzuki, H. Tamaoki, J. Nishida, H. Higuchi, T. Iwai, Y. Ishigaki, K. Hanada, R. Katoono, H. Kawai, K. Fujiwara, T. Fukushima, *Organic Redox Systems: Synthesis, Properties, and Applications*, Chap. 2 (Wiley, Hoboken, 2015), pp. 13–37
38. T. Suzuki, J. Nishida, T. Tsuji, *Angew. Chem. Int. Ed. Engl.* **36**, 1329–1331 (1997)
39. T. Suzuki, J. Nishida, T. Tsuji, *Chem. Commun.* 2193–2194 (1998)
40. T. Suzuki, K. Ono, J. Nishida, H. Takahashi, T. Tsuji, *J. Org. Chem.* **65**, 4944–4948 (2000)
41. Y. Ishigaki, Y. Hayashi, K. Sugawara, T. Shimajiri, W. Nojo, R. Katoono, T. Suzuki, *Molecules* **2017**, 22 (1900)
42. T. Suzuki, Y. Ishigaki, T. Iwai, H. Kawai, K. Fujiwara, H. Ikeda, Y. Kano, K. Mizuno, *Chem. A Eur. J.* **15**, 9434–9441 (2009)
43. R. Hoffmann, *Acc. Chem. Res.* **4**, 1–9 (1971)
44. K. Suzuki, A. Kobayashi, S. Kaneko, K. Takehira, T. Yoshihara, H. Ishida, Y. Shiina, S. Oishi, S. Tobita, *Phys. Chem. Chem. Phys.* **11**, 9850 (2009)
45. J.M. Frisch, W.G. Trucks, B.H. Schlegel, E.G. Scuseria, A.M. Robb, R.J. Cheeseman, G. Scalmani, V. Barone, A.G. Petersson, H. Nakatsuji, X. Li, M. Caricato, V.A. Marenich, J. Bloino, G.B. Janesko, R. Gomperts, B. Mennucci, P.H. Hratchian, V.J. Ortiz, F.A. Izmaylov, L.J. Sonnenberg, D. Williams-Young, F. Ding, F. Lipparini, F. Egidi, J. Goings, B. Peng, A. Petrone, T. Henderson, D. Ranasinghe, G.V. Zakrzewski, J. Gao, N. Rega, G. Zheng, W. Liang, M. Hada, M. Ehara, K. Toyota, R. Fukuda, J. Hasegawa, M. Ishida, T. Nakajima, Y. Honda, O. Kitao, H. Nakai, T. Vreven, K. Throssell, A.J. Montgomery, Jr., E.J. Peralta, F. Ogliaro, J.M. Bearpark, J.J. Heyd, N.E. Brothers, N.K. Kudin, N.V. Staroverov, A.T. Keith, R. Kobayashi, J. Normand, K. Raghavachari, P.A. Rendell, C.J. Burant, S.S. Iyengar, J. Tomasi, M. Cossi, M.J. Millam, M. Klene, C. Adamo, R. Cammi, W.J. Ochterski, L.R. Martin, K. Morokuma, O. Farkas, B.J. Foresman, J.D. Fox, (Gaussian, Inc., Wallingford CT, 2019)
46. T. Lu, F. Chen, *J. Comput. Chem.* **33**, 580–592 (2012)
47. E.D. Glendening, J.K. Badenhoop, A.E. Reed, J.E. Carpenter, J.A. Bohmann, C.M. Morales, P. Karafiloglou, C.R. Landis, F. Weinhold, *Theoretical Chemistry Institute* (University of Wisconsin, Madison, WI, 2018)
48. O.V. Dolomanov, L.J. Bourhis, R.J. Gildea, J.A.K. Howard, H. Puschmann, *J. Appl. Crystallogr.* **42**, 339–341 (2009)

Curriculum Vitae

Takuya Shimajiri

Department of Chemistry, Faculty of Science,
Hokkaido University, Sapporo, 060-0810, Japan
Web: <https://www.chem.sci.hokudai.ac.jp/~org1/>
Tel: +81-11-706-3396
e-mail: t.shimajiri@sci.hokudai.ac.jp



Education and Employment

2019-Apr./2022-Mar. **Ph.D.**; Graduate School of Chemical Science and Engineering, Hokkaido University. (Advisor: Takanori Suzuki).
2017-Apr./2019-Mar. **M.S.**; Graduate School of Chemical Science and Engineering, Hokkaido University.
2013-Apr./2017-Mar. **B.S.**; Faculty of Science, Hokkaido University.
2017-Sep./2022-Mar. **Research Fellow**, Hokkaido University Ambitious Leader's Program, Fostering Future Leader' to Open New Frontiers in Materials Science.
2019-Apr./2022-Mar. **Research Fellowship for Young Scientists**. Japan Society for the Promotion of Science (JSPS, DC1).
2022-Apr./present **Specially Appointed Assistant Professor**, Faculty of Science, Hokkaido University.

Awards

6. **Poster Prize**; The 5th Meeting of Condensed Conjugation for Rising Generation (2022).
5. **Poster Award**; The 51st Summer School of Structural Organic Chemistry (2019).
4. **Best Poster Award**; The 31st Banyu Symposium (2019).
3. **Poster Award**; The 8th CSJ Chemistry Festa (2018).
2. **Best Discussion Award**; The 6th International Symposium on AMBITIOUS LEADER'S PROGRAM Fostering Future Leaders to Open New Frontiers in Materials Science (2018).
1. **Best Poster Award**; The 18th Ries-Hokudai International Symposium (2017).

Research Interest

Compounds that are difficult to synthesize and/or easy to decompose in ambient conditions may show interesting properties. For example, C–C single bond is usually rigid and robust, and its elongation beyond 1.8 Å has been considered impossible. On the other hand, based on “intramolecular core–shell structure,” we succeeded in the first preparation of the compounds with a C–C single bond beyond 1.8 Å, which has been regarded as a boundary between bonded and non-bonded states. In addition, we also discovered that such a long and weak C–C single bond has a unique “*flexibility*” that can expand and contract upon slight external stimuli. Now, I am focusing on not only chemical bonds but also organic π -conjugated systems to elucidate unique chemical phenomena in extreme structures through experimental and theoretical studies.